



저작자표시-비영리-변경금지 2.0 대한민국

이용자는 아래의 조건을 따르는 경우에 한하여 자유롭게

- 이 저작물을 복제, 배포, 전송, 전시, 공연 및 방송할 수 있습니다.

다음과 같은 조건을 따라야 합니다:



저작자표시. 귀하는 원저작자를 표시하여야 합니다.



비영리. 귀하는 이 저작물을 영리 목적으로 이용할 수 없습니다.



변경금지. 귀하는 이 저작물을 개작, 변형 또는 가공할 수 없습니다.

- 귀하는, 이 저작물의 재이용이나 배포의 경우, 이 저작물에 적용된 이용허락조건을 명확하게 나타내어야 합니다.
- 저작권자로부터 별도의 허가를 받으면 이러한 조건들은 적용되지 않습니다.

저작권법에 따른 이용자의 권리는 위의 내용에 의하여 영향을 받지 않습니다.

이것은 [이용허락규약\(Legal Code\)](#)을 이해하기 쉽게 요약한 것입니다.

[Disclaimer](#)

공학박사학위논문

시간지연 열-탄성 감쇠를 고려한 자이로
구조물의 최적화 설계에 대한 연구

A study on the optimization of the gyro structure
considering the time-lagging thermoelastic dissipation

2019 년 8 월

서울대학교 대학원

기계항공공학부

김 정 환

시간지연 열-탄성 감쇠를 고려한 자이로 구조물의 최적화 설계에 대한 연구

A study on the optimization of the gyro structure considering the time-lagging thermoelastic dissipation

지도교수 김 지 환

이 논문을 공학박사 학위논문으로 제출함

2019 년 5 월

서울대학교 대학원

기계항공공학부

김 정 환

김정환의 공학박사 학위논문을 인준함

2019 년 6 월

위 원 장 : _____

부위원장 : _____

위 원 : _____

위 원 : _____

위 원 : _____

시간지연 열-탄성 감쇠를 고려한 자이로 구조물의 최적화 설계에 대한 연구

A study on the optimization of the gyro structure considering the time-lagging thermoelastic dissipation

지도교수 김 지 환

이 논문을 공학박사 학위논문으로 제출함

2019 년 5 월

서울대학교 대학원

기계항공공학부

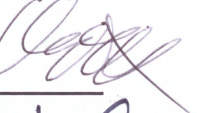
김 정 환

김정환의 공학박사 학위논문을 인준함

2019 년 6 월

위원장 : 김 용 혁 

부위원장 : 김 지 환 

위원 : 윤 순 진 

위원 : 임 재 욱 

위원 : 최 진 욱 

Abstract

A study on the optimization of the gyro structure considering the time-lagging thermoelastic dissipation

Jung-Hwan Kim

Department of Mechanical and Aerospace Engineering

The Graduate School

Seoul National University

Vibration characteristics of a gyro structures are mainly studied with the thermoelastic damping (TED) considering the non-Fourier heat conduction in the thesis. Firstly, the TED with the time-lagging effect is introduced with respect to the finite-speed heat flux. Then the solution is obtained by the temperature profile of 3-dimensional heat conduction equation using Bessel function of 1st kind. Thus, the TED can be defined using the quality factor (Q) with respect to the complex numbers. Moreover, the peak of the inverse value of Q is obtained with respect to the frequency, and the simplified expressions are suggested according to the frequency, lagging time, and geometrical factors. In here, the lagging time is set by the second sound velocity. Furthermore, the TED can be simplified by an equivalent coefficient of the linear damping in single cycle. And the temperature profile is graphically described to illustrate the delay of the heat flux.

And the Rayleigh-Ritz method based on Hamilton's principle is applied to obtain the equation of motion including imperfect masses and rotating effect. Then the eigenfrequency for inextensible ring is obtained by solving the result with a virtual density with respect to lumped masses. Furthermore, a transfer function is derived by Laplace transform in order to represent the random vibration. And the spectral density (SD) is obtained according to the function, then applications for random vibration are suggested by the standard deviation (StDev). Moreover, the peak factor is introduced to predict the maximum deflection value. Additionally, the frequency trimming method is studied as the modifying additional mass to compensate the split due to the imperfections.

The numerical data are presented as factors in thesis, and the optimization concept is suggested by analyzing the peak of inverse of Q . In order to find the peak, the factors with respect to the frequency and thickness are used according to the cross-sections. Then the radii are obtained as the function of thickness, and other properties. The dissipation is maximum on the peak point, but the difference with respect to the imperfection is smallest. Finally, the peak can be useful to design in conservative point of view.

Keywords: Gyro structure; Thermoelastic damping (TED); Non-Fourier heat conduction; In-plane vibration; Quality factor; Spectral density (SD); Frequency trimming

Student Number: 2014-31044

Contents

Abstract.....	i
Contents.....	iii
List of Tables.....	v
List of Figures.....	vi
Nomenclatures.....	ix
Chapter 1 Introduction.....	1
1.1 Background and motivation.....	1
1.2 Model and vibration analysis.....	4
1.3 Thermoelastic damping	7
1.4 Random vibration.....	10
1.5 Frequency trimming method.....	13
1.6 Thesis scope & outline.....	15
Chapter 2 Thermoelastic damping.....	23
2.1 Constitutive equations	23
2.2 Solution of the heat conduction equation: Temperature profile.....	29
2.3 Quality factor.....	32
2.4 Damping coefficient for random vibration.....	39
2.5 Normalized temperature profile.....	41
Chapter 3 Ring structure.....	54
3.1 Constitutive equations.....	54
3.2 Solutions – eigenfrequencies.....	58
3.3 Transfer function of the forced vibration.....	62

3.4 Random vibration.....	65
3.4 Frequency trimming method.....	72
Chapter 4 Analysis.....	88
4.1 Rectangular cross-sectional ring.....	88
4.2 Circular cross-sectional ring.....	92
Chapter 5 Optimum design.....	103
5.1 Concepts.....	103
5.2 Application to a ring model with rectangular cross-section.....	105
5.3 Application to a toroidal ring: Simplified model of TED.....	107
5.4 Application to a toroidal ring: with respect to the known lagging time.....	110
Chapter 6 Conclusions.....	118
6.1 Summary.....	120
6.2 Future works.....	123
References.....	125
Abstract (Korean)	138

List of Tables

Table 2.1 Solutions of the Bessel function.....	43
Table 2.2 Comparisons of the approximations.....	44
Table 3.1 The additional mass and frequencies after the trimming.....	74
Table. 4.1 Experimental data of the rectangular-cross-sectional ring [23]	95
Table 4.2 Material properties of the silicon [31].....	96
Table 5.1 Comparisons of the results for optimization.....	112

List of Figures

Fig. 1.1 MEMS beam resonator [88].....	18
Fig. 1.2 Modeling of a beam resonator with electrode [89]	19
Fig. 1.3 MEMS toroidal ring gyroscope [32]	20
Fig. 1.4 (a) Schematic of ring structures showing the triangular cross-section of the nanowires [59], (b) Schematic picture of hybrid plasmonic ring-resonator. ($R_0=1000$, $r_0=100$ [nm]) [60].....	21
Fig. 1.5 Vibration mode shape and temperature distribution from COMSOL® [89]	22
Fig. 2.1 Toroidal ring model [21].....	45
Fig. 2.2 Q^{-1} with respect to r_0	46
Fig. 2.3 Each component of Q^{-1} with respect to r_0	47
Fig. 2.4 % difference of Q^{-1} for summation and $q = 1$ only.....	48
Fig. 2.5 Peak frequencies with respect to β_{CV}	49
Fig. 2.6 Q^{-1} on the peak frequencies.....	50
Fig. 2.7 Function $f(\beta_{CV})$ with respect to β_{CV}	51
Fig. 2.8 Damping coefficients.....	52
Fig. 2.9 Normalized temperature profiles.....	53
Fig. 3.1 Eigenfrequency with respect to the mode numbers (a) $\omega_n = \frac{n^2(n^2-1)^2}{n^2+1}$, (b) % difference from n^2	75

Fig. 3.2 Eigenfrequency with respect to the angular rotational velocity (Eq. (3.2.2))	76
Fig. 3.3 Eigenfrequency with respect to the imperfection ($n=2$) (Eq. (3.2.2))	77
Fig. 3.4 Vibrational mode shape considered the orientation angle (Eq. (2.1.11)) with $n = 2$ (a) H-mode (b) L-mode.....	78
Fig. 3.5 Vibrational mode shape considered the orientation angle with $n = 3$ (a) H-mode (b) L-mode.....	79
Fig. 3.6 Normalized SD for ring and beam models.....	80
Fig. 3.7 Phase angles of the models.....	81
Fig. 3.8 (a) Normalized StDev of the response for displacement based on exact- and approximated SDs, (b) % errors between both SDs.....	82
Fig. 3.9 (a) Normalized StDev of the response for displacement with respect to the input frequencies, (b) % errors between both SDs.....	83
Fig. 3.10 Peak factors.....	84
Fig. 3.11 Expectation value of the deflection (Eq. (3.4.9))	85
Fig. 3.12 Difference of eigenfrequencies after attaching trimming masses for the rotating ring.....	86
Fig. 3.13 Q^{-1} for the ring model after attaching trimming masses for the rotating ring.....	87
Fig. 4.1 Q^{-1} of the circular-cross-sectional ring.....	97
Fig. 4.2 Deviation of the Q with respect to the imperfection for the circular-	

cross-sectional ring (a) $n=2$ (b) $n=3$	98
Fig. 4.3 Deviation of the Q with respect to the rotation for circular-cross-sectional ring.....	99
Fig. 4.4 (a) Deviation of the Q with respect to the imperfection for circular-cross-sectional ring (b) % difference from uniform ring	100
Fig. 4.5 Deviation of the Q^{-1} with respect to the rotation for circular-cross-sectional ring (a) $n = 0$, (b) $n = 10$, (c) magnified plot of (b)...	101
Fig. 4.6 Deviation of the ω_n with respect to the rotation for circular-cross-sectional ring (a) $n = 2$, (b) $n = 10$	102
Fig. 5.1 Optimization concept of the rectangular cross-sectional ring: ξ to the complex numbers.....	113
Fig. 5.2 (a) Comparison of Q^{-1} between Zener's and Lifshitz's models, (b) % difference between both models.....	114
Fig. 5.3 Optimum radii with respect to the radial thickness.....	115
Fig. 5.4 Optimum radii with respect to β_{CV}	116
Fig. 5.5 Q^{-1} with respect to β_{CV} on optimum points.....	117

Nomenclatures

A	Cross-sectional area
A_u	Arbitrary magnitude of the vibration
a_{1q}	The solution of the Bessel function
B_n	Arbitrary order of the Bessel function
b	Arbitrary number based on the Bessel function
c	Damping coefficient
(CF)	Crest factor (=peak factor)
Conj[]	Complex conjugate
C_v	Specific heat capacity
E	Young's modulus
$E[]$	Average
E_ω	Young's modulus including the thermoelastic damping
\hat{e}	Cubic dilation
F	Force
F_0	Unit force
f	Force function
$f(\beta_{cv})$	Function of the lagging time
$f(\omega)$	Function of the TED
g	Arbitrary sign for the toroidal ring
H	Transfer function

(HH)	Square of the transfer function
h	Thickness of the beam
i	Order of imperfection
\hat{i}	Order of spectral moment
I	Moment of inertia
inf	Infinite
j	$\sqrt{-1}$
K	Kinetic energy
K_{1q}	Arbitrary number with respect to a_{1q}
k	thermal conductivity
L	Length of the beam
m_i	i -th attached mass
m_s	Spectral moment
M_p	Mass of the perfect ring
m, n	Order of the vibration
N_{\max}	The number of the maximum points
N_{mean}	The number of the peak points
q	The order of the Bessel function
q_u, q_v	External forces
\mathbf{q}	Heat flux vector
Q	Quality factor
r	Coordinate for the radius

r_0	Local radius of the toroidal ring
r_{gyr}	Radius of the gyration
R_0	Mean radius of the ring
\hat{R}	Non-dimensional radius
S_0	Spectral density for the Gaussian white noise
S_{ff}	Spectral density of the forces
S_{uu}, S_{yy}	Spectral density of the responses for the ring and beam
s_j	j -th Sampling point
T	Temperature
T_0	Temperature profile independent to time
\hat{T}	Variable-separated temperature
\hat{T}_a	Ambient temperature
U	Potential energy
u, v	Radial and circumferential vibration mode shapes with respect to the mode number
U_n, V_n	Coefficients of the radial and circumferential vibration mode shapes
\hat{U}_n, \hat{V}_n	Normalized coefficients of the radial and circumferential vibration mode shapes
V	Volume
V_c	Velocity of the general phonon in medium

	(<i>i.e.</i> first <i>or</i> ordinary sound velocity)
V_{2nd}	Second sound velocity
W	Work or energy
x, y, z	Elements of the rectangular coordinate
' (prime)	$\frac{\partial}{\partial \theta}$
$[\dot{\quad}]$	$\frac{\partial}{\partial t}$
Δ_E	Relaxation strength
Ψ	Arbitrary modes
Ω	Rotating angular velocity
α	Thermal expansion coefficient
α_i	Ratio of the imperfect mass to the perfect ring
β	Local angular coordinate for the cross-section of the ring
β_{CV}	Normalized time-lagging
γ	Euler–Mascheroni’s constant (≈ 0.577216)
δ	Partial integral for the variation
$\delta\rho(\theta)$	Element for the imperfections of the virtual density
ε	Strains
ε_b	Vanmarcke’s bandwidth coefficient
θ	Angular coordinate element
λ_n	Eigenvalue of the beam
λ_{trm}	Trimming coefficient

ν	Poisson's ratio
ξ	Constant of the thermoelastic for the rectangular-cross-sectional structure
ρ_0	Material density
ρ_{imp}	Virtual density
σ	Stress
$\sigma_u, \sigma_{\dot{u}}, \sigma_{\ddot{u}}$	Standard deviations of the deformation, velocity, and acceleration
τ	General relaxation time
τ_q	q -th order general relaxation time
τ_{CV}	Time-lagging
χ	Thermal diffusivity
ψ_j	Orientalional angle
ω	General frequency or input frequency in random vibration
ω_n	Eigenfrequency in n -th mode
(subscripts)	
approx	Approximated random vibration analysis without off-diagonal terms
eq.mot	Equation of motion
exact	Exact random vibration analysis including off-diagonal terms

f	Point of the force
imp	Imperfect ring
iso	Isothermal
k	Order of Bessel function
n	n -th mode
$n1, n2$	n_1, n_2
opt	Optimized properties
peak	Term with peak
R	Global coordinate for radial direction
r	Local coordinate for radial direction
s	Sampling point
simple	Only $q=1$ term
TED	Thermoelastic damping
trm	Trimming
z	Coordinate for longitudinal direction
θ	Coordinate for tangential direction
Ω	Rotating
(superscripts)	
thermal	Thermal component for strain

Chapter 1 Introduction

1.1 Background and motivation

The MEMS and NEMS (Micro- and Nano-Electro-Mechanical Systems) are important industrial components in modern technology, such as aerospace, mechanical engineering, *etc.* For the precision parts, the minimalized machineries are strongly required in UAVs (Unmanned Aerial Vehicles) or autonomous cars. Then, the controlling motion is crucial issue in the moving vehicles. In this regard, the gyro sensor can be used to have the stability during the travel in the way. Figs. 1.1 and 1.2 show an actual MEMS beam resonator and the modeling of the resonator with electrode, respectively.

The ring structure is mainly used in various industrial parts, such as sensor or resonator, *etc.* And the model is topologically and geometrically stable and symmetric due to the circularly continuous structure, thus the ring is suitable for the MEMS or NEMS. Moreover, the structure is one of the extension of the simple beam, thus the model can be easily investigated and applied in a various actual purposes. For example, Fig. 1.3 represents a MEMS toroidal ring gyroscope. Moreover, the ring structure can be manufactured by bending thin element easily. In this regard, Figs. 1.4 (a) and (b) show experimental diagrams of an actual models of rings based on a triangular- and circular-cross-sectional nano-wire structures, respectively. While, the circular-cross-section is more popular than any other shapes, thus the toroidal ring can be potentially developable structural model in near

future.

For the vibration, the dissipation can affect the reduction of the efficiency during the motion. Generally, the damping can be classified into the extrinsic and intrinsic attenuations. The example reasons, respectively, of former are the gas, the squeeze-film, the supportings, the eddy-current, *etc.*, and latter are thermoelastic, dipole resonance, and Gilbert's damping due to a spin-pumping in the magnetic field, *etc.* Moreover, the intrinsic dissipation is more difficult to control rather than extrinsic ones due to the scale of the structure. And the thermoelastic damping (TED) is the most important intrinsic attenuation, thus the TED is main issue of the work. In this regard, the vibration mode shapes and temperature distributions are important point for analysis as Fig. 1.5.

The statistical investigation is the relationship between free- and actual forced-vibration models. Typically, the spectral density (SD) is useful to describe the frequency-domain analysis based on Gaussian white noise. The noise is consisted with all continuous frequencies as zero to infinite with the same amplitude, thus the input force can be modeled with generalized characteristic.

Moreover, the imperfection affects the frequency split and irregularity during the motion for the ring model. An addition makes asymmetric modes in the structure, thus the vibration characteristics are separated into two modes due to the distortion. The frequency split makes the inaccuracy for the motion, then the deviation should be corrected to ensure the precision

of the structure. In this regard, the “trimming method” is a simple and suitable way to coincide the split of the frequencies by eliminating the difference.

1.2 Thermoelastic damping

Generally, the attenuation is derived from various kinds of external dissipation mechanisms, such as Coulomb friction [1], viscous damping [2], *etc.* And the classifications of dissipations can be categorized as two major topics as “extrinsic” and “intrinsic” dampings. [3][4] The extrinsic one is related to an external elements of the structure, *e.g.* squeeze-film damping [5], support losses [6], air- or gas-damping [6], surface loss [6], Kelvin-Voigt’s model [7], *etc.* On the other hand, the intrinsic one is originated from material characteristics, such as thermoelastic damping (TED) [8][9], Akhiezer dissipation due to thermal phonons [10], and Gilbert’s damping due to a spin-pumping in the magnetic field [11], *etc.*

Especially, the intrinsic damping is more difficult to control rather than extrinsic ones. And the TED is one of the largest factor of the intrinsic attenuation, thus the damping is dealt with in this work. The dissipation is originated from frictions between multiple molecules during the expansion due to the motion of the structure, and dominant in the micro- or nano-scaled model. [9] In order to express the TED numerically, the quality factor (Q-factor; Q) or the loss factor is mainly used as the ratio of the maximum to loss energies per a cycle. Moreover, the inverse of the Q is frequently adopted to emphasize the loss effect rather than the Q .

Additionally, the velocity of the heat flux is finite in the actual model. In the room temperature or lower frequency, the speed of heat flux can be assumed as infinite, thus the time-lagging can be neglected in classical

Fourier heat conduction equation. [12] However, the time-lagging effect should be considered in the extremely low temperature or higher frequency because the delay of the flux cannot follow the motion (i.e. time-lagging is longer). [13][14] Usually, the TED is sufficiently smaller in nearby 0 [K] rather than the air damping, etc. [15]. The paradox can be compensated by the non-Fourier heat conduction [16][17], thus the work can be applied into the high-frequency atmosphere or extremely low temperature, such as a superconductor. [18][19][20]

As the practical point of view, the optimization can be applied into the topic. One of a useful theorem is the “Debye peak” [9], known as the maximum loss factor (i.e. maximum Q^{-1}). But the peak is useful to avoid the effect due to the imperfection [21]. In this regard, “Debye peak” is discussed to design the ring on the conservative point of view.

Furthermore, the general TED mechanism has been studied by numerous investigators such as: Duwel *et al.* [22] experimentally presented the TED in beam-shaped MEMS gyros. Wong *et al.* [23] proposed the application of the damping mechanism based on Zener’s model. Nayfeh and Younis [24] performed the attenuation of the micro-plate based on the Love’s equation of motion. Sun *et al.* [25] examined the damping for an Euler-Bernoulli beam including non-Fourier heat conduction. Lu *et al.* [26] described the TED of a tubular shell through the thickness direction using Donnell–Mushtari–Vlasov approach. Kim *et al.* [27] considered the damping for a micro-ring with an effect of rotating. Choi *et al.* [28] studied the weak form

of a thermoelasticity based on the virtual-work principle. Sharma [29] discussed the TED of micro- or nano-scaled beam with the non-Fourier heat conduction equation. Guo *et al.* represented the TED of a beam [30] and plate [31] models with dual-phase-lagging for heat flux and temperature distribution. Moreover, Senkal *et al.* [32] studied the parametric drive of a MEMS-integrating toroidal ring gyroscopes. Kim and Kim dealt with the TED for a micro-ring model including local deviations [33] based on Refs. [34] and [35], and rotating ring with point masses [36]. Li *et al.* [37] examined the dissipation for a toroidal solid ring model based on Zener's result. Alghamdi and Youssef [38] analyzed the dual-phase-lagging TED for a rotating micro- or nano-ring model. Fang and Li [39] represented the thermoelastic loss for a micro-ring with two-dimensional heat conduction. Kim *et al.* [40] studied the splitting of the damping for a micro-ring according to lumped masses. Moreover, Kim and Kim presented the difference of the TED from point masses for a toroidal ring [21] and cylindrical shell [41], respectively. And Zhou *et al.* investigated a micro-beam model with rectangular [42] and circular [43] cross-section based on the CV equation.

1.3 Model and vibration analysis

A ring is simple and topologically stable model due to the circular shape based on a smooth-curved beam [44]. And the less space is required rather than the beam with the same stiffness, thus the advantage of the structure is outstanding. Moreover, higher frequency is another significant characteristic, thus the model is suitable to minimize for MEMS or NEMS elements. In this work, Love's equation of motion [36] based on Flugge's strain-displacement relationship, and inextensional theory [45] are mainly used to simplify the analysis with constant centerline during the motion. The theories can be valid in a thin ring based on Euler-Bernoulli's beam model. Furthermore, the vibration mechanism can be classified as in- and out-of-plane [46] motions with respect to the torsional twist motion. However, only the in-plane vibration is analyzed using the expression as two dimensional mode shapes for radial and tangential components.

Basically, Williams [1] presented the equations of motion for a thin ring based on Hamilton's principle. Kirkhope [47] developed the in-plane vibration of the thick ring according to the rotary inertia and shear effects. Endo *et al.* [48] investigated the flexural vibration of a thin ring considering centrifugal and Coriolis forces due to the rotation. Suzuki [49] analyzed the in-plane vibration for the inextensible thick ring. Bickford and Reddy [50] performed the rotational effect on the thick ring. Huang and Soedel [51] proposed the effect of Coriolis acceleration for thick rotating on elastic foundations. Charnley *et al.* [52] discussed the extensional and

inextensional rings with rectangular cross-section considering the torsion. Hong and Lee [34] predicted the effect due to the local deviations with variations for finite mass and stiffness. Eley *et al.* [46] examined the Coriolis coupling on the vibration of a rotating ring with distortion. Ellison and Ahmadi [53] dealt with the passive control of an airborne equipment with a circular ring and concentrated mass. Yoon and Lee [54] extended the study in [34] into the structure including multiple deviations. Bisegna and Caruso [55] discussed frequency split due to imperfections based on a perturbation method. Park *et al.* [35] represented the mode pairs for a ring including multiple local deviations.

And the ring with circular cross-section, known as toroidal ring, is one of potential model for a NEMS resonator. The manufacturing of the toroidal ring is difficult in nowadays for the MEMS, but the model can be potentially established in near future. In this regard, the beams with various cross-sections including circular shape have been studied by numerous investigators such as: Hu *et al.* [56] examined epitaxial semiconducting heterostructures based on triaxial nanowires. Bartolomé *et al.* [57] represented indium-oxide micro-rods with various cross-sections. Anguiano *et al.* [58] demonstrated circular and square micro-pillar resonators within high frequency range. Moreover, the application of the micro- or nano-ring is experimentally investigated based on a beam structure. For example, Pauzauskie *et al.* [59] experimentally represented the nanowire ring resonator with triangular cross-section. Additionally, Gu

et al. [60] introduced a hybrid plasmonic pseudo-ring resonator made with nanowire, which can be assumed as perfect ring. Thus, the toroidal ring can be established easily and freely for the cross-section, then the model can be potentially developable on the MEMS or NEMS. And the analysis of the rectangular-cross-sectional ring is easier than the toroidal ring, but the toroidal one is easier for manufacturing by bending the straight structure.

1.4 Random vibration

For the theoretical studies, the deterministic functions are mainly studied to investigate the vibration characteristics. In this regard, the free vibration is an important issue, then the frequency analysis is mainly discussed as a limitation. On the other hand, the response value of the future time cannot be estimated because an actual case of the input force is non-deterministic [61]. Despite the uncertainty, the averaging procedure based on the statistical regularity can be applied by collecting much enough samples. As a familiar assumption, a general input is consisted with the same amplitude on various range of the frequencies [62] known as “Gaussian white noise”. The distribution is continuous, then the random vibration analysis can be classified using the bandwidth. Then, the average, standard deviation (StDev) or expected maximum of the response can be predicted by the transfer function obtained by using the Laplace transform. [63] The result can be extended to the estimation of the fatigue life, such as [64][65].

In this regard, the random vibration analysis is performed by numerous investigators, such as: Elishakoff and Livshits analyzed the random vibration of Euler-Bernoulli [66] and Timoshenko [67] beam models. Gopalakrishnan *et al.* [68] performed a matrix method for spectrum of wave propagation in multiple-connected Timoshenko beams. Chang [69] presented the analysis of the Timoshenko beam with elastic foundations. Birgersson *et al.* [70] investigated the vibration of plates based on the turbulent boundary layer excitation. Barbato and Conte [71] established the

definitions of spectral characteristics for stationary and non-stationary processes extended to general complex-valued non-stationary random processes. Wang [72] performed the modal analysis on a continuous beam model subject to generic forms of actuation forces and sensing devices. Ricciardi [61] studied the stochastic response of a beam excited by moving loads with random amplitude. Zhang *et al.* [73] formulated the random vibration of a long-span bridge. Araújo and Laier [74] operated transmissibility matrices based on modal analysis of the power spectral density (PSD). Zavoni *et al.* [75] developed a formulation of the modal response for multi-support structures using a random vibration. Moreover, Braccesi *et al.* [76] suggested a frequency-domain criterion for the predicting a damage based on the autocorrelation function (ACF). Awrejcewicz *et al.* [77] proposed the chaotic dynamics and responses of flexible beams due to the white noise. Li *et al.* [78] examined the analysis for a cylindrical shell considering the axial compression.

Additionally, the modal cross-spectral density (cross-SD) is usually neglected when the damping is slight and the neighborhood eigenfrequencies are well separated for the system. However, the cross-SD should be considered in the narrowband random excitation, especially in the vicinity of the eigenfrequency range. [79] In here, an antiresonance is one of the most important effects in the modal analysis, but the direct-SD which is the simplified model by neglecting the coupling effect of the different modes cannot detect the phenomenon because the truncation error

diminished. [80] Thus the comparison between the both SDs are represented in this work.

1.5 Frequency trimming method

Inevitably, actual models including the nonuniformities due to the errors from manufacturing, structural defection, attached devices such as sensors [81], or other factors. [21] The imperfection can be modeled with Rayleigh's quotient [45], by compensation of the limitation in Love's equation of motion. [40] Generally, the imperfection consists with point masses, radial and torsional springs without any masses. For the structural specialty of the circular ring, two vibration mode shapes appear with respect to the distorted angles of orientations. [45] And the eigenfrequencies are bifurcated into two values according to the orientations as "symmetric" and "asymmetric" modes. [35]

In order to correct the split, additional elements are needed to eliminate the bifurcation of the modes. By assuming that the both separated eigenfrequencies are the same, the terms of imperfection can be written as a function of the mass and the angular positions. [45] The general result is an open-ended answer, thus the "trimming" method can be specified as single- or multi-modes [82] and including pre-selected locations. [83] To simplify the analysis in this work, the additional element is only lumped mass without any spring, and the only single-mode trimming is introduced with one additional point mass. And the applications can be classified as: Wang *et al.* [84] investigated the frequency trimming in MEMS resonators by localized filament annealing. Rourke *et al.* [85] proposed the eliminating frequency splits between a pair of in- and out-of-plane modes of imperfect

ring model. Moreover, Kim and Kim [86] studied the trimming method for a hemispherical ring with lumped masses. Behbahani and M'Closkey [87] analyzed the eigenfunctions of the non-uniform ring with perturbation expansions method.

1.6 Thesis scope & outline

In this work, a micro toroidal ring is mainly discussed by the thermoelastic damping, random vibration analysis, and the frequency trimming method. Firstly, the heat conduction equation including the time-lagging effect is introduced to model the thermoelastic damping (TED). The cross-section of the structure is circular, thus the cylindrical coordinate is proper to obtain the temperature profile. Thus, the solutions of the temperature shape are expressed as complex numbers. The maximum-strain- and loss-of-energies are defined as per cycle, and then the ratio known as quality factor (Q-factor) is adopted to describe the characteristics of the ring.

Furthermore, the equation of motion is applied to obtain the eigenfrequency of the model. To compensate the slight imperfection term based on Rayleigh's quotient, the virtual density is assumed as a function of kinetic energy and ordinary material density. In here, vibration mode shapes are assumed as inextensional condition with the constant length of center line, and in-plane motion without torsion. Precisely, the inextensional assumption is inaccuracy in the higher mode because curves of the mode shape appear during the vibration. However, the amplitude goes smaller in the higher mode as shown in the transfer function, thus the assumption can be used to estimate the characteristics of the vibration and TED.

Next, imperfections are described as lumped masses as zero-volume, thus the strain energy is independent to the additions. The virtual density is obtained from the Rayleigh's quotient, and then the result is the function of

the magnitudes and angular positions of the masses. Moreover, the transfer function is obtained to represent the spectral density (SD) in the forced vibration model. In order to simplify the analysis, Gaussian white noise is used as an input function, and the average value of the square-deformation is obtained as estimation of the response.

The basic analysis of the structure is shown as eigenfrequencies with the function of imperfection as the virtual density. Additionally, the TED is investigated as the Q-factor, and linearized as the constant value.

Moreover, the random vibration is studied using the linear damping coefficient, and the trends of the responses are shown graphically. For the first time, the relationship between the input force and output response is expressed using the transfer function via Laplace transform. Then the standard-deviation (StDev) is the same as the square-root of the average of the square deformation when the mean value of the average can be assumed as zero. Then the spectral density (SD) based on the Gaussian white noise is obtained as ideal case of the random vibration analysis. Moreover, the bandwidth of the response is represented by using the spectral moment. Then the number of peaks and zero-cross points, and Crest factor (CF) as a peak factor (PF) can be calculated as the characteristics of the fatigue failure. The optimum design concept of the ring model is represented using the “Debye peak” with the minimum Q-factor. On the other hand, the peak can be usefully investigated as conservative point as insensible characteristic with respect to the imperfection. Moreover, the trimming method is

introduced to control the split frequencies into a single value. Finally, the goal of this work is the explicit form of the peak point for the Q^{-1} on the toroidal micro-ring model.

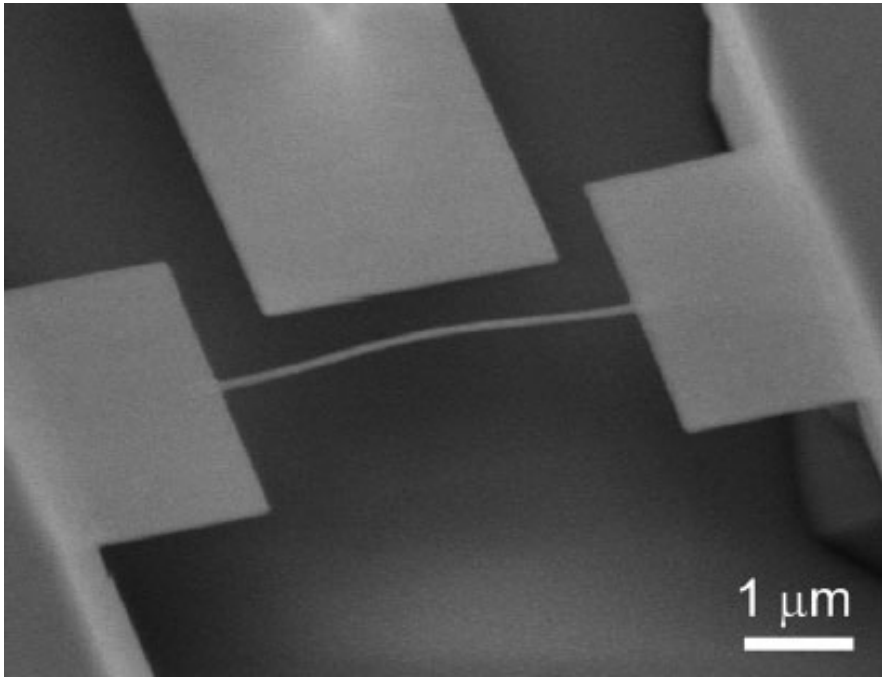


Fig. 1.1 MEMS beam resonator [88]

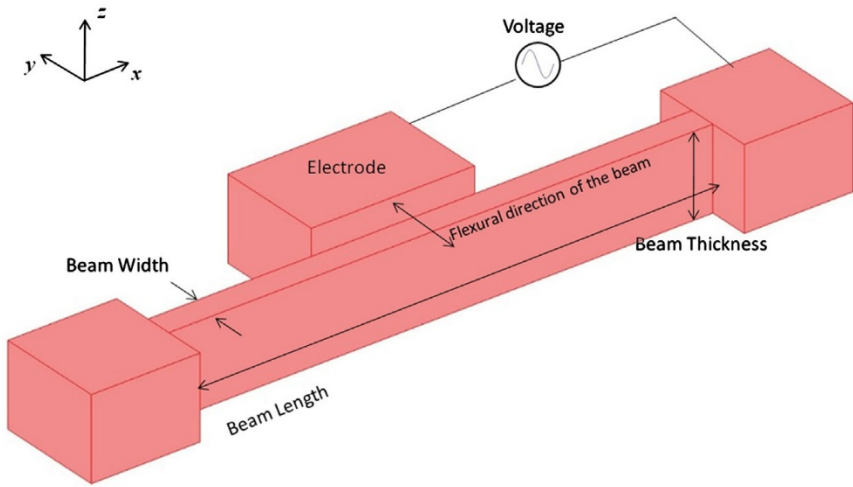


Fig. 1.2 Modeling of a beam resonator with electrode [89]

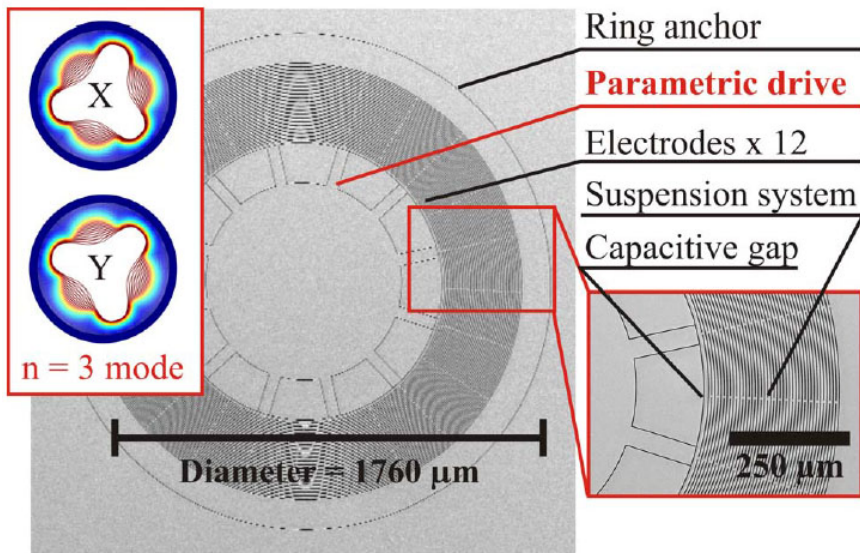
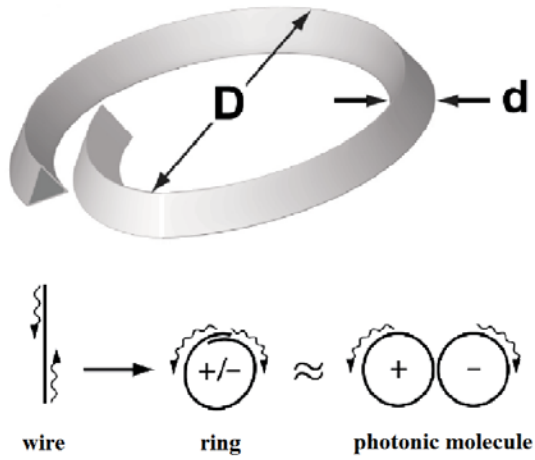
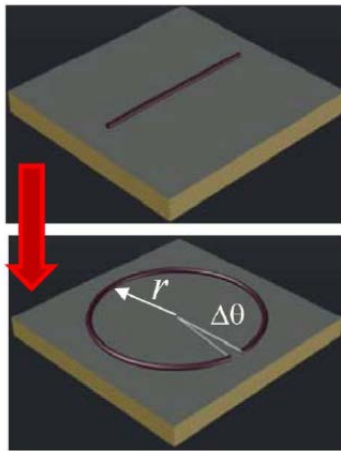


Fig. 1.3 MEMS toroidal ring gyroscope [32]



(a)



(b)

Fig. 1.4 (a) Schematic of ring structures showing the triangular cross-section of the nanowires [59],

(b) Schematic picture of hybrid plasmonic ring-resonator. ($R_0=1000$, $r_0=100$ [nm]) [60]

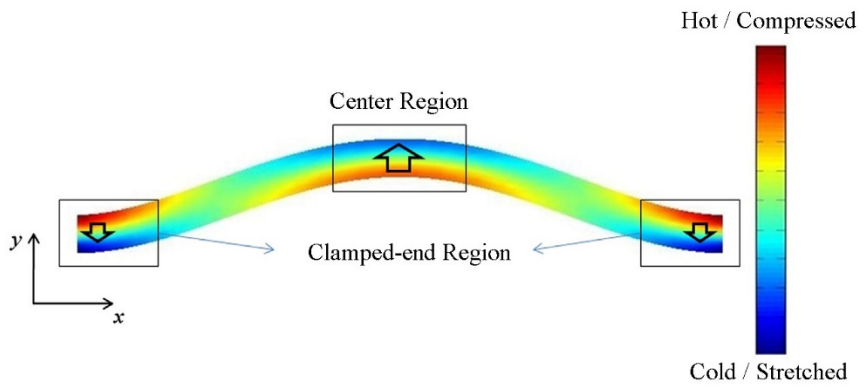


Fig. 1.5 Vibration mode shape and temperature distribution from
COMSOL® [89]

Chapter 2 Thermoelstic damping

2.1 Constitutive equations

Firstly, Cattaneo and Vernotte (CV) [13][14] independently suggested an equation of heat conduction considered a time-lagging with respect to a heat flux vector \mathbf{q} . When the deviation of temperature is small enough, \mathbf{q} can be defined as a gradient of the temperature profile as [12]

$$\mathbf{q} = -k\nabla T_F \quad (2.1.1)$$

Moreover, the gradient of \mathbf{q} is set to a heat conduction equation as

$$\nabla \mathbf{q} = -k\nabla^2 T_F = -C_v \frac{\partial T}{\partial t} - \frac{E\alpha\hat{T}_a}{1-2\nu} \frac{\partial \hat{e}}{\partial t} \quad (2.1.2)$$

where the Laplacian operator and cubic dilatation, respectively, are [37]

$$\nabla^2 = \frac{\partial^2}{\partial R^2} + \frac{1}{R} \frac{\partial}{\partial R} + \frac{1}{R^2} \frac{\partial^2}{\partial \theta^2} + \frac{\partial^2}{\partial z^2} \quad (2.1.3)$$

$$\hat{e} = \varepsilon_\theta + \varepsilon_R + \varepsilon_z \quad (2.1.4)$$

To modify the paradox of infinite velocity peculiar in the classical Fourier's theory, the general heat flux with the time derivative term should be regarded in order to obtain the CV's heat conduction equation, known as a non-Fourier equation, as:

$$\left(1 + \tau_{CV} \frac{\partial}{\partial t}\right) \mathbf{q} = -k \nabla T \quad (2.1.5)$$

where $\nabla T = \left(1 + \tau_{CV} \frac{\partial}{\partial t}\right) \nabla T_F$, and especially $\nabla T = \nabla T_F$ when $\tau_{CV} = 0$ (i.e. classical Fourier heat conduction).

Then, the improved heat conduction equation with the relaxation time τ_{CV} is obtained as:

$$\left(1 + \tau_{CV} \frac{\partial}{\partial t}\right) \nabla \mathbf{q} = -k \nabla^2 T = -\left(1 + \tau_{CV} \frac{\partial}{\partial t}\right) \left(-C_v \frac{\partial T}{\partial t} - \frac{E\alpha \hat{T}_a}{1-2\nu} \frac{\partial \hat{\epsilon}}{\partial t}\right) \quad (2.1.6)$$

in here, C_v and $\frac{E\alpha \hat{T}_a}{1-2\nu}$ are not functions with respect to time.

The micro- or nano-toroidal ring model is presented in Fig. 2.1 with global (R, θ, Z) and local coordinates (x, y, z) with local angle β . And the i -th imperfect masses m_i including the trimming masses are located at $\theta = \theta_i$. Moreover, the effects from the shear deformation and rotary inertia are neglected in order to simplify the model. Then, the variation of temperature field in Eq. (2.1.2) is given as

$$T(R, \theta, z, t) = \hat{T}(R, \theta, z, t) - \hat{T}_a = T_0(R, \theta, z) \exp(j\omega t) \quad (2.1.7)$$

Moreover, the circumferential, radial, and axial strains, respectively, can be represented as [37]

$$\varepsilon_{\theta} = \frac{\sigma_{\theta}}{E} + \varepsilon_{\theta}^{\text{thermal}} \quad (2.1.8a)$$

$$\varepsilon_R = \varepsilon_z = -\frac{\nu\sigma_{\theta}}{E} + \varepsilon_R^{\text{thermal}} \quad (2.1.8b)$$

where the thermal strains are

$$\varepsilon_{\theta}^{\text{thermal}} = \varepsilon_R^{\text{thermal}} = \alpha T(R, \theta, z, t) \quad (2.1.9)$$

The circumferential strain is proportional to the local coordinate x from inextensional assumption, thus

$$\varepsilon_{\theta} = -\frac{x}{R_0^2} \left(\frac{\partial^2 u}{\partial \theta^2} + u \right) \quad (2.1.10)$$

Where the general mode shape as the homogeneous solution can be assumed as

$$u(\theta, t) = A_u \exp(jn\theta + jn\psi_j + j\omega t) \quad (2.1.11)$$

Using Eqs. (2.1.8) to (2.1.6), the circumferential stress can be expressed as

$$\sigma_{\theta} = -\frac{Ex}{R_0^2} \left(\frac{\partial^2 u}{\partial \theta^2} + u \right) - \alpha ET \quad (2.1.12)$$

Substituting Eqs. (2.1.12) to (2.1.6), the detail equation of heat conduction

is

$$\begin{aligned} & \left\{ \chi \nabla^2 - \left(1 + \frac{2(1+\nu)}{1-2\nu} \Delta_E \right) \left(\frac{\partial}{\partial t} + \tau_{CV} \frac{\partial^2}{\partial t^2} \right) \right\} T \\ & = -\frac{\Delta_E}{\alpha} \left(\frac{\partial}{\partial t} + \tau_{CV} \frac{\partial^2}{\partial t^2} \right) \left[\frac{x}{R_0^2} \left(\frac{\partial^2 u}{\partial \theta^2} + u \right) \right] \end{aligned} \quad (2.1.13)$$

in here, $\chi = \frac{k}{c_v}$ as thermal diffusivity $\left[\frac{\text{m}^2}{\text{sec}} \right]$, and $\Delta_E = \frac{E\alpha^2 \hat{r}_a}{c_v} \ll 1$ as the relaxation strength, respectively. The definition of the Δ_E is the relative difference between the adiabatic and isothermal values of Young's modulus [44].

Thus the second term in Eq. (2.1.13) can be reduced as

$$\left\{ \chi \nabla^2 - \left(\frac{\partial}{\partial t} + \tau_{CV} \frac{\partial^2}{\partial t^2} \right) \right\} T = -\frac{\Delta_E}{\alpha} \left(\frac{\partial}{\partial t} + \tau_{CV} \frac{\partial^2}{\partial t^2} \right) \left[\frac{x}{R_0^2} \left(\frac{\partial^2 u}{\partial \theta^2} + u \right) \right] \quad (2.1.14)$$

Using the Laplacian, the specific 3-dimensional heat conduction can be re-written as

$$\begin{aligned} & \chi \left(\frac{\partial^2 T}{\partial R^2} + \frac{1}{R} \frac{\partial T}{\partial R} + \frac{1}{R^2} \frac{\partial^2 T}{\partial \theta^2} + \frac{\partial^2 T}{\partial z^2} \right) - \left(\frac{\partial T}{\partial t} + \tau_{CV} \frac{\partial^2 T}{\partial t^2} \right) \\ & = -\frac{\Delta_E}{\alpha} \left(\frac{\partial}{\partial t} + \tau_{CV} \frac{\partial^2}{\partial t^2} \right) \left[\frac{x}{R_0^2} \left(\frac{\partial^2 u}{\partial \theta^2} + u \right) \right] \end{aligned} \quad (2.1.15)$$

From the component of radial coordinate, $R = R_0 + x$ [37], then

$$\begin{aligned}
& \chi \left(\frac{\partial^2 T}{\partial x^2} + \frac{1}{R_0+x} \frac{\partial T}{\partial x} + \frac{1}{(R_0+x)^2} \frac{\partial^2 T}{\partial \theta^2} + \frac{\partial^2 T}{\partial z^2} \right) - \left(\frac{\partial T}{\partial t} + \tau_{CV} \frac{\partial^2 T}{\partial t^2} \right) \\
& = -\frac{\Delta_E}{\alpha} \left(\frac{\partial}{\partial t} + \tau_{CV} \frac{\partial^2}{\partial t^2} \right) \left[\frac{x}{R_0^2} \left(\frac{\partial^2 u}{\partial \theta^2} + u \right) \right]
\end{aligned} \tag{2.1.16}$$

The radius is sufficiently larger than the thickness, then the 1st order differential term $\frac{1}{R_0+x} \frac{\partial T}{\partial x}$ can be neglected [17], and $R_0 + x \cong R_0$, thus

$$\begin{aligned}
& \chi \left(\frac{\partial^2 T}{\partial x^2} + \frac{1}{R_0^2} \frac{\partial^2 T}{\partial \theta^2} + \frac{\partial^2 T}{\partial z^2} \right) - \left(\frac{\partial T}{\partial t} + \tau_{CV} \frac{\partial^2 T}{\partial t^2} \right) \\
& = -\frac{\Delta_E}{\alpha} \left(\frac{\partial}{\partial t} + \tau_{CV} \frac{\partial^2}{\partial t^2} \right) \left[\frac{x}{R_0^2} \left(\frac{\partial^2 u}{\partial \theta^2} + u \right) \right]
\end{aligned} \tag{2.1.17}$$

where the separation of the time variable in the temperature profile as

$$T = T(x, z, \theta, t) = T_0(x, z, \theta) \exp(j\omega t) \tag{2.1.18}$$

And the general coordinate transformation is represented as

$$\begin{cases} x \\ z \end{cases} = r \begin{cases} \sin(\beta) \\ \cos(\beta) \end{cases} \tag{2.1.19a,b}$$

Substituting Eqs. (2.1.18) and (2.1.19) into Eq. (2.1.17), thus

$$\begin{aligned}
& \chi \left(\frac{\partial^2 T}{\partial r^2} + \frac{1}{r} \frac{\partial T}{\partial r} + \frac{1}{r} \frac{\partial^2 T}{\partial \beta^2} + \frac{1}{R_0^2} \frac{\partial^2 T}{\partial \theta^2} \right) - \left(\frac{\partial T}{\partial t} + \tau_{CV} \frac{\partial^2 T}{\partial t^2} \right) \\
& = -\frac{\Delta_E}{\alpha} \left(\frac{\partial}{\partial t} + \tau_{CV} \frac{\partial^2}{\partial t^2} \right) \left[\frac{r \sin(\beta)}{R_0^2} \left(\frac{\partial^2 u}{\partial \theta^2} + u \right) \right]
\end{aligned} \tag{2.1.20}$$

The coordinate of Eq. (2.1.18) can be transformed as

$$T(r, \beta, \theta, t) = T_0(r, \beta, \theta) \exp(j\omega t) \quad (2.1.21)$$

Moreover, the boundary condition (BC) as no heat flux on the surface of the ring as

$$\frac{\partial T_0}{\partial r} = 0 \text{ at } r = r_0 \quad (2.1.22)$$

And the continuity condition of the circumferential coordinate is

$$T_0(r, \beta, \theta) = T_0(r, \beta, \theta + 2\pi) \quad (2.1.23)$$

The radial displacement is given in Eq. (2.1.11), thus Eq. (2.1.20) can be re-arranged as

$$\begin{aligned} & \chi \left(\frac{\partial^2 T_0}{\partial r^2} + \frac{1}{r} \frac{\partial T_0}{\partial r} + \frac{1}{r} \frac{\partial^2 T_0}{\partial \beta^2} + \frac{1}{R_0^2} \frac{\partial^2 T_0}{\partial \theta^2} \right) - (j\omega_n - \tau_{CV}\omega^2) T_0 \\ & = -(j\omega - \tau_{CV}\omega^2) \frac{4E}{\alpha} \frac{r \sin(\beta)}{R_0^2} (1 - n^2) \hat{U}_n \sin(n\theta) \end{aligned} \quad (2.1.24)$$

2.2 Solution of the heat conduction equation: Temperature profile

In the previous section, the governing equation of thermoelastic dissipation is obtained with harmonic vibration. The solution of the temperature profile expressed by cylindrical coordinate can be described by “ k -th order Bessel Function of 1st kind” as [37]

$$T_0(r, \beta, \theta) = \sum_{m=0}^{\infty} \sum_{k=0}^{\infty} \sum_{q=1}^{\infty} J_k \left(\frac{a_{kq}}{r_0} r \right) \left[\begin{array}{l} A_{kqm} \sin(k\beta) \\ + B_{kqm} \cos(k\beta) \end{array} \right] \sin(m\theta) \quad (2.2.1)$$

Substituting Eq. (2.2.1) to Eq. (2.1.24), then $A_{kqm} \equiv C_{1qm}$ remains when $k = 1$ only, otherwise all A_{kqm} and B_{kqm} terms diminish. Then the temperature profile is

$$T_0(r, \beta, \theta) = \sum_{m=0}^{\infty} \sum_{q=1}^{\infty} J_1 \left(\frac{a_{1q}}{r_0} r \right) [C_{1qm} \sin(\beta)] \sin(m\theta) \quad (2.2.2)$$

In here, C_{1qm} is a constant, which can be obtained by substituting the BC into (2.2.2). Thus, multiplying $r J_1 \left(\frac{a_{1q}}{r_0} r \right) \sin(\beta) \sin(n\theta)$ into the Equation, and the integrating from $(0,0,0)$ to $(2\pi, 2\pi, r_0)$ through (θ, β, r) , respectively, then the coefficient when $m = n$ is obtained as

$$C_{1qn} = \frac{2r_0}{R_0^2} \frac{\Delta_E (1-n^2) \bar{U}_n}{\alpha} \frac{1}{(a_{1q}^2 - 1) J_1(a_{1q})} \frac{(j\omega - \tau_{CV} \omega^2) \tau_q}{1 + g(j\omega - \tau_{CV} \omega^2) \tau_q} \quad (2.2.3a)$$

$$C_{1qn} = 0 \quad (m \neq n) \quad (2.2.3b)$$

where Eq. (2.2.3b) occurs due to the orthogonality of $\sin(m\theta)$ and

$$\sin(n\theta). \text{ And } g \equiv g(a_{1q}, n, r_0, R_0) = \left(\frac{nr_0}{a_{1q}R_0} \right)^2.$$

Furthermore, a_{1q} can be numerically obtained from the BC, thus (all terms independent with r are omitted)

$$\frac{\partial}{\partial r} \left[J_1 \left(\frac{a_{1q}}{r_0} r \right) \right]_{r=r_0} = \frac{a_{1q}}{2r_0} [J_0(a_{1q}) - J_2(a_{1q})] = 0 \quad (2.2.4)$$

Table 2.1 shows the results of first 5 terms and some more for a_{1q} .

Substituting Eq. (2.2.3a) into Eq. (2.2.2), then

$$\begin{aligned} T_0(r, \beta, \theta) &= \frac{2r_0}{R_0^2} \frac{\Delta E(1-n^2)\bar{U}_n}{\alpha} \sin(\beta) \sin(n\theta) \\ &\times \sum_{q=1}^{\text{inf}} \left[\frac{J_1\left(\frac{a_{1q}}{r_0}r\right)}{(a_{1q}^2-1)J_1(a_{1q})} \frac{(j\omega - \tau_{CV}\omega^2)\tau_q}{1+g(j\omega - \tau_{CV}\omega^2)\tau_q} \right] \end{aligned} \quad (2.2.5)$$

where τ_q is the relaxation time, the thermal diffusion time through the thickness coordinate [9], as

$$\tau_q = \frac{1}{\chi} \left(\frac{r_0}{a_{1q}} \right)^2 \quad (2.2.6)$$

Furthermore, the Real and Imaginary parts of Eq. (2.2.5) can be easily re-written as

$$\left. \begin{array}{l} \{\text{Real}[T_0(r, \beta, \theta)]\} \\ \{\text{Imag}[T_0(r, \beta, \theta)]\} \end{array} \right\} = \frac{2r_0 \Delta_E (1-n^2) \hat{U}_n}{R_0^2 \alpha} \sin(\beta) \sin(n\theta) \times$$

$$\sum_{q=1}^{\infty} \left[\frac{J_1\left(\frac{a_1 q r}{r_0}\right)}{(a_1 q^2 - 1) J_1(a_1 q)} \times \frac{\{\mathbf{A1}\}}{\{1 + g - \tau_{CV}(\omega^2 \tau_q)\}^2 + (\omega \tau_q)^2} \right] \quad (2.2.7)$$

where

$$\{\mathbf{A1}\} = \left\{ \begin{array}{l} (\omega \tau_q)^2 \left(1 - g \frac{\tau_{CV}}{\tau_q}\right) - \omega^2 \tau_{CV} \tau_q (1 - \omega^2 \tau_{CV} \tau_q) \\ (1 + g) \omega \tau_q \end{array} \right\}.$$

2.3 Quality factor

The definition of the quality factor (Q-factor) is the ratio of maximum energy to dissipated energy during a cycle, thus the form can be described as [37]

$$\frac{1}{Q_{\text{TED}}} = \frac{1}{2\pi} \frac{\Delta W}{W_{\text{max}}} \quad (2.3.1)$$

The max. elastic energy stored in the ring structure, and energy loss per cycle from TED, respectively, are

$$W_{\text{max}} = \frac{1}{2} \iiint_V \sigma_{\theta} \varepsilon_{\theta} dV = \frac{1}{2} \iiint_V \sigma_{\theta} \varepsilon_{\theta} (R_0 + x) dS d\theta \quad (2.3.2a)$$

$$\begin{aligned} \Delta W &= -\pi \iiint_V \sigma_{\theta} \text{Imag}[\varepsilon_{\theta}^{\text{thermal}}] dV \\ &= -\pi \iiint_V \sigma_{\theta} \text{Imag}[\alpha T_0] dV \end{aligned} \quad (2.3.2b)$$

And the damping is sufficiently small, the strain and stress can be reduced in order to calculate easily, thus

$$\varepsilon_{\theta} \approx \frac{\sigma_{\theta}}{E} \quad (2.3.3a)$$

$$\sigma_{\theta} \approx -\frac{Ex}{R_0^2} \left(\frac{\partial^2 u}{\partial \theta^2} + u \right) \quad (2.3.3b)$$

Substituting Eqs. (2.2.7b), and (2.3.3) into Eq. (2.3.2), then

$$\begin{aligned}
W_{\max} &= \frac{1}{2} \iiint_V \sigma_{\theta} \varepsilon_{\theta} (R_0 + x) dS d\theta = \\
&\frac{E}{2} \left[\frac{(1-n^2) \hat{U}_n}{R_0^2} \right]^2 \int_{x=-r_0}^{x=+r_0} \int_{z=-\sqrt{r_0^2-x^2}}^{z=+\sqrt{r_0^2-x^2}} x^2 (R_0 + x) dz dx \\
&\times \int_{\theta=0}^{\theta=2\pi} [\sin(n\theta)]^2 d\theta = \frac{\pi E I R_0}{2} \left[\frac{(1-n^2) \hat{U}_n}{R_0^2} \right]^2 \quad (2.3.4a)
\end{aligned}$$

$$\begin{aligned}
\Delta W &= -\pi \iiint_V \sigma_{\theta} \text{Imag}[\alpha T_0] dV = 2\pi E r_0 \Delta_E \left[\frac{(1-n^2) \hat{U}_n}{R_0^2} \right]^2 \\
&\times \sum_{q=1}^{\inf} \left[\int_{r=0}^{r=r_0} \frac{1}{(a_{1q}^2-1) J_1(a_{1q})} \left\{ \frac{(1+g)\omega\tau_q}{\left\{ \frac{1+g}{-\tau_{CV}(\omega^2\tau_q)} \right\}^2 + (\omega\tau_q)^2} \right\} r^2 J_1\left(\frac{a_{1q}}{r_0} r\right) dr \right] \\
&\times \int_{\theta=0}^{\theta=2\pi} \{R_0 + r \sin(\beta)\} [\sin(\beta)]^2 d\beta \times \int_{\theta=0}^{\theta=2\pi} [\sin(n\theta)]^2 d\theta \\
&= W_{\max} \sum_{q=1}^{\inf} \left[\frac{2\pi \Delta_E \frac{8}{a_{1q}^2(a_{1q}^2-1)}}{\left\{ \frac{1+g}{-\tau_{CV}(\omega^2\tau_q)} \right\}^2 + (\omega\tau_q)^2} \right] \quad (2.3.4b)
\end{aligned}$$

Using Eq. (2.3.1), the Q-factor can be re-written as

$$\frac{1}{Q_{\text{TED}}} = \sum_{q=1}^{\inf} \left[b_{1q} \Delta_E \frac{(1+g)\omega\tau_q}{\left\{ \frac{1+g}{-\tau_{CV}(\omega^2\tau_q)} \right\}^2 + (\omega\tau_q)^2} \right] \quad (2.3.5)$$

where $b_{1q} = \frac{8}{a_{1q}^2(a_{1q}^2-1)}$, and $\tau_q = \frac{1}{\chi} \left(\frac{r_0}{a_{1q}} \right)^2 = \frac{c_v}{k_0} \left(\frac{r_0}{a_{1q}} \right)^2$.

This is the expression of the function of the eigenfrequency.

Moreover, $b_{11} = 0.987 \approx 1$ when $q = 1$ as a simplification, and other

b_{1q} s ($q > 1$) can be neglected, thus

$$\frac{1}{Q_{\text{TED.Simple}}} = \Delta_E \frac{(1+g)\omega\tau_1}{\{1+g-\tau_{\text{CV}}(\omega^2\tau_1)\}^2+(\omega\tau_1)^2} \quad (2.3.6)$$

Where the relaxation time $\tau_1 = \frac{1}{\chi} \left(\frac{r_0}{a_{11}} \right)^2 = \frac{c_v}{k_0} \left(\frac{r_0}{a_{11}} \right)^2 = 0.294989 \frac{c_v r_0^2}{k_0}$.

Additionally, the peak of the Q^{-1} is one of the most important factor for the optimization or design to avoid higher dissipation. For a beam based on the Zener's model [8], the single peak appears as

$$\frac{Q^{-1}}{\Delta_E B_n} = \frac{\omega\tau}{1+(\omega\tau)^2} \quad (2.3.7)$$

By solving $\frac{\partial}{\partial \omega} \left(\frac{Q^{-1}}{\Delta_E B_n} \right) = 0$, thus $\omega\tau = 1$ can be obtained easily.

Moreover, the $Q_{\text{TED.Simple}}$ as the present work is stated in Eq. (2.3.6), then

the differential is similarly performed as $\frac{\partial}{\partial \omega} \left(\frac{(Q_{\text{TED.Simple}})^{-1}}{\Delta_E} \right) = 0$ and the

normalized lagging time $\beta_{\text{CV}} = \frac{\tau_{\text{CV}}}{\tau_1}$, thus the frequency of the peak

$(Q_{\text{TED.Simple}})^{-1}$ is [42][43]

$$(\omega_{\text{peak},n})^2 = \frac{1}{\tau_{\text{CV}}^2} \frac{f(\beta_{\text{CV}})}{6\beta_{\text{CV}}} \quad (2.3.8)$$

with

$$\beta_{CV} \times f(\beta_{CV}) = 2\beta_{CV}(1 + g) - 1 + \sqrt{(2\beta_{CV} - 1)^2 + 12\beta_{CV}^2 + 4g(8\beta_{CV}^2 - \beta_{CV} + 4\beta_{CV}^2 g)} \quad (2.3.9)$$

Substituting Eq. (2.3.8) into Eq. (2.3.6), the peak of $(Q_{\text{TED.Simple}})^{-1}$ is

$$\frac{1}{Q_{\text{TED.Simple}}} = \Delta_E \frac{\{1+g\} \sqrt{\frac{f(\beta_{CV})}{6\beta_{CV}}}}{\left\{1+g-\frac{f(\beta_{CV})}{6}\right\}^2 + \frac{f(\beta_{CV})}{6\beta_{CV}}} \quad (2.3.10)$$

The peak value of $(Q_{\text{TED.Simple}})^{-1}$ is not longer $0.5\Delta_E$ based on Zener's model [8] because of the time lagging. In here, g is the unique term of the toroidal ring. The result is much similar to the Ref. [42][43] when g is neglected, thus the results of the thin ring and beam are the same forms.

Moreover, the simple approximations of Eq. (2.3.9) can be obtained by using Taylor's expansion and limitation forward infinity into $f(\beta_{CV})$ as:

$$f(\beta_{CV}) \approx 6\beta_{CV}(1 + g)^2 \text{ for small } \beta_{CV} \quad (2.3.11a)$$

$$\lim_{\beta_{CV} \rightarrow \text{inf}} \{f(\beta_{CV})\} = 6(1 + g) \text{ for large } \beta_{CV} \quad (2.3.11b)$$

Substituting these results into Eqs. (2.3.8) and (2.3.10), thus the peak

frequencies and the values of Q^{-1} s are:

$$(\omega_{\text{peak},n})^2 = \frac{1}{\tau_{\text{CV}}^2} (1 + g)^2 \text{ for small } \beta_{\text{CV}} \quad (2.3.12a)$$

$$(\omega_{\text{peak},n})^2 = \frac{1}{\tau_{\text{CV}}^2 \beta_{\text{CV}}} (1 + g) \text{ for large } \beta_{\text{CV}} \quad (2.3.12b)$$

$$\frac{1}{Q_{\text{TED.Simple}}} = \Delta_E \frac{1}{[1 - \beta_{\text{CV}}(1+g)]^2 + 1} \text{ for small } \beta_{\text{CV}} \quad (2.3.13a)$$

$$\frac{1}{Q_{\text{TED.Simple}}} = \Delta_E \sqrt{\beta_{\text{CV}}(1+g)} \text{ for large } \beta_{\text{CV}} \quad (2.3.13b)$$

The results are summarized in Table 2.2.

Additionally, the single-phase-lagging time τ_{CV} is suggested for the material properties as [12]

$$\tau_{\text{CV}} = \frac{\chi}{V_C^2/3} = \frac{\chi}{(V_{2\text{nd}})^2} \quad (2.3.14)$$

In here, $V_C = \sqrt{E/\rho}$ is the velocity of the general phonon in the medium, known as the “first” or “ordinary” sound velocity. Furthermore, $V_{2\text{nd}}$ is the finite speed of the heat propagation, so called as the “second” sound velocity. Both normally hearable sound and heat are much similar waves, thus $V_{2\text{nd}}$ can be regarded as another acoustics. This is the key difference between the classical Fourier’s and non-Fourier (i.e. CV’s) heat conduction models [12].

Fig. 2.2 shows the normalized Q^{-1} based on Eqs. (2.3.5) as the summation

and (2.3.6) as $q = 1$ only, respectively. In the model, $R_0 = 10[\mu\text{m}]$ and the range of r_0 is $10^{-7.5}$ to $10^{-5.5}$, respectively. The summation of Q^{-1} is the main factor of the TED, and the case of $q = 1$ can be represented as the simplification. And the Zener's model (i.e. neglected non-Fourier effect) can be valid when the radial thickness is small, but the result on the thick ring is not accurate more than the peak, known as "Debye peak".

Fig. 2.3 shows the elements of the TED with respect to various qs for the same model. In each mode of q , there is only single peak, and the summation of the TED makes multiple peaks when the ring is thick. And large β_{CV} causes the peaks more significantly with respect to the q [43].

Fig. 2.4 represents the percentage difference of the Q^{-1} in only $q = 1$ according to the summation of Q^{-1} . As shown in Fig. 2.1, thinner ring than the peak shows much little difference. On the other hand, the difference goes larger when the ring is much thicker than the peak point.

Fig. 2.5 shows the peak frequency ($\omega_{\text{peak},n}$) based on Eq. (2.3.8). And

Fig. 2.6 presents the normalized $(Q_{\text{TED,Simple}})^{-1} A_E$ for the 3-D and 2-D rings. The mode number $n = 20$, and the global radius is 1000 [nm]. For the thin ring with $r_0 \rightarrow 0$, both graphs are the same as [42] [43] for beam models. The final expression of the beam is strictly different from present work with thin ring, but the process of non-dimensionalization is exactly the same. When the ring is thick, the peak frequency goes larger due to the effect of the thickness. As represented in (b), the $(Q_{\text{TED,Simple}})^{-1}$ is

nearby $0.5\Delta_E$ when the lagging time is short or unconsidered [9][23]. On the contrary, the lagging time is long, $(Q_{\text{TED.Simple}})^{-1}$ goes extremely larger for the thick structure.

Fig. 2.7 shows the plots of Eq. (3.3.11) with $f(\beta_{CV})$ for rings as $\frac{r_0}{R_0} = 0$ (i.e. beams with rectangular [42] or circular [43] cross-sections, or 2-D ring), 0.05, and 0.1 with $n = 20$, and the approximations. As stated in the paragraph, the approximations as $g = 0$ for beam and thin ring models can be compared in here. Moreover, the special term in the 3-D toroidal ring model can be affect the deviation of the $f(\beta_{CV})$, and the range are moved toward smaller β_{CV} . Then, Eq. (2.3.11) can be used in small or large β_n for the 3-D ring too. However, the inflection point is the function of g , thus the range of the curve should be checked to ensure the accuracy of the simplification.

2.4 Damping coefficient for random vibration

To simplify the expression of the transform function, the damping coefficient can be equivalently linearized as c proportional with respect to the velocity. In here, the external force is much larger than the intrinsic dissipation, the energy loss per cycle can be expressed as an integral term. From the basic equation of motion and chain rule, the dissipated energy in one cycle is [91]

$$\begin{aligned}\Delta W_{\text{eq.mot.}} &= \oint [F_{\text{damping}}] dx = \int_{\theta=0}^{2\pi} \int_{t=0}^{\frac{2\pi}{\omega}} [-c(n^2 + 1)\dot{u}] \left(\frac{dx}{dt}\right) dt d\theta \\ &= -c(n^2 + 1) \int_{\theta=0}^{2\pi} \int_{t=0}^{\frac{2\pi}{\omega}} (\dot{u})^2 dt d\theta\end{aligned}\quad (2.4.1)$$

Substituting the mode shape into Eq. (2.4.1), and then

$$\begin{aligned}\Delta W_{\text{eq.mot.}} &= -c(n^2 + 1) \int_{\theta=0}^{2\pi} \int_{t=0}^{\frac{2\pi}{\omega}} [(j\omega)\widehat{U}^2\{\sin(n\theta)\}^2 |\exp(j\omega t)|^2] dt d\theta \\ &= 2\pi^2(n^2 + 1)\widehat{U}^2 c\omega\end{aligned}\quad (2.4.2)$$

From the TED equation, Eqs. (2.3.4b) and (2.4.2) are the same, thus the damping coefficient $\left[\frac{\text{kg}}{\text{sec}}\right]$ is

$$c = c(\omega) = \frac{EI}{2\omega R_0^3} \frac{(1-n^2)^2}{(1+n^2)}$$

$$\times \sum_{q=1}^{\text{inf}} \left[\frac{8\Delta_E}{a_1 q^2 (a_1 q^2 - 1)} \frac{\{1+g\}\omega\tau_1}{\{1+g-\tau_{CV}(\omega^2\tau_1)\}^2 + (\omega\tau_1)^2} \right] \quad (2.4.3)$$

As shown in here, the damping coefficient is a function of the eigenvalue and input frequency. Moreover, the modified damping coefficient goes lower when the eigenfrequency is much higher. The assumption and result are well agreement with the general damping, such as Coulomb friction, *etc.* Fig. 2.8 shows the damping coefficient of the ring with respect to the radial thickness. To simplify the data, q is investigated only 1 in this Figure. As stated in former Section, the results from CV's equation can be valid when the ring is thin. However, the damping coefficient goes smaller when the ring is thicker more than the peak due to the time-lagging.

2.5 Normalized temperature profile

To simplify the analysis, the non-dimensional parameters of the frequency, the lagging time, and the radius are adopted as [43]

$$\widehat{\Omega}_{nq} = \omega\tau_q, \quad \hat{t} = \frac{\tau_{cv}}{\tau_q}, \quad \widehat{R} = \frac{r}{r_0} \quad (2.5.1a,b,c)$$

Then, the normalized Real and Imaginary parts of the Eq. (2.2.7) are

$$\begin{aligned} \left\{ \begin{array}{l} \text{Real}[\widehat{T}_0(r, \beta, \theta)] \\ \text{Imag}[\widehat{T}_0(r, \beta, \theta)] \end{array} \right\} &= \left\{ \begin{array}{l} \text{Real}[T_0(r, \beta, \theta)] \\ \text{Imag}[T_0(r, \beta, \theta)] \end{array} \right\} / \left(\frac{2r_0}{R_0^2} \frac{\Delta_E(1-n^2)\bar{U}_n}{\alpha} \right) \\ &= \sin(\beta) \sin(n\theta) \times \sum_{q=1}^{\text{inf}} \left[\frac{J_1(a_{1q}\widehat{R})}{(a_{1q}^2-1)J_1(a_{1q})} \frac{\{\mathbf{A2}\}}{(1+g-\widehat{\Omega}_{nq}^2\hat{t})^2 + \widehat{\Omega}_{nq}^2} \right] \end{aligned} \quad (2.5.2)$$

where

$$\{\mathbf{A2}\} = \left\{ \begin{array}{l} \widehat{\Omega}_{nq}^2(1-g\hat{t}) - \widehat{\Omega}_{nq}^2\hat{t}(1-\widehat{\Omega}_{nq}^2\hat{t}) \\ \widehat{\Omega}_{nq}(1+g) \end{array} \right\} \quad (2.5.3)$$

In here, the results in the notation “ Σ ” are similar to the case of a beam [13] with circular cross-section for $g = 0$. And the entire results without \hat{t} terms are the same as the case of the toroidal ring with classical Fourier heat conduction [53].

Fig. 2.9 shows the non-dimensionalized temperature profiles obtained from Eq. (2.5.2). The time lagging effect makes the delay of the heat flux, known

as the definition of the non-Fourier heat conduction. When the NF is neglected as [37], the temperature profile is exactly flat. But the delay can be visualized by swells on the temperature profiles. Moreover, both “Real” and “Imag” parts of the surfaces are symmetric with respect to the centerline due to the inextensional condition.

Table 2.1 Solutions of the Bessel function

q	a_{1q}	$\frac{a_{1q}}{q\pi}$	$K_{1q} = \frac{8}{a_{1q}^2(a_{1q}^2-1)}$
1	1.841177	0.586065	0.987444
2	5.331456	0.848528	0.010263
3	8.536351	0.905735	0.001528
4	11.70600	0.931534	0.000429
5	14.86358	0.946245	0.000165
10	30.60192	0.974090	9.13E-06
20	62.03233	0.987275	5.40E-07
50	156.2886	0.994964	1.34E-08
100	313.3711	0.997491	8.30E-10
infinite	$q\pi$	1.000000	$\frac{8}{(q\pi)^4-(q\pi)^2} \rightarrow 0$

Table 2.2 Comparisons of the approximations

	for small β_{CV}	for large β_{CV}
$f(\beta_{CV})$ Eq. (2.3.11)	$6\beta_{CV}\{1+g\}^2$	$6\{1+g\}$
$(\omega_{\text{peak},n})^2$ Eq. (2.3.12)	$\frac{1}{\tau_{CV}^2}\{1+g\}^2$	$\frac{1}{\tau_{CV}^2\beta_{CV}}\{1+g\}$
$\frac{1}{Q_{\text{TED,Simple}}\Delta_E}$ Eq. (2.3.13)	$\frac{1}{[1-\beta_{CV}\{1+g\}]^2+1}$	$\sqrt{\beta_{CV}\{1+g\}}$

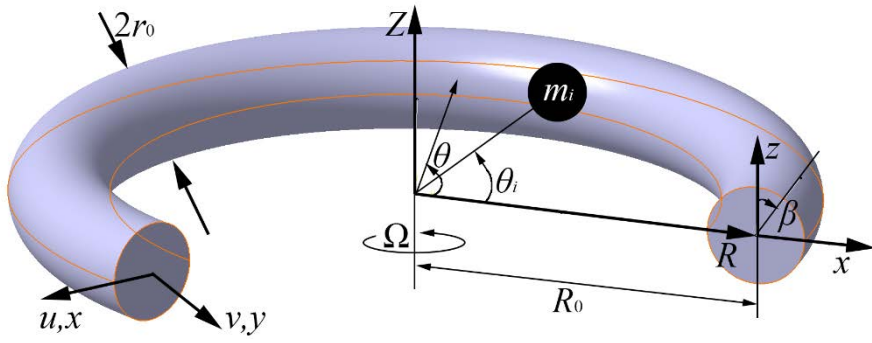


Fig. 2.1 Toroidal ring model

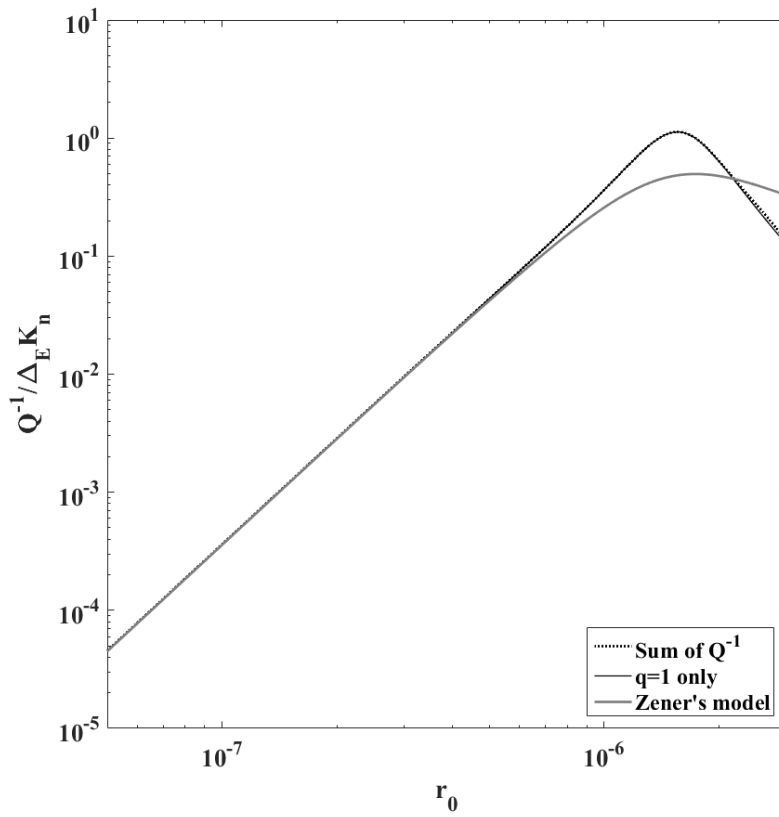


Fig. 2.2 Q^{-1} with respect to r_0

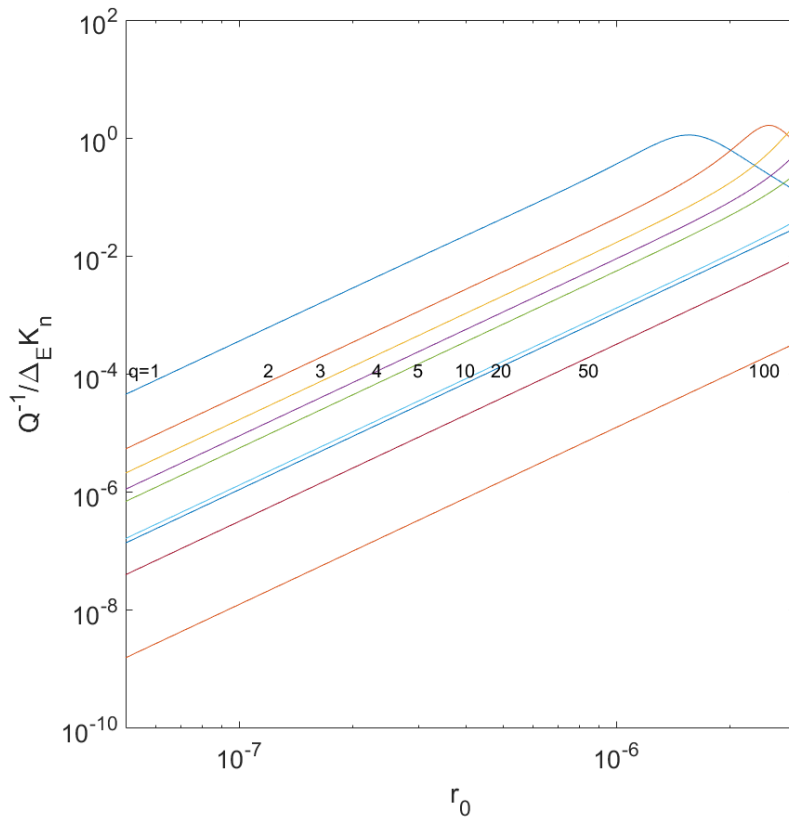


Fig. 2.3 Each component of Q^{-1} with respect to r_0

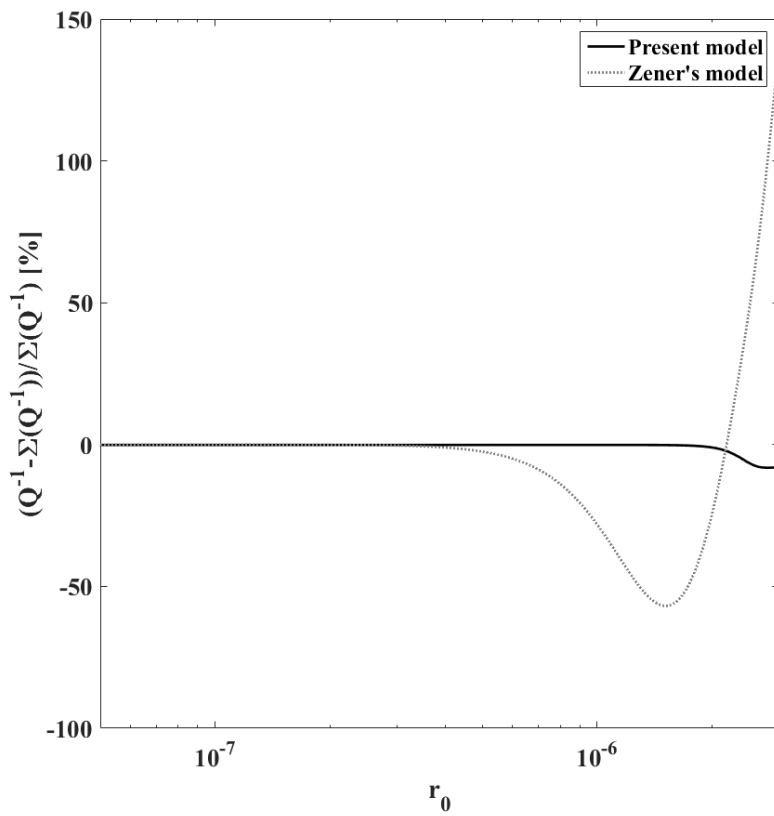


Fig. 2.4 % difference of Q^{-1} for summation and $q = 1$ only

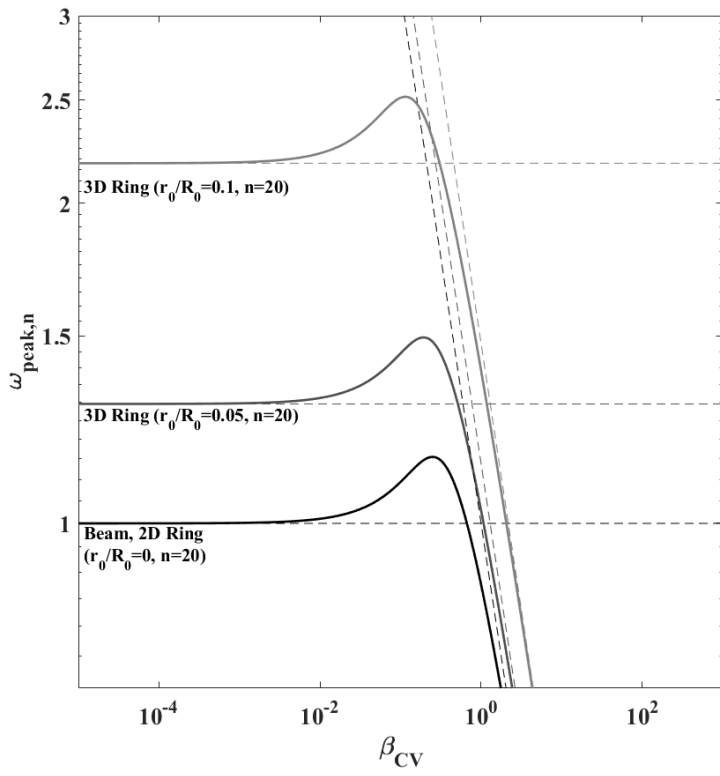


Fig. 2.5 Peak frequencies with respect to β_{CV}

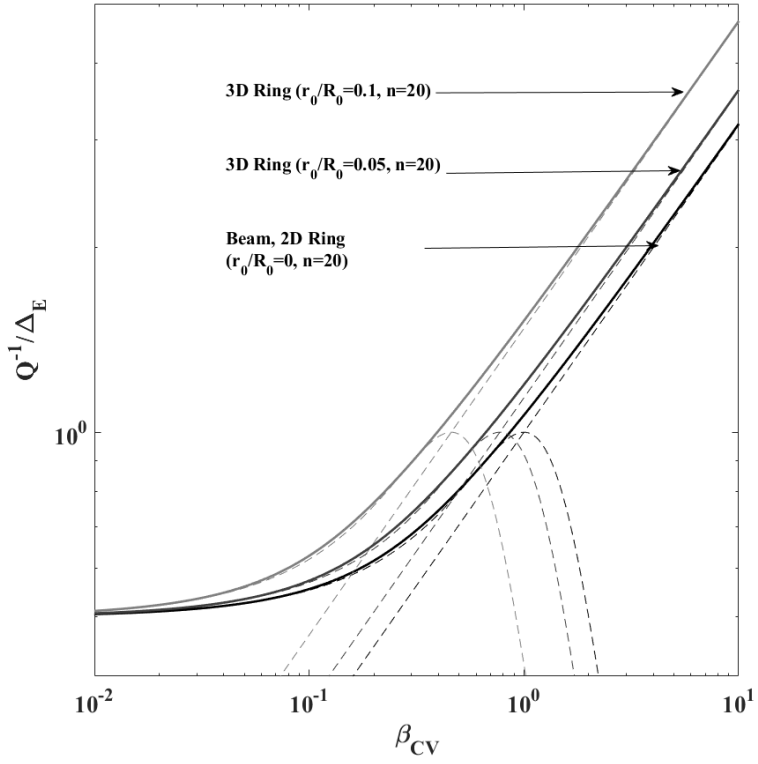


Fig. 2.6 Q^{-1} on the peak frequencies

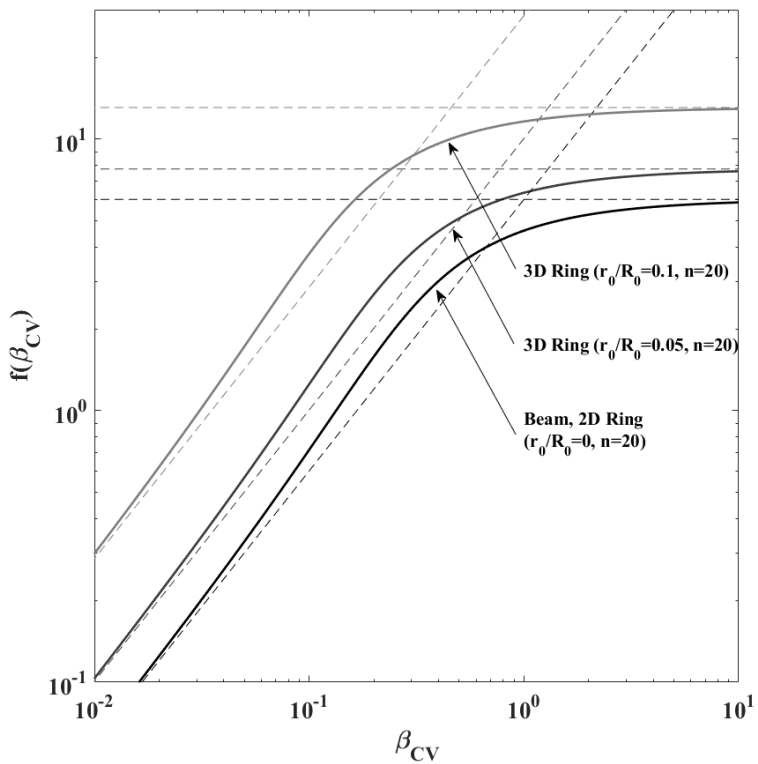


Fig. 2.7 Function $f(\beta_{CV})$ with respect to β_{CV}

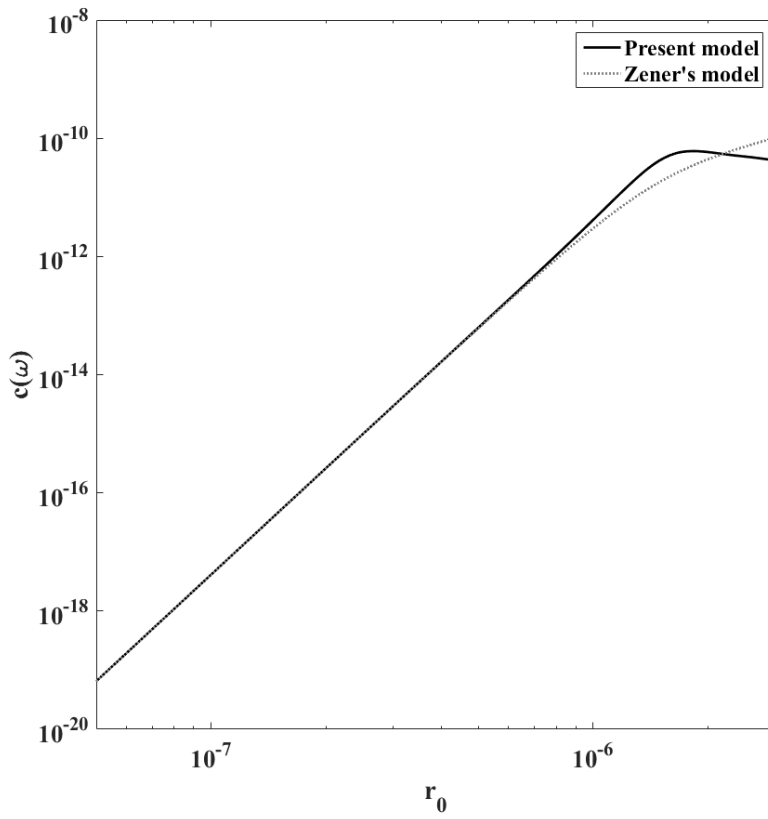


Fig. 2.8 Damping coefficients

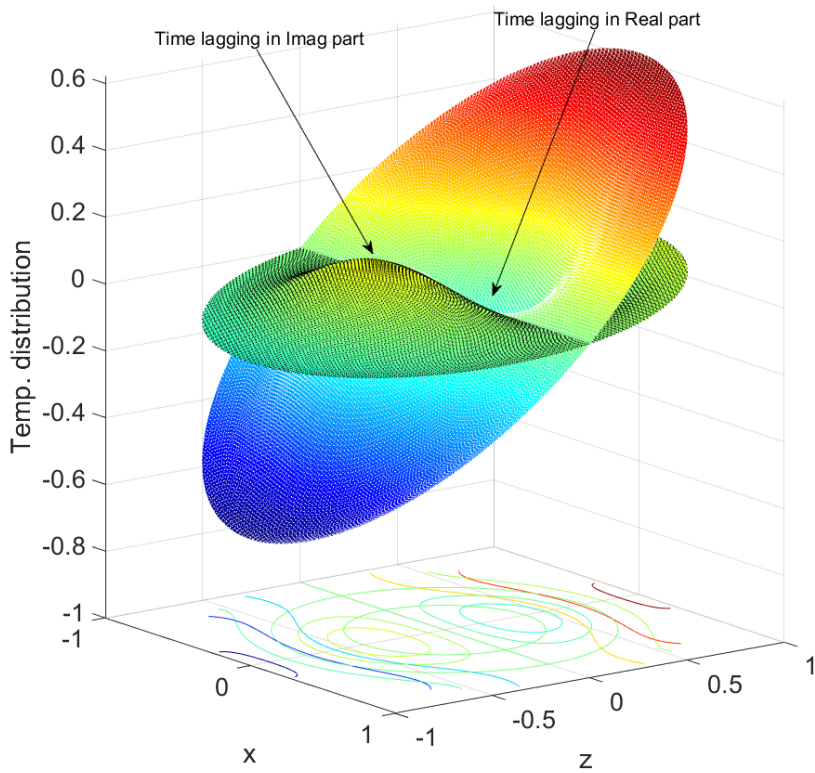


Fig. 2.9 Normalized temperature profiles

Chapter 3 Ring structure

3.1 Constitutive equations

The rotating thin ring structure with constant angular velocity as $\dot{\theta} = \Omega$ with respect to Z -axis is a special case of arches [4] as Fig. 2.1, and the equation of motion can be obtained by reduction from Love's shell equation and Hamilton's Principle. [90] In the ring, the thickness is sufficiently thinner than the mean radius, thus Euler-Bernoulli beam theory can be applied into the ring. [44] Additionally, the virtual density including point masses should be obtained by perturbation method further. In here, the lumped masses only affect kinetic energy nor strain energy, thus ρ can be changed only as ρ_{imp} [36] nor E , I , and A . Firstly, the kinetic and strain energies are given as [90]

$$K = \int_{\theta=0}^{2\pi} \frac{\rho_{\text{imp}} A R_0}{2} [(\dot{u} - v\Omega)^2 + (\dot{v} + (u + R_0)\Omega)^2] d\theta \quad (3.1.1a)$$

$$U = \frac{1}{2} \int_R \int_{\theta} \int_z (\Sigma \sigma \varepsilon) dV \quad (3.1.1b)$$

The variations of both energies can be expressed as

$$\int_{t_0}^{t_1} \delta K dt = \int_{t_0}^{t_1} \int_{\theta=0}^{2\pi} \frac{\rho_{\text{imp}} A R_0}{2} \left[\begin{aligned} &(-\ddot{u} + 2\dot{v}\Omega + u\Omega^2 + R_0\Omega^2)\delta u \\ &+ (-\ddot{v} - 2\dot{u}\Omega + v\Omega^2)\delta v \end{aligned} \right] d\theta dt \quad (3.1.2a)$$

$$\int_{t_0}^{t_1} \delta U dt = \int_{t_0}^{t_1} \int_{\theta=0}^{2\pi} \left[\frac{EI}{R_0^4} \left[\frac{\partial^3 v}{\partial \theta^3} - \frac{\partial^4 u}{\partial \theta^4} \right] - \frac{EA}{R_0^2} \left[\frac{\partial v}{\partial \theta} + u \right] \delta u \right. \\ \left. + \frac{EI}{R_0^4} \left[\frac{\partial^2 v}{\partial \theta^2} - \frac{\partial^3 u}{\partial \theta^3} \right] + \frac{EA}{R_0^2} \left[\frac{\partial^2 v}{\partial \theta^2} + \frac{\partial u}{\partial \theta} \right] \delta v \right] d\theta dt \quad (3.1.2b)$$

Furthermore, the external forces per unit length are composed with damping coefficient c and external forces are

$$q_u = -c \frac{\partial u}{\partial t} + f_u(\theta, t) \quad (3.1.3a)$$

$$q_v = -c \frac{\partial v}{\partial t} + f_v(\theta, t) \quad (3.1.3b)$$

Using the Hamilton's principle into Eq. (3.1.2), the equation of motion for the ring with damping is

$$\frac{EI}{R^4} \left[\frac{\partial^3 v}{\partial \theta^3} - \frac{\partial^4 u}{\partial \theta^4} \right] - \frac{EA}{R^2} \left[\frac{\partial v}{\partial \theta} + u \right] \\ + \rho_{\text{imp}} A (\ddot{u} - 2\dot{v}\Omega - u\Omega^2 - R\Omega^2) + q_u = 0 \quad (3.1.4a)$$

$$\frac{EI}{R^4} \left[\frac{\partial^2 v}{\partial \theta^2} - \frac{\partial^3 u}{\partial \theta^3} \right] + \frac{EA}{R^2} \left[\frac{\partial^2 v}{\partial \theta^2} + \frac{\partial u}{\partial \theta} \right] \\ + \rho_{\text{imp}} A (\ddot{v} + 2\dot{u}\Omega - v\Omega^2) + q_v = 0 \quad (3.1.4b)$$

Moreover, the circumferential strain, forces (q_θ , q_3) and inertia terms can be neglected in the equation, thus the center-line of the ring is always constant, as well knows as inextensional condition by $\frac{\partial v}{\partial \theta} + u = 0$. Then,

$$\begin{aligned} & \frac{EI}{R^4} \left[\frac{\partial^6 u}{\partial \theta^6} + 2 \frac{\partial^4 u}{\partial \theta^4} + \frac{\partial^2 u}{\partial \theta^2} \right] \\ & + \rho_{\text{imp}} A \left[\frac{\partial^4 u}{\partial \theta^2 \partial t^2} - \frac{\partial^2 u}{\partial t^2} + 4\Omega \frac{\partial^2 u}{\partial \theta \partial t} + \Omega^2 \left(u - \frac{\partial^2 u}{\partial \theta^2} \right) \right] = q_u'' + q_v' \end{aligned} \quad (3.1.5)$$

where

$$q_u'' = -c \frac{\partial^4 u}{\partial \theta^2 \partial t^2} + \frac{\partial^2}{\partial \theta^2} [f_u(\theta, t)] \quad (3.1.6a)$$

$$q_v' = -c \frac{\partial v'}{\partial t} + \frac{\partial}{\partial \theta} [f_v(\theta, t)] = c \frac{\partial u}{\partial t} + \frac{\partial}{\partial \theta} [f_v(\theta, t)] \quad (3.1.6b)$$

Then, Eqs. (3.1.5) and (3.1.6) can be re-arranged as

$$\begin{aligned} & \frac{EI}{R_0^4} \left[\frac{\partial^6 u}{\partial \theta^6} + 2 \frac{\partial^4 u}{\partial \theta^4} + \frac{\partial^2 u}{\partial \theta^2} \right] + c \frac{\partial}{\partial t} \left[\frac{\partial^2 u}{\partial \theta^2} - u \right] \\ & + \rho_{\text{imp}} A \left[\frac{\partial^4 u}{\partial \theta^2 \partial t^2} - \frac{\partial^2 u}{\partial t^2} + 4\Omega \frac{\partial^2 u}{\partial \theta \partial t} + \Omega^2 \left(u - \frac{\partial^2 u}{\partial \theta^2} \right) \right] \\ & = \frac{\partial}{\partial \theta} [f_v(\theta, t)] + \frac{\partial^2}{\partial \theta^2} [f_u(\theta, t)] \end{aligned} \quad (3.1.7)$$

The only external circumferential force can be assumed as

$$f_u(\theta, t) = \frac{F_0}{2\pi R_0} \delta(\theta - \theta_f) \exp(j\omega t) \quad (3.1.8)$$

In here, the tangential force is neglected, thus $f_v(\theta, t) = 0$.

Applying Eq. (3.1.7) to Eq. (3.1.6), thus

$$\begin{aligned}
& \frac{EI}{R_0^4} \left[\frac{\partial^6 u}{\partial \theta^6} + 2 \frac{\partial^4 u}{\partial \theta^4} + \frac{\partial^2 u}{\partial \theta^2} \right] + c \frac{\partial}{\partial t} \left[\frac{\partial^2 u}{\partial \theta^2} - u \right] \\
& + \rho_{\text{imp}} A \left[\frac{\partial^4 u}{\partial \theta^2 \partial t^2} - \frac{\partial^2 u}{\partial t^2} + 4\Omega \frac{\partial^2 u}{\partial \theta \partial t} + \Omega^2 \left(u - \frac{\partial^2 u}{\partial \theta^2} \right) \right] \\
& = \frac{F_0}{2\pi R_0} \delta''(\theta - \theta_f) \exp(j\omega t) \tag{3.1.8}
\end{aligned}$$

Moreover, the free vibration can be modeled by eliminating F_0 as

$$\begin{aligned}
& \frac{EI}{R_0^4} \left[\frac{\partial^6 u}{\partial \theta^6} + 2 \frac{\partial^4 u}{\partial \theta^4} + \frac{\partial^2 u}{\partial \theta^2} \right] + c \frac{\partial}{\partial t} \left[\frac{\partial^2 u}{\partial \theta^2} - u \right] \\
& + \rho_{\text{imp}} A \left[\frac{\partial^4 u}{\partial \theta^2 \partial t^2} - \frac{\partial^2 u}{\partial t^2} + 4\Omega \frac{\partial^2 u}{\partial \theta \partial t} + \Omega^2 \left(u - \frac{\partial^2 u}{\partial \theta^2} \right) \right] = 0 \tag{3.1.9}
\end{aligned}$$

3.2 Solutions – eigenfrequencies

In this Section, the solutions of the eigenfrequencies are represented using the method in the previous section. Substituting Eq. (2.1.11) into Eq. (3.1.9), then the eigenvalue of the rotating ring is

$$[\omega_{\text{imp},\Omega}] = \frac{2\Omega n}{n^2+1} \pm \sqrt{\left(\frac{2\Omega n}{n^2+1}\right)^2 - \Omega^2 + (\omega_{\text{imp}})^2} \quad (3.2.1)$$

where the eigenfrequency of the non-rotating ring ω_{imp} is

$$(\omega_{\text{imp}})^2 = \frac{EI}{\rho_{\text{imp}}AR_0^4} \frac{(n^2-1)^2 n^2}{n^2+1} \quad (3.2.2)$$

In order to obtain the eigenfrequency of the imperfect ring, the virtual density ρ_{imp} can be represented using perturbation method. Firstly, the density can be divided into well-known material density (ρ_0) and the density function as [55]

$$\rho_{\text{imp}} = \rho_0 + \delta\rho(\theta) \quad (3.2.3)$$

In here, the variation is performed as a weak form including the virtual density function [55], then ρ_{imp} can be obtained by the integration based on Fourier transform, known as perturbation method. Then the result of the function is

$$(\omega_{\text{imp}})^2 = (\omega_n)^2 \frac{1}{1 + \sum_i \left(\alpha_i \left[1 + \frac{n^2-1}{n^2+1} \cos\{2n(\theta_i - \psi_j)\} \right] \right)} \quad (3.2.4)$$

where $(\omega_n)^2 = \frac{EI}{\rho_0 A R_0^4} \frac{(n^2-1)^2 n^2}{n^2+1}$ and α_i are the square of the eigenfrequency for the uniform ring and the ratio of the point mass with respect to the mass of the perfect ring, respectively. And the results obtained from the Rayleigh-Ritz [45] and perturbation [55] methods are the same analytically when there is no imperfection of the stiffness.

And the shift angle is

$$\psi_j = \frac{1}{2n} \arctan \frac{\sum_i (m_i \sin\{2n\theta_i\})}{\sum_i (m_i \cos\{2n\theta_i\})} + \frac{j\pi}{2n} \quad (3.2.5)$$

where $j = 0$ or 1 is the orientation mode, and the whole process using Rayleigh-Ritz method is stated in [45].

Thus, Eq. (3.2.3) can be re-written with respect to the imperfections as:

$$\rho_{\text{imp}} = \rho_0 + \rho_0 \sum_i \left(\alpha_i \left[1 + \frac{n^2-1}{n^2+1} \cos\{2n(\theta_i - \psi_j)\} \right] \right) \quad (3.2.6)$$

Fig. 3.1 shows the eigenfrequency with respect to the mode numbers for normalized properties except the mode numbers. Thus ω_n consists of only n , and the approximation of the frequency can be set as $\omega_n = n^2$ for

higher mode number. In here, $\omega_n = n^2$ for an ultra-high frequency ring can be reasonable more than $n = 40$ because the difference is less than 0.1%. Additionally, the actual resonator is used in $n=3$ or lower mode. However, the predictions of the data in high modes are shown in this work for various future purposes.

The accuracy of the inextensional assumption of the ring is not ensured in the higher mode generally. The amplitude goes smaller in the higher mode as shown in the transfer function. However, the multiple dimensional heat conduction can compensate the characteristics of the TED in the higher mode with respect to the result of FEM. [39] Thus, the present work as the toroidal ring with 3-D heat conduction equation can be applied in the higher mode, too. And the FEM results can ensure the theoretical data of the inextensional condition in higher number of the modes. [37]

Fig. 3.2 represents the effect of angular rotational velocity with respect to ω_n as the same model in Fig. 3.1. The words “backward” and “forward” are the directions of the wave-traveling during the motion. For the cases as $n = 2$, both lines are the asymptotic curves for other mode numbers. And when n increases, the difference of an eigenfrequency of rotating structure with respect to the non-rotating one goes smaller than lower mode number. Moreover, the frequency goes lower significantly when the rotational velocity is high. In the case, the rotating effect is dominant rather than the eigenfrequency.

Fig. 3.3 shows the percentage difference of the eigenfrequencies of the

same normalized models with attached point mass at 0 [deg] only. The difference goes almost proportional with respect to the mass ratio, and converges when the mode number is high. For the data, the main factor of the difference is mass ratio, and mode number in lower modes.

Figs. 3.4 and 3.5 represent the mode shapes of the model with single attached mass for $n = 2$ and 3, respectively. The orientation angle makes the distortion in the vibrational mode shape with respect to the shape on uniform ring models.

3.3 Transfer function of the forced vibration

For the modal analysis, the mode shape of the vibration can be expressed as the summation of various responses as

$$u(\theta, t) = \sum_{n=2}^{\text{inf}} \Psi_n(\theta) \exp(j\omega t) \quad (3.3.1)$$

Where $\Psi_n(\theta)$ is the mode shape of each n given as

$$\Psi_n(\theta) = U_n \cos(n\theta + n\psi_l) \quad (3.3.2)$$

Substituting Eqs. (2.1.11) and (3.3.2) into Eq. (3.3.1), thus ($\exp(j\omega t)$ omitted in both sides)

$$\begin{aligned} & \sum_{n=2}^{\text{inf}} \left\{ \begin{array}{l} \frac{EI}{R_0^4} (-n^6 + 2n^4 - n^2) - jc\omega(n^2 + 1) \\ + \rho_{\text{imp}} A [(n^2 + 1)\omega^2 - 4n\Omega\omega + \Omega^2(n^2 + 1)] \end{array} \right\} \\ & = \frac{F_0}{2\pi R_0} \delta''(\theta - \theta_f) \end{aligned} \quad (3.3.3)$$

To use the orthogonality of eigenfunction, Eq. (3.3.3) can be integrated after multiplying by $\cos(n\theta + n\psi_j)$ through $\theta = 0$ to 2π similarly as Ref. [80] as

$$\begin{aligned}
& \int_0^{2\pi} \left[\sum_{n=2}^{\text{inf}} \left\{ \frac{EI}{R_0^4} (-n^6 + 2n^4 - n^2) - jc\omega(n^2 + 1) \right. \right. \\
& \quad \left. \left. + \rho_{\text{imp}} A [(n^2 + 1)\omega^2 - 4n\Omega\omega + \Omega^2(n^2 + 1)] \right\} \right] ad\theta \\
& \quad \times \Psi_n(\theta) \cos(n\theta + n\psi_j) \\
&= \int_0^{2\pi} \left[\sum_{n=2}^{\text{inf}} \left\{ \frac{EI}{R_0^4} (-n^6 + 2n^4 - n^2) - jc\omega(n^2 + 1) \right. \right. \\
& \quad \left. \left. + \rho_{\text{imp}} A [(n^2 + 1)\omega^2 - 4n\Omega\omega + \Omega^2(n^2 + 1)] \right\} \right] ad\theta \\
& \quad \times U_n \cos(n\theta + n\psi_j) \cos(n\theta + n\psi_j) \\
&= \int_0^{2\pi} \left[\frac{F_0}{2\pi R_0} \delta''(\theta - \theta_f) \cos(n\theta + n\psi_j) \right] ad\theta \tag{3.3.4}
\end{aligned}$$

The result of integrations in Eq. (3.3.4) can be obtained by the term U_n as

$$U_n = \frac{n^2 F_0 \cos(n\theta_f + n\psi_j)}{\rho_{\text{imp}} A (n^2 + 1) 2R_0 \pi^2 \left[\omega_n^2 - \omega^2 + \frac{jc\omega}{\rho_{\text{imp}} A} - \Omega^2 + 4\frac{n\Omega\omega}{n^2 + 1} \right]} \tag{3.3.5}$$

$$\text{with } \frac{c}{\rho_{\text{imp}} A} \equiv \beta_d \left[\frac{1}{\text{sec}} \right].$$

Eq. (3.3.3) can be re-written by using Eq. (3.3.5), thus the summation of mode shapes is

$$\begin{aligned}
u(\theta, t) &= \\
& \sum_{n=2}^{\text{inf}} \frac{n^2 \cos(n\theta_f + n\psi_j) \cos(n\theta + n\psi_j)}{\rho_{\text{imp}} A (n^2 + 1) \pi \left[\omega_n^2 - \omega^2 + j\omega\beta_d - \Omega^2 + 4\frac{n\Omega\omega}{n^2 + 1} \right]} \frac{F_0}{2\pi R_0} \exp(j\omega t) \tag{3.3.6}
\end{aligned}$$

On the forced vibration, the response with respect to the force is defined as

a transfer function as

$$H(\theta_s, \theta_f, \omega) = \frac{u(\theta, t)}{f} \quad (3.3.7)$$

In here, θ_s is the angular position of the sampling point for the ring model.

For the present ring model, the transfer function can be written as

$$H(\theta_s, \theta_f, \omega) = H = \sum_{n=2}^{\infty} \frac{n^2 \cos(n\theta_f + n\psi_j) \cos(n\theta + n\psi_j)}{\rho_{\text{imp}} A (n^2 + 1) \pi \left[\omega_n^2 - \omega^2 + j\omega \beta_d - \Omega^2 + 4 \frac{n\Omega\omega}{n^2 + 1} \right]} \quad (3.3.8)$$

3.4 Random excitation

The random vibration can be modeled by using the spectral density. In order to simplify the analysis, the ‘‘Gaussian white noise’’ assumption is adopted to idealize the distribution of frequencies due to the input force as constant $S_{ff} = S_0$. The SD of response $S_{yy}(x_1, x_2, \omega)$ for a longitudinal coordinate is defined as [80]

$$S_{yy}(x_1, x_2, \omega) = S_0 \times \int_{s_j=0}^{s_j=L} \text{conj}[H_{\text{longi}}(x_1, s_j, \omega)] ds_j \times \int_{s_k=0}^{s_k=L} H_{\text{longi}}(x_2, s_k, \omega) ds_k \quad (3.4.1)$$

where H_{longi} , x_1 , and s_j are the transfer function of longitudinal coordinate, 1st detection point of the response, and the j^{th} interaction point of force, respectively.

Similarly, the SD can be modified with respect to the angular coordinate as

$$S_{uu}(\theta_{s1}, \theta_{s2}, \omega) = H(\theta_{s1}, \theta_{f1}, -\omega) \times S_0 \times H(\theta_{s2}, \theta_{f2}, \omega) \quad (3.4.2)$$

in here, the transfer functions are different from Eq. (3.4.1) because the integral of the ring is already operated in Section 3.3, thus the dimensions are different, too. And the both functions have relationship as a complex conjugate (i.e. $\text{conj}[H(\theta_s, \theta_f, \omega)] = H(\theta_s, \theta_f, -\omega)$).

Substituting Eq. (3.3.8) into Eq. (3.4.2), thus

$$\begin{aligned}
S_{uu}(\theta_{s1}, \theta_{s2}, \omega) &= H(\theta_{s1}, \theta_{f1}, -\omega) \times S_0 \times H(\theta_{s2}, \theta_{f2}, \omega) = S_0 \times \\
&\sum_{n_1=2}^{\text{inf}} \sum_{n_2=2}^{\text{inf}} \frac{\left\{ \begin{array}{c} n_1^2 \cos(n_1 \theta_{f1} + n_1 \psi_{j,n_1}) \times \\ \cos(n_1 \theta_{s1} + n_1 \psi_{j,n_1}) \end{array} \right\}}{\left\{ \begin{array}{c} \rho_{\text{imp},n_1} A(n_1^2+1) \pi \times \\ \left[\omega_{n_1}^2 - \omega^2 + j\omega\beta_d - \Omega^2 + 4\frac{n_1\Omega\omega}{n_1^2+1} \right] \end{array} \right\}} \frac{\left\{ \begin{array}{c} n_2^2 \cos(n_2 \theta_{f2} + n_2 \psi_{j,n_2}) \times \\ \cos(n_2 \theta_{s2} + n_2 \psi_{j,n_2}) \end{array} \right\}}{\left\{ \begin{array}{c} \rho_{\text{imp},n_2} A(n_2^2+1) \pi \times \\ \left[\omega_{n_2}^2 - \omega^2 + j\omega\beta_d - \Omega^2 + 4\frac{n_2\Omega\omega}{n_2^2+1} \right] \end{array} \right\}}
\end{aligned} \tag{3.4.3}$$

Where the variables with subscript $n1$ or n_1 are the value with respect to $n = n_1$, and the similar calculation can be applied as $n = n_2$.

When the damping is sufficiently small, and the difference of both adjacent eigenfrequencies are sufficiently large [80], Eq. (3.3.8) can be simplified by applying an approximation as $n_1 = n_2 = n$. Then, the modal cross-SD terms can be neglected, thus

$$\begin{aligned}
[S_{uu}(\theta_{s1}, \theta_{s2}, \omega)]_{\text{approx}} &\cong S_0 \times \\
&\sum_{n=2}^{\text{inf}} \left[\frac{n^2 \cos(n\theta_f + n\psi_j)}{\rho_{\text{imp}} A(n^2+1) \pi} \right]^2 \left[\frac{\cos(n\theta_{s1} + n\psi_j) \cos(n\theta_{s2} + n\psi_j)}{\left(\omega_n^2 - \omega^2 - \Omega^2 + 4\frac{n\Omega\omega}{n^2+1} \right)^2 + (\omega\beta_d)^2} \right]
\end{aligned} \tag{3.4.4}$$

in here, the cross-spectral components as the off-diagonal terms are neglected in the approximate SD, thus the truncation error between both SDs are important in this work.

Then, the modal truncation based on the direct-SD as $\theta_{s1} = \theta_{s2} = \theta_s$ is applied, but the modal cross spectral terms still valid because $n_1 \neq n_2$, thus

$$S_{uu}(\theta_s, \omega) = H(\theta_s, \theta_f, -\omega) \times S_0 \times H(\theta_s, \theta_f, \omega) = S_0 \times$$

$$\sum_{n_1=2}^{\infty} \sum_{n_2=2}^{\infty} \frac{\left\{ \begin{array}{c} n_1^2 \cos(n_1 \theta_f + n_1 \psi_{j,n_1}) \times \\ \cos(n_1 \theta_s + n_1 \psi_{j,n_1}) \end{array} \right\}}{\left\{ \begin{array}{c} \rho_{\text{imp},n_1} A(n_1^2+1) \pi \times \\ \left[\omega_{n_1}^2 - \omega^2 + j\omega\beta_d - \Omega^2 + 4\frac{n_1 \Omega \omega}{n_1^2+1} \right] \end{array} \right\}} \frac{\left\{ \begin{array}{c} n_2^2 \cos(n_2 \theta_f + n_2 \psi_{j,n_2}) \times \\ \cos(n_2 \theta_s + n_2 \psi_{j,n_2}) \end{array} \right\}}{\left\{ \begin{array}{c} \rho_{\text{imp},n_2} A(n_2^2+1) \pi \times \\ \left[\omega_{n_2}^2 - \omega^2 + j\omega\beta_d - \Omega^2 + 4\frac{n_2 \Omega \omega}{n_2^2+1} \right] \end{array} \right\}} \quad (3.4.5)$$

$$[S_{uu}(\theta_s, \omega)]_{\text{approx}} \cong S_0 \times$$

$$\sum_{n=2}^{\infty} \left[\frac{n^2 \cos(n\theta_f + n\psi_j) \cos(n\theta_s + n\psi_j)}{\rho_{\text{imp}} A(n^2+1) \pi} \right]^2 \left[\frac{1}{\left(\omega_n^2 - \omega^2 - \Omega^2 + 4\frac{n\Omega\omega}{n^2+1} \right)^2 + (\omega\beta_d)^2} \right] \quad (3.4.6)$$

To analyze the motion of the ring model, statistical data are needed from the SD. The average of u^2 can be obtained by integrating the SD through the frequencies as [80]

$$E[u^2(\theta, t)] = \int_{-\infty}^{\infty} S_{uu}(\theta_s, \omega) d\omega \quad (3.4.7)$$

In here, the frequency band is limited between $\omega_1 \leq |\omega| \leq \omega_2$, thus

$$S_{ff}(\omega) = S_0 \quad (3.4.8)$$

otherwise, $S_{ff}(\omega) = 0$.

Substituting Eqs. (3.4.5) and (3.4.6) into Eq. (3.4.7) with the band-limitation, thus

$$E[u^2(\theta, t)]_{\text{exact}} = 2S_0 \times \int_{\omega_1}^{\omega_2} \text{Real}\left\{\sum_{n_1=2}^{\text{inf}} \sum_{n_2=2}^{\text{inf}} [(HH)_{\text{exact}}]\right\} d\omega \quad (3.4.9)$$

where

$$(HH)_{\text{exact}} = \left[\frac{\left\{ \frac{n_1^2 \cos(n_1\theta_{f_1} + n_1\psi_{j,n_1}) \times}{\cos(n_1\theta + n_1\psi_{j,n_1})} \right\}}{\left\{ \frac{\rho_{\text{imp},n_1} A(n_1^2 + 1) \pi \times}{\left[\omega_{n_1}^2 - \omega^2 + j\omega\beta_d - \Omega^2 + 4\frac{n_1\Omega\omega}{n_1^2 + 1} \right]} \right\}} \frac{\left\{ \frac{n_2^2 \cos(n_2\theta_{f_2} + n_2\psi_{j,n_2}) \times}{\cos(n_2\theta + n_2\psi_{j,n_2})} \right\}}{\left\{ \frac{\rho_{\text{imp},n_2} A(n_2^2 + 1) \pi \times}{\left[\omega_{n_2}^2 - \omega^2 + j\omega\beta_d - \Omega^2 + 4\frac{n_2\Omega\omega}{n_2^2 + 1} \right]} \right\}} \right] \quad (3.4.10)$$

Moreover, the simplified form by neglecting the modal cross-SD in the expression is:

$$E[u^2(\theta, t)]_{\text{approx}} = 2S_0 \int_{\omega_1}^{\omega_2} \left\{ \sum_{n=2}^{\text{inf}} \left(\frac{\left[\frac{n^2 \cos(n\theta_s + n\psi_j) \cos(n\theta_f + n\psi_j)}{\rho_{\text{imp}} A(n^2 + 1) \pi} \right]^2}{\left[\frac{1}{\left(\omega_n^2 - \omega^2 - \Omega^2 + 4\frac{n\Omega\omega}{n^2 + 1} \right)^2 + (\omega\beta_d)^2} \right]} \right) \right\} d\omega \quad (3.4.11)$$

To obtain the maximum deflection, experiential equations are mainly applied as in Ref. [80]. The SD for the velocity and acceleration of the deflection are given as

$$S_{\dot{u}\dot{u}}(x, \omega) = \omega^2 S_{uu}(x, \omega), \quad S_{\ddot{u}\ddot{u}}(x, \omega) = \omega^4 S_{uu}(x, \omega) \quad (3.4.12a,b)$$

Moreover, the maximum deflection obtained from the statistical experiences can be expressed as

$$\frac{E[u_{\max}(\theta)]}{\sigma_u} \equiv (CF) \quad (3.4.13)$$

In here, (CF) is Crest factor or the peak factor with Euler–Mascheroni constant ($\gamma \approx 0.577216$) defined as [79]

$$(CF) = \sqrt{2 \ln(N_{\text{mean}})} + \frac{\gamma}{\sqrt{2 \ln(N_{\text{mean}})}} + (\text{higher order terms}) \quad (3.4.14)$$

Furthermore, the numbers of mean values with respect to the zero-crossing-frequency, and maxima with respect to the peak-frequency, respectively, are:

$$N_{\text{mean}} = N_{\text{max}} \sqrt{1 - \varepsilon_b^2}, \quad N_{\text{max}} = \left(\frac{1}{2\pi} \frac{\sigma_{\dot{u}}}{\sigma_u} T \right) \quad (3.4.15,16)$$

The Vanmarcke's bandwidth parameter for the response known with 0 (i.e. extremely narrowband) to 1 (i.e. extremely broadband) is

$$\varepsilon_b = \sqrt{1 - \frac{m_{sm,2}^2}{m_{sm,0} m_{sm,4}}} \quad (3.4.17)$$

where the \hat{i} -th ($i=0,2,4$) spectral moments are given as:

$$m_{sm,i} = \int \omega^i S_{uu}(\omega) d\omega \quad (3.4.18)$$

The PF and parameter can be used as independent variables to estimate the fatigue life, but the specific experimental equations are omitted in this work. The modal coupling effect is due to the square term in the definition of the spectral density. In here, the various modes of the response can be multiplied, thus the off-diagonal terms (i.e. different modes) affect the characteristics of the exact-SD, such as antiresonance. To simplify the model, only diagonal terms can be multiplied as the approximated-SD, but the antiresonance cannot be detected as the limitation. In this work, the sampling point is just one as the direct-SD to simplify the cross-SD, but the multiple modes of the response are still valid to get the antiresonance.

Fig. 3.6(a) shows the spectral densities (SD) of the normalized ring and beam models. The SD of the non-vibrational (i.e. $\omega = 0$) structures are set as 1, and the exact (solid lines) and approximated (dotted lines) densities are presented in the graphs. For the exact SDs, the antiresonances appear in the Figure as the local minimum points. On the contrary, the antiresonance diminished in the approximated SDs as Eq. (3.4.6), due to the neglect of the off-diagonal terms in Eq. (3.4.5). Moreover, the larger damping coefficients makes the difference of the amplitude on SDs lower, but the eigenfrequency as resonance point is almost the same. And Fig. 3.6(b) indicates the magnitude plot for $\omega=0$ to 20.

And Fig. 3.7 represents the phase angles of the same models. The eigenfrequencies and antiresonance points are located as the angle is $\pm 0.5\pi$ for getting larger and smaller, respectively. This paragraph can show the characteristics of the SD more clearly, thus the antiresonance and transient area can be depicted more easily.

Fig. 3.8 shows the normalized standard deviations (StDevs) of the response for displacement based on exact- and approximated SDs for the ring and beam models. The differences for the ring are more significant nearby the impact point, but can be neglected in other points. As similarly with the beam model, the antiresonance is important issue in the ring model.

Fig. 3.9 represents the StDevs with respect to the range of input frequencies. Exactly, the wide range input makes the displacement larger, and the error goes smaller than the case based on the narrow range input force.

Fig. 3.10 shows the peak factors for the ring and beam models. The factor can be used to estimate the maximum displacement with respect to the StDevs. As stated in previous Figures, the damping coefficient is less important in the factor. On the contrary, the input frequency and the approximation are significant factors in the analysis. Thus, Fig. 3.11 represents the expectation value of the deflection obtained from Eq. (3.4.9). The trends are almost similar to the Fig. 3.9 (a) because the deviation of the PF is much smaller than the StDevs.

3.5 Frequency trimming method

In Section 3.2, the frequency deviation is investigated with imperfection by using Raileigh-Ritz method. Based on the orientation angle ψ_j , the kinetic energy term (i.e. ρ_{imp}) includes two values. And then, the splitted eigenfrequencies and the mode shapes are bifurcated, thus the inaccuracy occurs in the structure. To compensate the error, the extra positive mass or hole (i.e. negative mass) can be added, and thus the bifurcated frequencies into single value. [82][83]

From Eq. (3.2.5) with modified orientation angle $\psi_{j,\text{trm}}$ and correction of mass, the bifurcated frequencies are

$$(\omega_{\text{trm},1})^2 = (\omega_n)^2 \frac{1}{(1+\alpha_i) - \frac{(1-n^2)}{(1+n^2)} \sum_i (\alpha_i [\cos\{2n(\theta_i - \psi_j)\}])} \quad (3.5.1a)$$

$$(\omega_{\text{trm},2})^2 = (\omega_n)^2 \frac{1}{(1+\alpha_i) + \frac{(1-n^2)}{(1+n^2)} \sum_i (\alpha_i [\cos\{2n(\theta_i - \psi_j)\}])} \quad (3.5.1b)$$

Eliminating ω_n in both equations, then

$$\sum_i (\alpha_i [\cos\{2n(\theta_i - \psi_j)\}]) = \lambda_{\text{trm}} \quad (3.5.2)$$

$$\text{where } \lambda_{\text{trm}} = \left(\frac{1+n^2}{1-n^2} \right) (1 + \alpha_i) \frac{(\omega_{\text{trm},1})^2 - (\omega_{\text{trm},2})^2}{(\omega_{\text{trm},1})^2 + (\omega_{\text{trm},2})^2}.$$

In the special case for single trimming mass, $[\cos\{2n(\theta_i - \psi_j)\}] = 1$, thus

$$m_{\text{trm}} = \mp M_p (1 + \alpha_i) \lambda_{\text{trm}} \quad (3.5.3)$$

with the negative and positive signs for orientation angles as ψ_0 and ψ_1 , respectively.

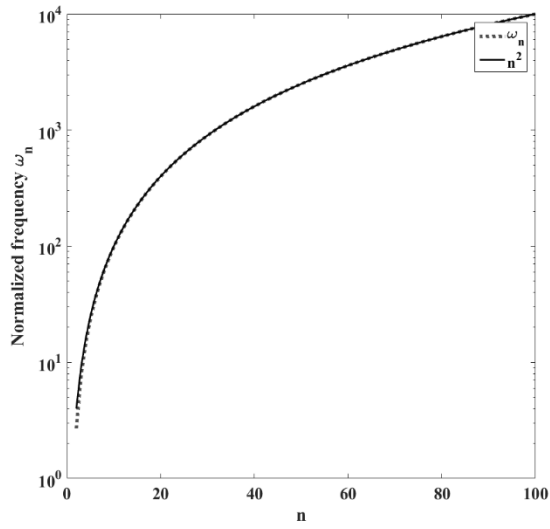
To eliminate the frequency split, there are two ways to modify the frequencies. Firstly, the negative sign is removing mass from the imperfect ring. On the contrary, the positive sign means adding point mass into the structure. Thus, the prediction of the trimming methodology can be applied to modify the irregularity of the sensor or resonator. Moreover, the frequency trimming of the hemispherical shell [86] can be modeled by the similar way.

Table 3.1 represents the data of the trimming method with the same mass ratios and angles in Ref. [45], but the radii are given as $R_0 = 10[\mu\text{m}]$ and $r_0 = 1[\mu\text{m}]$, and the temperature is 80[K]. The trimming masses and the orientation angles are the same as [45], and the percentage errors are the same, too. Thus, the trimming method can be applied into any scale of the ring. However, the trimmed frequencies are not exactly the same because of the numerical error during the calculation.

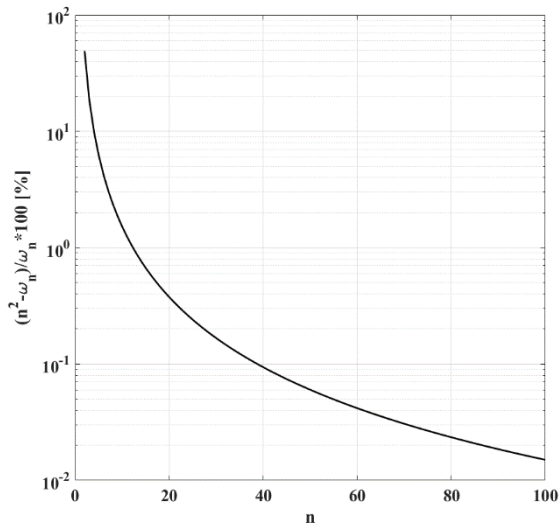
Based on the model in Table 3.1, Fig. 3.12 shows the normalized frequencies of the rotating ring with imperfection and trimming. And Fig. 3.13 represents the Q^{-1} of the same models. And the trimmed values are not the same exactly, but the graphs are much similar for each ψ . Moreover, the rotation can control the difference of the frequency and Q^{-1} .

Table 3.1 The additional mass and frequencies after the trimming

	Initial	Trimmed with ψ_1	Trimmed with ψ_2
ω_n (e+8)	1.1433	1.1433	1.1433
Masses at 45 [deg]	0,20,70	-6.949	38.051
% Point masses according to the perfect ring	1.35, 2.7, 4.05	-2.522	2.522
ω of H-mode (e+8)	1.1074	1.1136	1.1118
ω of L-mode (e+8)	1.0920	1.0879	1.0862
Error %(H) according to the perfect ring	-3.139	-2.597	-2.758
Error %(L) according to the perfect ring	-4.4857	-4.8471	-4.9972



(a)



(b)

Fig. 3.1 Eigenfrequency with respect to the mode numbers

(a) $\omega_n^2 = \frac{n^2(n^2-1)^2}{n^2+1}$, (b) % difference from an eigenvalue of a beam

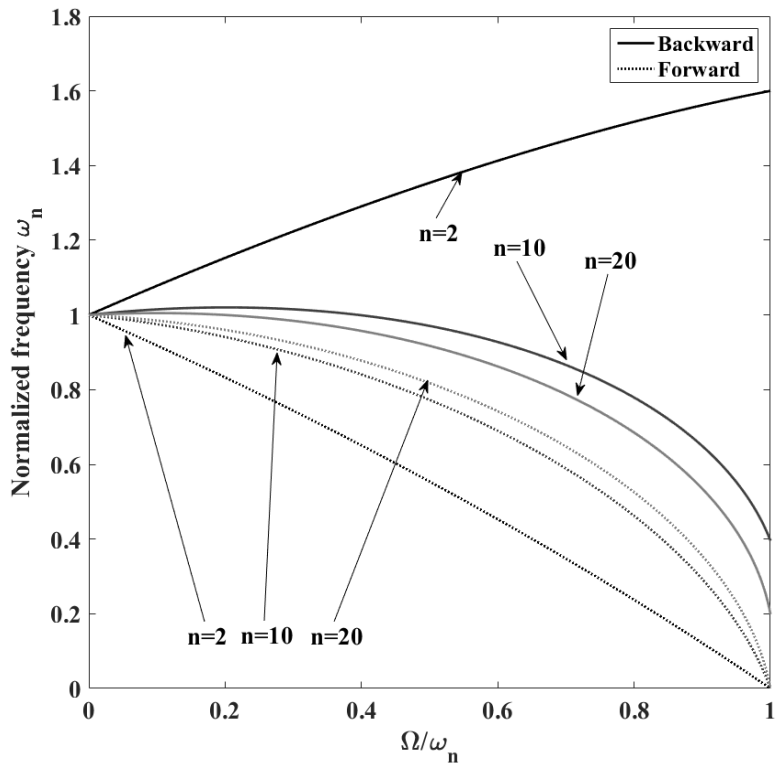


Fig. 3.2 Eigenfrequency with respect to the angular rotational velocity

(Eq. (3.2.2))

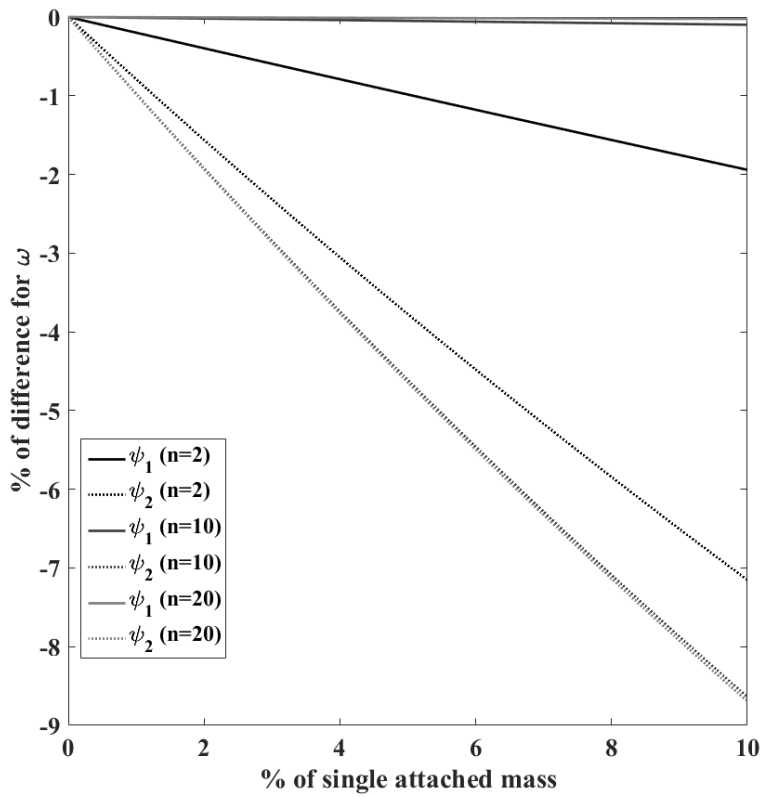
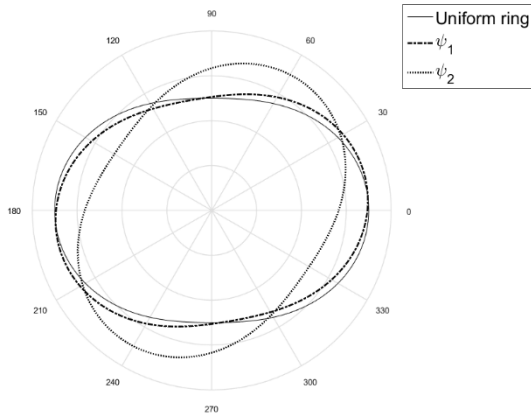
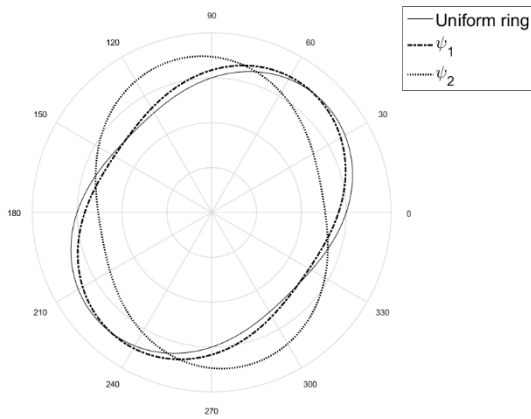


Fig. 3.3 Eigenfrequency with respect to the imperfection (n=2) (Eq.

(3.2.4))



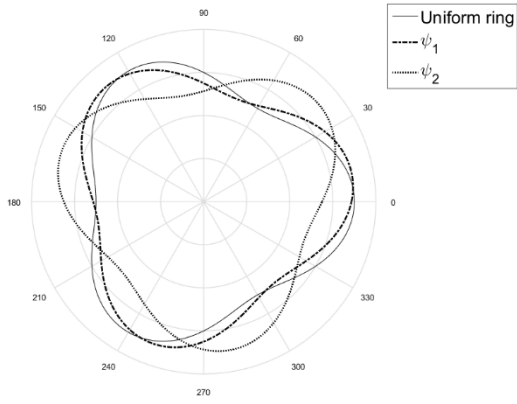
(a)



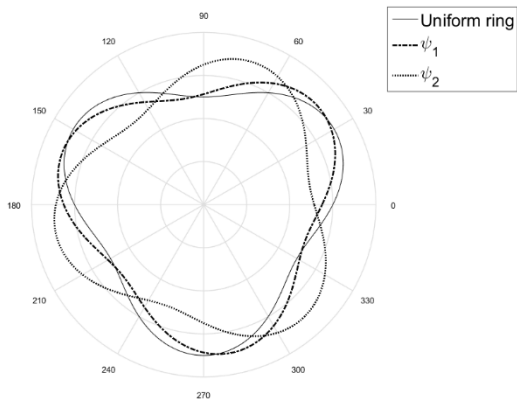
(b)

Fig. 3.4 Vibrational mode shape considered the orientation angle (Eq.

(2.1.11)) with $n = 2$ (a) H-mode (b) L-mode



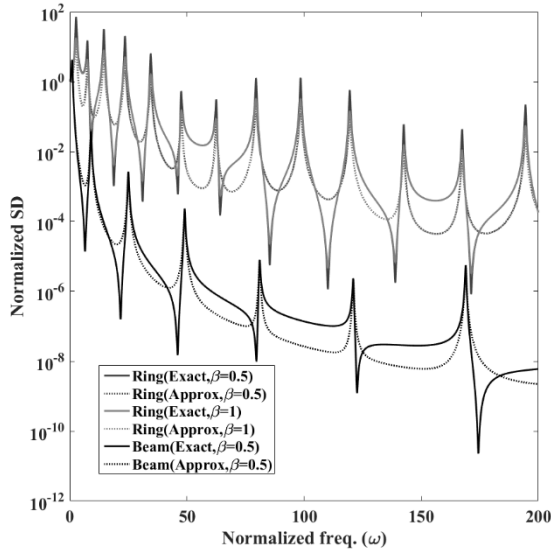
(a)



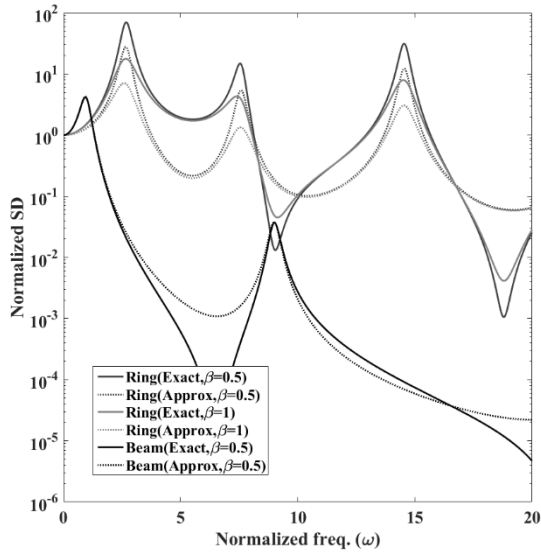
(b)

Fig. 3.5 Vibrational mode shape considered the orientation angle with

$n = 3$ (a) H-mode (b) L-mode



(a)



(b)

Fig. 3.6 Normalized SD for ring and beam models

(a) $\omega=0\sim 200$, (b) magnified plot of $\omega=0\sim 20$

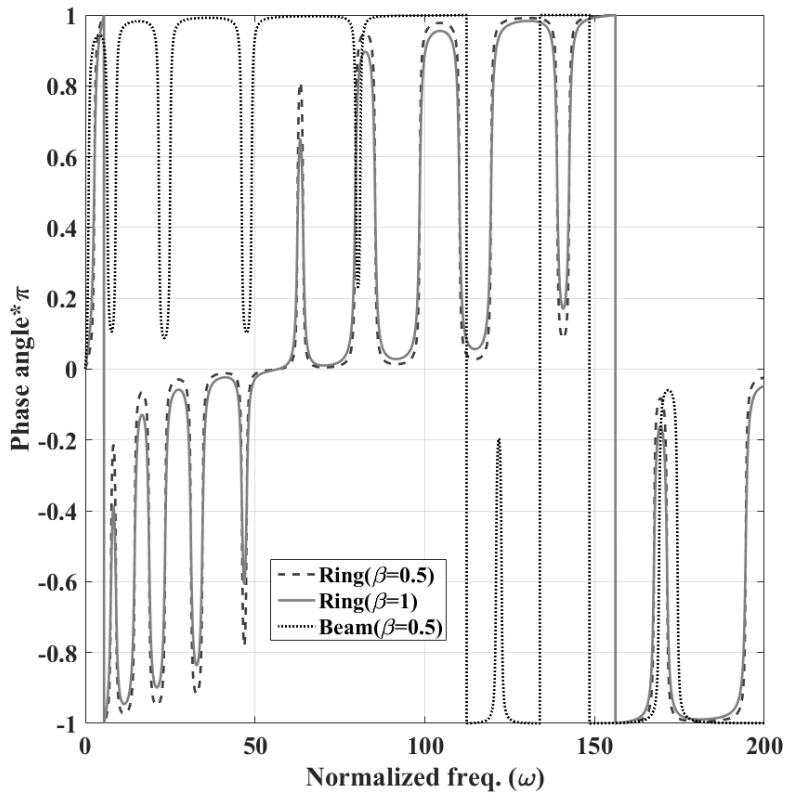
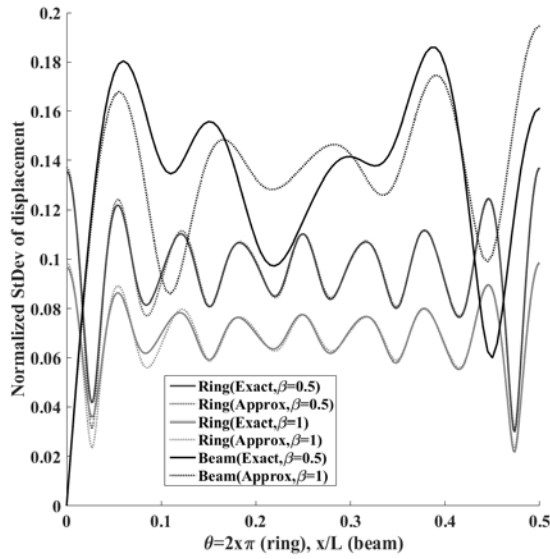
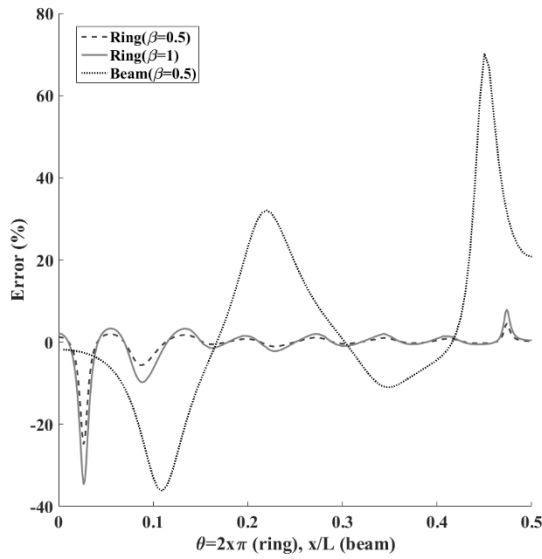


Fig. 3.7 Phase angles of the models

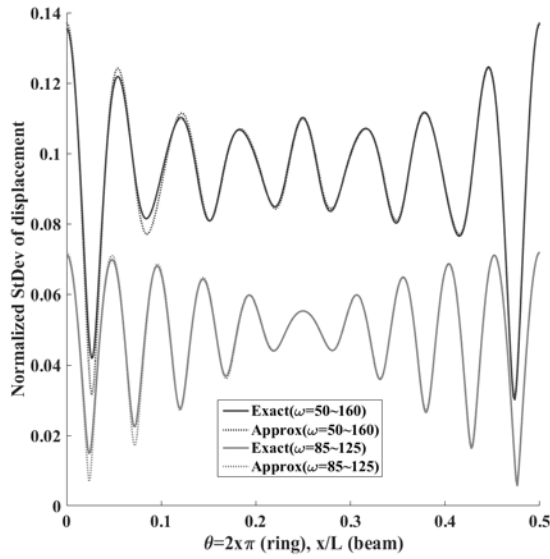


(a)

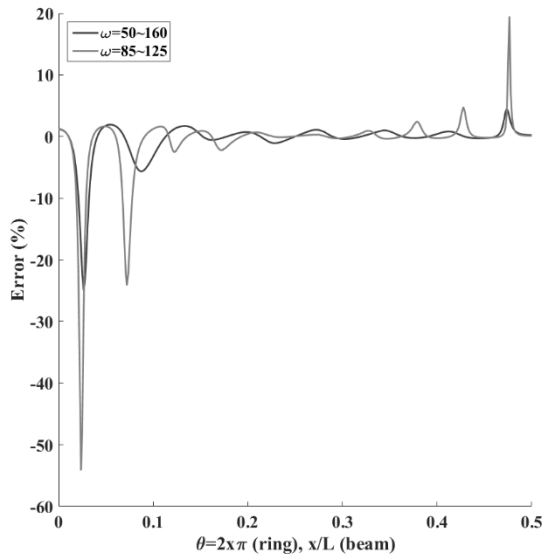


(b)

Fig. 3.8 (a) Normalized StDev of the response for displacement based on exact- and approximated SDs, (b) % errors between both SDs.



(a)



(b)

Fig. 3.9 (a) Normalized StDev of the response for displacement with respect to the input frequencies, (b) % errors between both SDs.

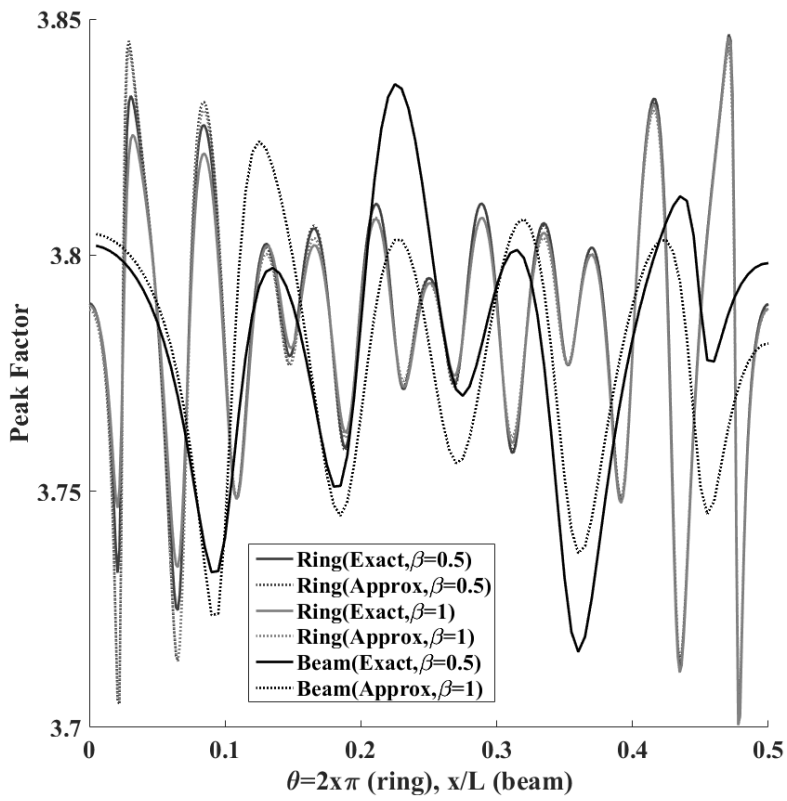


Fig. 3.10 Peak factors

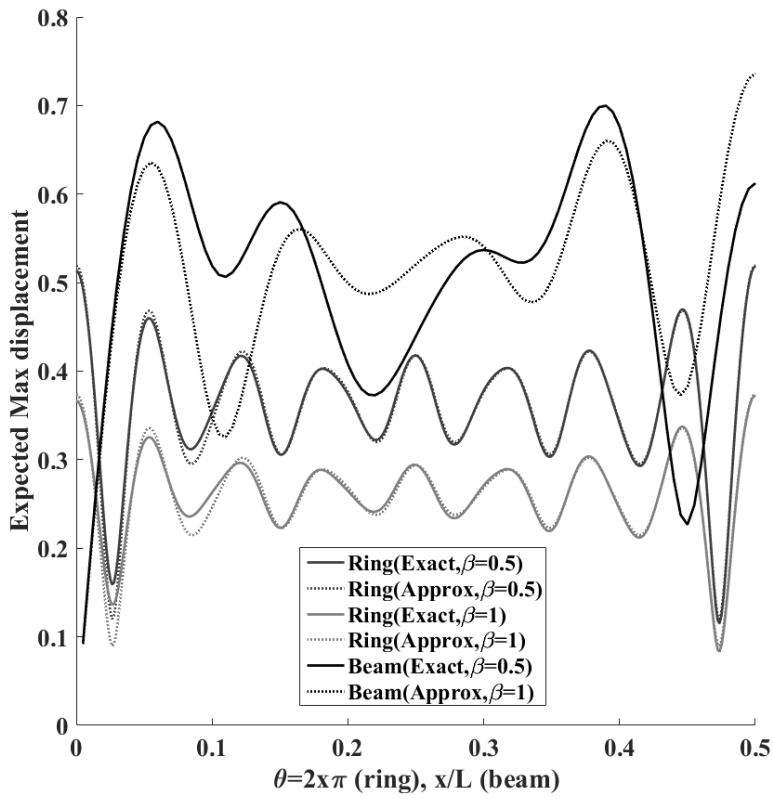


Fig. 3.11 Expectation value of the deflection (Eq. (3.4.9))

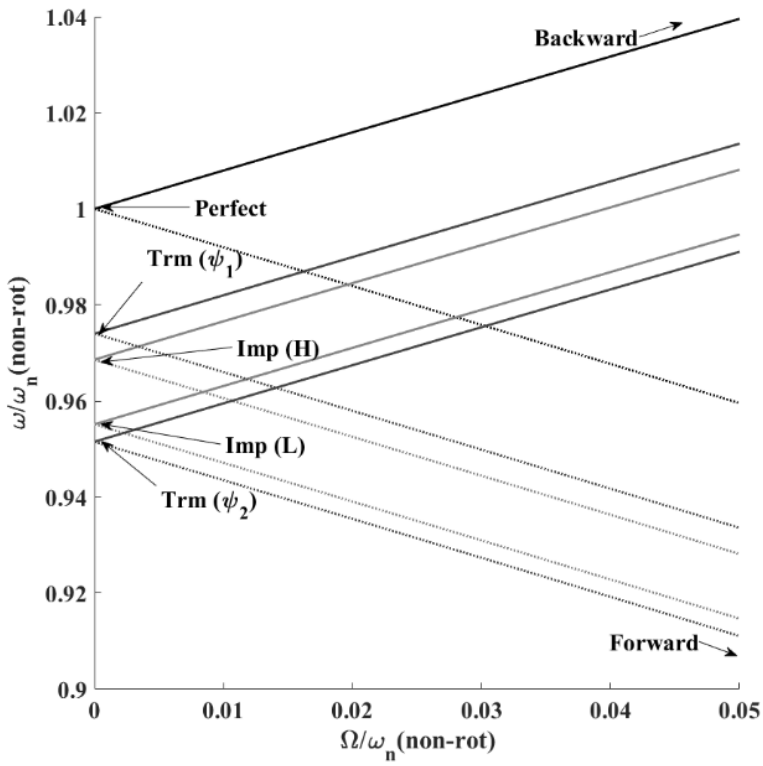


Fig. 3.12 Difference of eigenfrequencies after attaching trimming masses
for the rotating ring

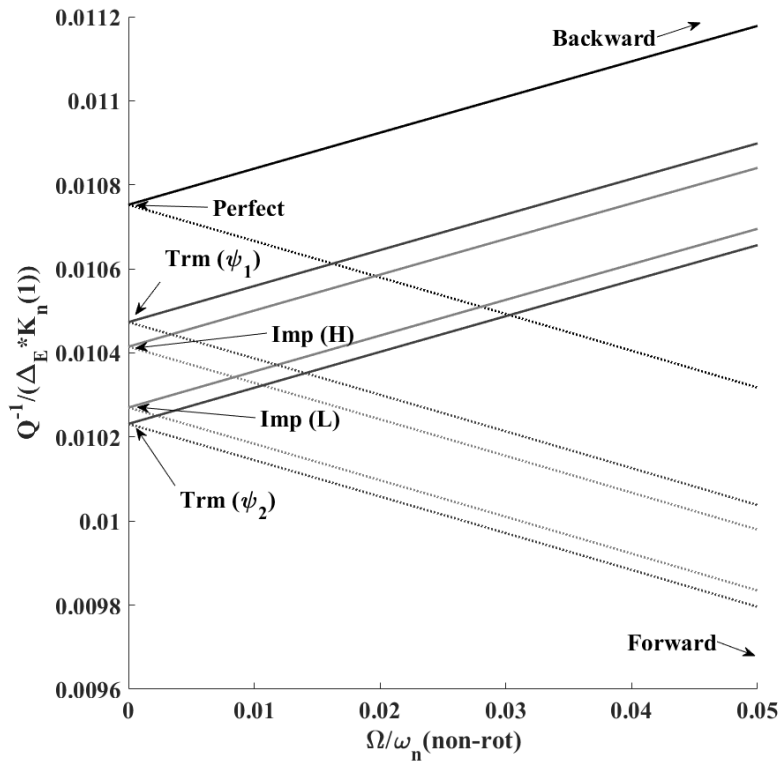


Fig. 3.13 Q^{-1} for the ring model after attaching trimming masses for the rotating ring

Chapter 4 Numerical analysis

4.1 Rectangular cross-sectional ring

The result of the rectangular ring is already analyzed as [44], [40], and so on. In this section, thermoelastic damping for the rectangular ring is simply introduced by the results from literatures.

The motion for in-plane vibration of a rectangular-cross-sectional beam and ring show linear distribution during the vibration. Thus, the complex eigenfrequencies for beam [9] and ring [44] models can be written using the modified Young's modulus as

$$\begin{aligned}(\omega_{\text{beam}})^2 &= \frac{EI}{\rho A} \lambda_n^4 \{1 + \Delta_E [1 + f(\omega)]\} = \frac{E_\omega I}{\rho A} \lambda_n^4 \\ &= (\omega_{\text{iso,beam}})^2 \{1 + \Delta_E [1 + f(\omega)]\}\end{aligned}\quad (4.1.1a)$$

$$\begin{aligned}(\omega_{\text{ring}})^2 &= \frac{EI}{\rho A R_0^4} \frac{n^2(n^2-1)^2}{n^2+1} \{1 + \Delta_E [1 + f(\omega)]\} = \frac{E_\omega I}{\rho A R_0^4} \frac{n^2(n^2-1)^2}{n^2+1} \\ &= (\omega_{\text{iso,ring}})^2 \{1 + \Delta_E [1 + f(\omega)]\}\end{aligned}\quad (4.1.1b)$$

where the subscript “iso” indicates the isothermal frequency obtained by neglecting the TED.

Overall, E_ω is the modified Young's modulus in each model which is the function of the eigenfrequency. In here, λ_n is the normalized eigenvalues of a beam model. For example, $\lambda_n = \frac{n\pi}{L}$ and $\lambda_1 = \frac{4.73}{L}$ are the value of a simply-supported and clamped-clamped beams with length as L ,

respectively.

To simplify the implicit function, Δ_E can be assumed as sufficiently small, thus $f(\omega) \cong f(\omega_{\text{iso}})$ and Taylor's Series can be applied in the equation, then

$$\omega = \omega_{\text{iso}} \left\{ 1 + \frac{\Delta_E}{2} [1 + f(\omega_0)] \right\} \quad (4.1.2)$$

where

$$f(\omega) = \frac{24}{(h\bar{k})^3} \left[\frac{h\bar{k}}{2} - \tan\left(\frac{h\bar{k}}{2}\right) \right] \quad (4.1.3)$$

and

$$\bar{k} = (1 + j) \sqrt{\frac{\omega_{\text{iso}}}{2\chi}} \quad (4.1.4)$$

And the complex number can be separated into the Real and Imaginary parts as:

$$\text{Real}(\omega) = \omega_{\text{iso}} \left[1 + \frac{\Delta_E}{2} \left\{ 1 - \frac{6}{\xi^3} \frac{\sinh(\xi) - \sin(\xi)}{\cosh(\xi) + \cos(\xi)} \right\} \right] \quad (4.1.5a)$$

$$\text{Imag}(\omega) = \omega_{\text{iso}} \left[\frac{\Delta_E}{2} \left\{ \frac{6}{\xi^3} \frac{\sinh(\xi) + \sin(\xi)}{\cosh(\xi) + \cos(\xi)} - \frac{6}{\xi^2} \right\} \right] \quad (4.1.5b)$$

with a coefficient as

$$\xi = h \sqrt{\frac{\omega_{\text{iso}}}{2\chi}} \quad (4.1.6)$$

By the definition of the Q-factor, Eq. (4.1.5) can be rearranged as

$$Q^{-1}(\xi) = \Delta_E \left\{ \frac{6}{\xi^2} - \frac{6}{\xi^3} \frac{\sinh(\xi) + \sin(\xi)}{\cosh(\xi) + \cos(\xi)} \right\} \quad (4.1.7)$$

This is the simple form of Q^{-1} for the rectangular beam model.

When imperfections and rotation are added in the ring, the virtual density as Eq. (2.2.4) can be applied into the eigenfrequency. Thus, Eq. (4.1.5) can be modified based on Eq. (2.2.2) as:

$$\xi_{\text{imp}} = h \sqrt{\frac{[\omega_{\text{imp}}]}{2\chi}} \quad (4.1.8)$$

Then, Q^{-1} is modified as the function of $[\xi_{\text{imp}}]$ [40] as:

$$Q^{-1}(\xi_{\text{imp}}) = \Delta_E \left\{ \frac{6}{(\xi_{\text{imp}})^2} - \frac{6}{(\xi_{\text{imp}})^3} \frac{\sinh(\xi_{\text{imp}}) + \sin(\xi_{\text{imp}})}{\cosh(\xi_{\text{imp}}) + \cos(\xi_{\text{imp}})} \right\} \quad (4.1.9)$$

Table 4.1 shows the experimental data [23] are stated as the Q-factor. In the

literature, the gas damping is controlled by the air pressure as 0.001[Torr] (i.e. 0.133 [Pa]). Moreover, the number of the legs is almost independent, and the other dissipation mechanisms (e.g. air, anchor) are assumed as the same. And the factors of the differences are the uncertainty of the material properties, and of the surface treatment effects which can affect local surface stresses. Thus, the difference can be considered as the Q-factor only due to the TED.

4.2 Circular cross-sectional ring

As stated in the previous Section, the temperature distribution is linear in the rectangular cross-sectional beam or ring. However, the circular cross-sectional beam or ring does not show the linear deformation during the motion due to the irregular shape, thus Eq. (4.1.1) is not valid for the cross-sectional beam or toroidal ring. Using Section 2.2 to 2.3, the quality factor can be obtained as Eq. (2.3.5), thus the form is similar to the Zener's form. Similarly, the Q^{-1} of the imperfect ring with the eigenfrequency with Eq. (3.2.2) as:

$$\frac{1}{Q_{\text{TED,imp}}} = \sum_{q=1}^{\text{inf}} \left[b_{1q} \Delta_E \frac{\{1+g^2\}[\omega_{\text{imp}}]\tau_q}{\{1+g^2-\tau_{\text{cv}}([\omega_{\text{imp}}]^2 \tau_q)\}^2 + ([\omega_{\text{imp}}]\tau_q)^2} \right] \quad (4.2.1)$$

Fig. 4.1 shows the quality factors of the silicon toroidal ring models in $n=2$ and 3. The result is performed by Eq. (4.2.1) with respect to the eigenfrequencies, then the peaks appear according to each line. Moreover, the regions can be classified as the peaks, then the optimization can be established as in Chapter 5. Moreover, the peak moves toward the thinner and larger region when the mode number is larger.

Fig. 4.2 represents the deviation of Q^{-1} with respect to the imperfections using an expression in the graph as $\frac{Q(\xi_{\text{imp}})-Q(\xi)}{Q(\xi)} \times 100[\%]$ with (a) for $n = 2$ and (b) for $n = 3$, respectively. The trends show reversely from the lines in the Figures, thus the concept will be represented in the next Chapter.

And the asymmetric mode performs the smaller deviation because the single point mass acts as the pivot point, thus the characteristics of the vibration is similar to the uniform ring.

Fig. 4.3 shows the percentage difference of the Q with respect to the imperfection and mode numbers. As known from Eq. (3.2.4), the main factors of the difference are the mass ratio, mode number, and angular position. Furthermore, when n goes larger, the difference converges specific value when the single point mass attached on the structure.

Fig. 4.4 shows (a) Q^{-1} , (b) % difference of Q^{-1} for the toroidal ring with $r_0 = 1[\mu\text{m}]$ and $R_0 = 100[\mu\text{m}]$ for $T = 298[\text{K}]$, respectively. And the material properties [31] are shown in Table 4.2. When the mode number is sufficiently high, the NF effect appears clearly in spite of the high temperature as (a). Moreover, the trend of % difference goes reversely with respect to the peak of Q^{-1} as (b). And the differences of $\Sigma(Q^{-1})$ are a little smaller than the simplified data of $q = 1$ because of the NF effect on higher order terms.

Fig. 4.5 shows the Q^{-1} for only $q = 1$ on 80 [K] with respect to the rotational speed on (a) $n = 2$, (b) $n = 10$, (c) magnified plot of (b), respectively. For the higher mode number as (b), Q^{-1} goes down rapidly with higher Ω because the Coriolis effect is significantly large. In addition, the effect of NF makes shift from Q^{-1} of $q = 1$ only, thus the time lagging should be considered when the frequency is ultra-high. And Fig. 4.6 shows the eigenfrequency with respect to Ω for (a) $n = 2$, (b) $n =$

10, respectively. The overall trends are similar to the Fig. 4.5, as shown as the rectangular-cross-sectional Rings [40].

Table. 4.1 Experimental data of the rectangular-cross-sectional ring [23]

a_r	3	3	2	2	2
h	120	117	50	52	38
No. of legs	8	16	8	6	6
ω_n	13.8	13.49	12.97	13.49	9.85
Q (Experimental) [23]	10500	10000	24000	22000	48000
Q [23]	10600	10400	21800	19600	47300
Q (Present)	10730	10464	22029	19866	47979
% Error from Experimental data	2.190	4.640	-8.213	-9.700	-0.044

Table 4.2 Material properties of the silicon [31]

\hat{T}_a [K]	40	80	160	293	400
E [10^9 Pa]	169.3	169.2	168.5	165.9	163.1
ρ [kg/m ³]	2330	2330	2330	2330	2327
κ [W/(mK)]	3660	1360	375	156	105
α [10^6 /K]	-0.164	-0.472	0.689	2.590	3.253
C_v [$10^6 \frac{J}{m^3K}$]	0.10275	0.43804	1.06248	1.66129	1.82670
τ_{CV} [10^{-12} sec]	1470.64	128.263	14.6416	3.95649	2.46029

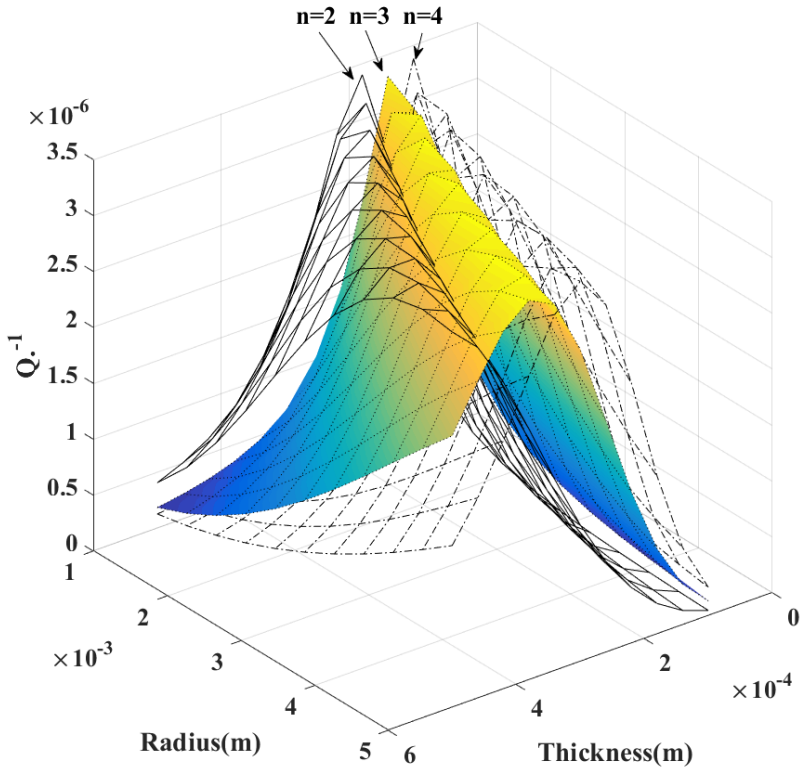
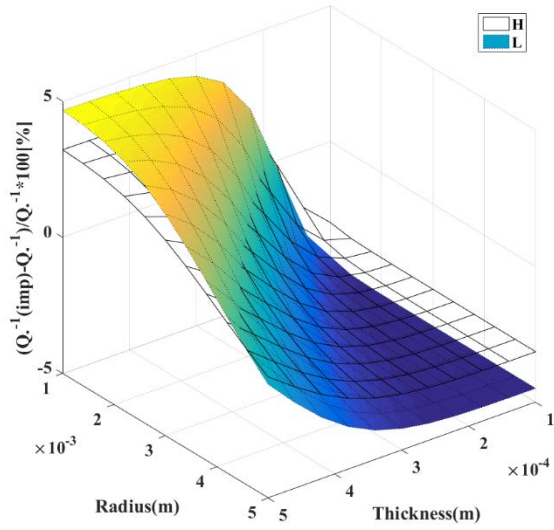
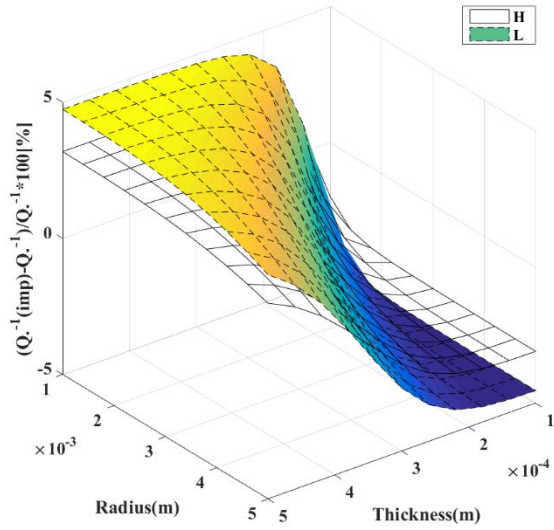


Fig. 4.1 Q^{-1} of the circular-cross-sectional ring in various modes



(a)



(b)

Fig. 4.2 Deviation of the Q with respect to the imperfection for the circular-cross-sectional ring (a) $n = 2$ (b) $n = 3$

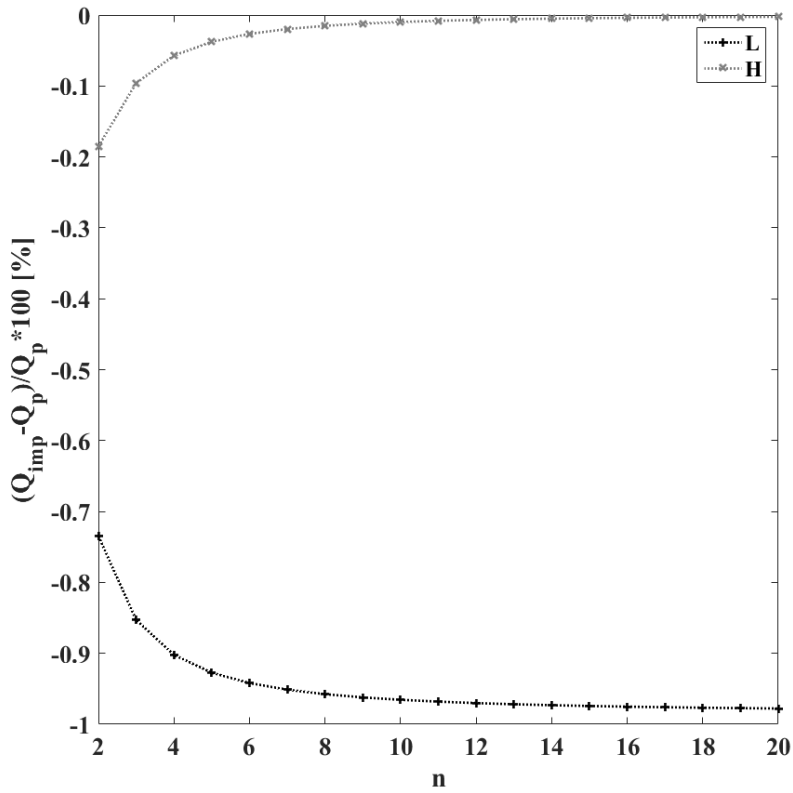
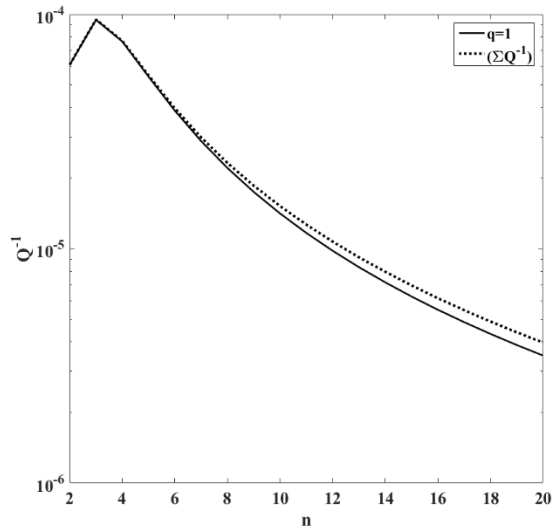
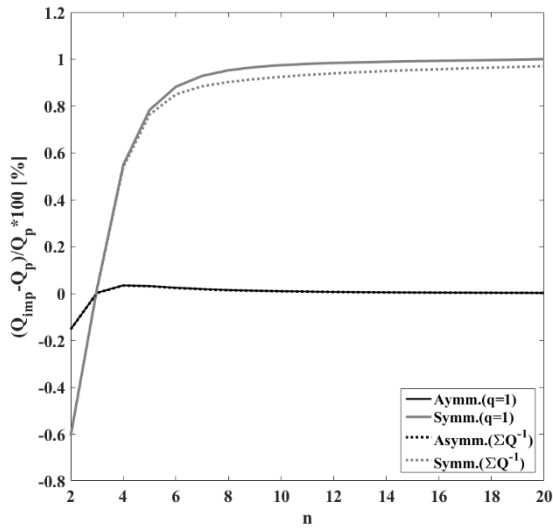


Fig. 4.3 Deviation of the Q with respect to the mode number for circular-cross-sectional ring

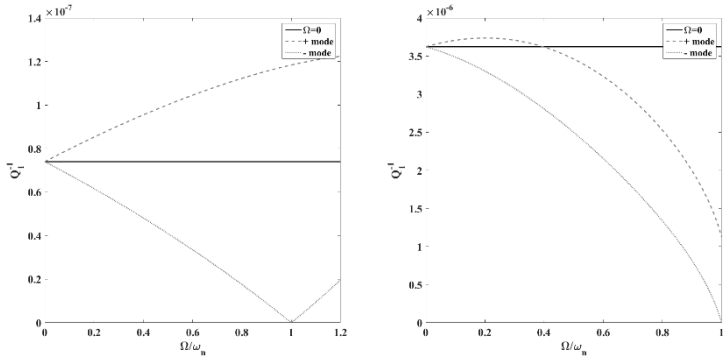


(a)



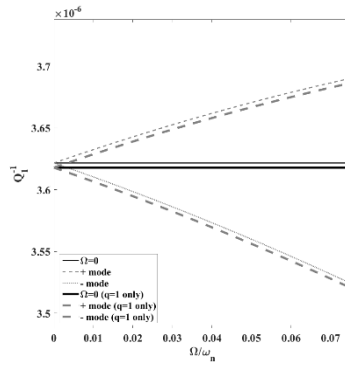
(b)

Fig. 4.4 (a) Deviation of the Q with respect to the imperfection for circular-cross-sectional ring (b) % difference from uniform ring



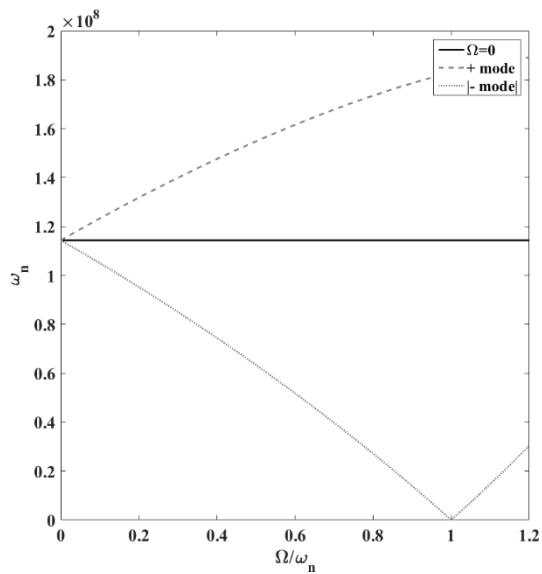
(a)

(b)

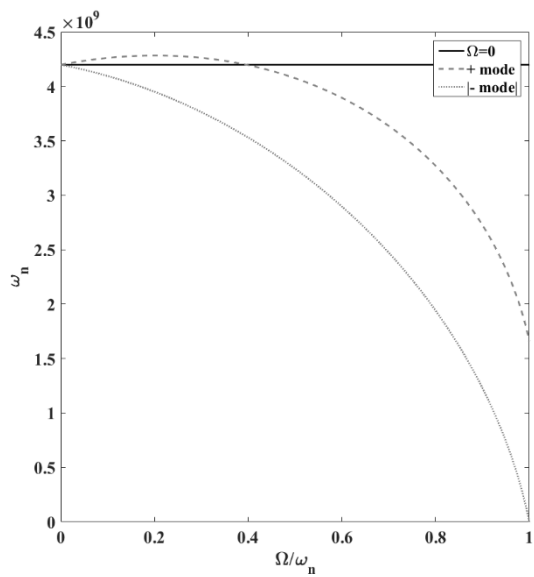


(c)

Fig. 4.5 Deviation of the Q^{-1} with respect to the rotation for circular-cross-sectional ring (a) $n = 0$, (b) $n = 10$, (c) magnified plot of (b)



(a)



(b)

Fig. 4.6 Deviation of the ω_n with respect to the rotation for circular-cross-sectional ring (a) $n = 2$, (b) $n = 10$

Chapter 5 Optimizations

5.1 Concepts

For the general thermoelastic dissipation with a small value, the energy lost per cycle with respect to the total energy per cycle can be expressed as the quality factor. The expression of the inverse value is given as [8]

$$Q^{-1} = \Delta_E \frac{\omega\tau}{1+(\omega\tau)^2} \quad (5.1.1)$$

where Δ_E and τ are the relaxation strength and time, respectively.

The value of Q^{-1} is maximum (i.e. minimum Q) with $Q^{-1} = 0.5\Delta_E$ when $\omega\tau = 1$. This phenomenon is so called as “Debye peak”, then the transient point of the two characteristics for the thermoelastic vibration. Firstly, when ω is much smaller than $\frac{1}{\tau}$, then the energy dissipation is so little and the system remains equilibrium. On the contrary, ω is much larger than $\frac{1}{\tau}$, the relaxation time is extremely short but the energy dissipation is small, too. On the other hand, a specific frequency makes the highest damping in the constant length or radius of the structure. To find the value, a differential of Q^{-1} with respect to the frequency can be used as:

$$\frac{\partial}{\partial\omega}(Q^{-1}) = 0 \quad (5.1.2)$$

The expression of the solution is designated as $(Q^{-1})_{\max} = Q_{\min}$ at $\omega =$

$\omega_{Q,\min}$. In here, the absolute value of the differential is much small on the point nearby $\omega = \omega_{Q,\max}$. Thus, to reduce the error caused by nonuniformity, the optimization concept using $\omega_{Q,\max}$ is necessary in the gyro structure.

Additionally, the isothermal eigenfrequencies of the beam and ring models, again, are:

$$(\omega_{\text{beam}})^2 = \frac{EI}{\rho A} \frac{\lambda_n^4}{L^4} \quad (5.1.3a)$$

$$(\omega_{\text{ring}})^2 = \frac{EI}{\rho A R_0^4} \frac{n^2(n^2-1)^2}{n^2+1} \quad (5.1.3b)$$

5.2 Application to a ring model with rectangular cross-section

Firstly, the concept of the optimization for a beam model is introduced in this paragraph. In here, the idea is valid only when the cross-section is rectangular because the temperature profile distributes just 1-dimensional coordinate. As the matter of fact, the temperature profile of a ring model with rectangular cross-section can be expressed as the multiple of the Young's modulus in the case as [44]. In here, Q^{-1} is maximum when $\xi_{\max} = 2.224555$ from Eq. (4.1.5b), thus $Q^{-1} = 0.494179\Delta_E$. [8] Fig. 5.1 shows the results based on Eq. (4.1.5) for both parts of the complex numbers. Using the eigenfrequency with the maximum Q^{-1} , Eq. (4.1.7) can be written as

$$(\xi_{\max})^4 = h^4 \frac{(\omega_0)^2}{4\chi^2} = \frac{h^4}{4\chi^2} \frac{n^2(n^2-1)^2}{n^2+1} \frac{EI}{\rho A a^4} \quad (5.2.1)$$

Then the modified expression with a radius of gyration as $(r_{\text{gyr}})^2 = \frac{I}{A} =$

$\frac{h^2}{12}$ is

$$R_0^4 = \frac{1}{1175.476\chi^2} \left(\frac{n^2(n^2-1)^2 E}{n^2+1} \frac{E}{\rho} \right) h^6 \quad (5.2.2)$$

As shown in here, the optimized thickness can be obtained as a deterministic diameter of the ring is constant.

Moreover, the result for optimum design on the beam model can be obtained similarly, then

$$L^4 = \frac{1}{1175.476\chi^2} \left(\lambda_n^4 \frac{E}{\rho} \right) h^6 \quad (5.2.3)$$

Figs. 5.2 (a) and (b) show the normalized Q^{-1} and the percentage difference of the Zener's and Lifshitz's models, respectively. When ξ is smaller than the Debye peak, the percentage difference is almost constant. On the contrary, the difference goes larger in the region of the larger ξ because of the truncation error of the function. In here, Zener's result [8] can be obtained by using Eq. (4.1.6), then

$$\frac{Q^{-1}}{\Delta E} = \frac{\frac{2\xi^2}{\pi^2}}{1 + \left(\frac{2\xi^2}{\pi^2} \right)^2} \quad (5.2.4)$$

5.3 Application to a toroidal ring: Simplified model of TED

Generally, Eq. (5.2.2) can be used only when the cross-section is rectangular due to the 1-D coordinate. However, the cross-section of the toroidal ring shows two-dimensional temperature profile due to the bending mode shape. Thus Eq. (5.2.1) is not valid longer, then the new approach of the Debye peak should be adopted to state the optimization. The Q-factor of a toroidal ring is

$$(Q_{2D})^{-1} = b_{11} \Delta_E \frac{\omega \tau_1}{1 + (\omega \tau_1)^2} \cong \Delta_E \frac{\omega \tau_1}{1 + (\omega \tau_1)^2} \quad (5.3.1)$$

In here, b_{11} is a solution from Bessel Function, thus $b_{11} \approx 0.987428$.

By a simple numerical algebra, the maximum value of $(Q_{2D})^{-1}$ is

$$[(Q_{2D})^{-1}]_{\max} = (Q_{2D,\min})^{-1} = \Delta_E \frac{\omega \tau_1}{1 + (\omega \tau_1)^2} = \frac{\Delta_E}{2} \quad (5.3.2)$$

And the relaxation time with respect to the radius of the cross-section is given as

$$\tau_1 = \frac{1}{\chi} \left(\frac{r_0}{a_{11}} \right)^2 = \frac{c_v}{k_0} \left(\frac{r_0}{a_{11}} \right)^2 \approx 0.294989 \frac{c_v}{k_0} r_0^2 \quad (5.3.3)$$

Substituting Eq. (5.3.3) into (5.3.2), thus

$$\frac{\omega_0 \times 0.294989 \frac{Cv}{k_0} r_0^2}{1 + \left(\omega_0 \times 0.294989 \frac{Cv}{k_0} r_0^2 \right)^2} = \frac{1}{2} \quad (5.3.4)$$

The radius of gyration for a toroidal ring is $(r_{\text{gyr}})^2 = \frac{I}{A} = 0.25r_0^2$, thus the form of eigenfrequency is re-written as

$$(\omega_0)^2 = \left[\frac{n^2(n^2-1)^2 E}{n^2+1} \frac{r_0^2}{\rho} \right] \frac{r_0^2}{4R_0^4} \quad (5.3.5)$$

Using the new form of ω_0 , Eq. (5.3.4) can be re-arranged with

$$R_0^4 = \frac{1}{45.9673\chi^2} \left[\frac{n^2(n^2-1)^2 E}{n^2+1} \frac{r_0^2}{\rho} \right] r_0^6 \quad (5.3.6)$$

In the result, the optimized radius of the cross-section can be calculated for a specific material and mean-radius. For the comparison with the equation of the Section 5.2, the coefficient number is different due to the approaching method and radius of gyration. But other geometrical and material coefficients are the same in both cases.

Similarly, new form of Eq. (5.3.4) for beam can be obtained as:

$$L^4 = \frac{1}{45.9673\chi^2} \left(\lambda_n^4 \frac{E}{\rho} \right) r_0^6 \quad (5.3.7)$$

Fig. 5.3 shows the relationships between thickness and radius for a normalized ring model with $\frac{1}{45.9673\chi^2} \frac{E}{\rho} = 1$ in Eq. (5.3.6). As the mode number goes larger, the radius goes extremely larger. Moreover, the radii should be considered to be larger than the actual thickness. The reference line is suitable to set the limitation for the design.

Table 5.1 represents the results from Eqs. (5.2.2), (5.2.3), (5.3.6), and (5.3.7). As shown in here, the coefficients are the same as the same shape of the model. Thus the results can be classified as the Table for beam or ring, and the cross-sections.

5.4 Application to a toroidal ring: with respect to the known lagging time

When the lagging time τ_{CV} is known, the non-dimensional value $\beta_{CV} = \frac{\tau_{CV}}{\tau_1}$ is useful as shown in Section 3.3. Thus, the peak of $(Q_{TED,Simple})^{-1}$ can be obtained as the function of the β_{CV} . Firstly, the peak frequency is shown in Eq. (3.3.8) as [42][43]

$$(\omega_{peak,n})^2 = \frac{1}{\tau_{CV}^2} \frac{f(\beta_{CV})}{6\beta_{CV}} \quad (5.4.1)$$

The general form of the eigenfrequency in Eqs. (5.3.5) and (5.3.7) can be equipollent with the peak frequency, thus

$$[L_{opt}(\beta_{CV})]^4 = \frac{3}{2} \left[\lambda_n^4 \frac{E}{\rho} \frac{\beta_{CV} \tau_{CV}^2}{f(\beta_{CV})} r_0^2 \right] \quad (5.4.2a)$$

$$[R_{0,opt}(\beta_{CV})]^4 = \frac{3}{2} \left[\frac{n^2(n^2-1)^2 E}{n^2+1} \frac{\beta_{CV} \tau_{CV}^2}{f(\beta_{CV})} r_0^2 \right] \quad (5.4.2b)$$

In here, $\tau_1 = \frac{r_0^2}{\chi a_{11}^2}$ and $\tau_{CV} = \frac{\chi \rho}{3E}$ are known as Eqs. (2.2.6) and (2.3.14)

for the geometrical and material properties respectively.

Fig. 5.4 shows the optimum design for radii with respect to β_{CV} for $n = 2$ (dark lines) and 20 (bright lines), respectively. And the radii as r_0 and R_0 are 1 and 10 [μm], respectively. As known in the previous Sections, the effects of the time-lagging is important in results from higher mode

number. And the optimum radius converges when the lagging time is longer. Fig. 5.5 represents the normalized Q^{-1} for the same model in Fig. 5.4 for optimized model. In here, the dissipation due to the time-lagging is significant when the lagging is longer. But in the 3-D ring in $n = 2$ mode, the line goes reversely because of the characteristic for Debye peak. Again, the geometrical properties are important because the characteristics appear in the opposite direction to the peaks.

Table 5.1 Comparisons of the results for optimization

	Rectangular	Circular
Cross-section	$\frac{1}{1175.476\chi^2} \frac{E}{\rho} \times$	$\frac{1}{45.9673\chi^2} \frac{E}{\rho} \times$
Beam $L^4 =$	$(\lambda_n^4)h^6$	$(\lambda_n^4)r_0^6$
Ring $(R_0)^4 =$	$\left(\frac{n^2(n^2 - 1)^2}{n^2 + 1}\right)h^6$	$\left(\frac{n^2(n^2 - 1)^2}{n^2 + 1}\right)r_0^6$

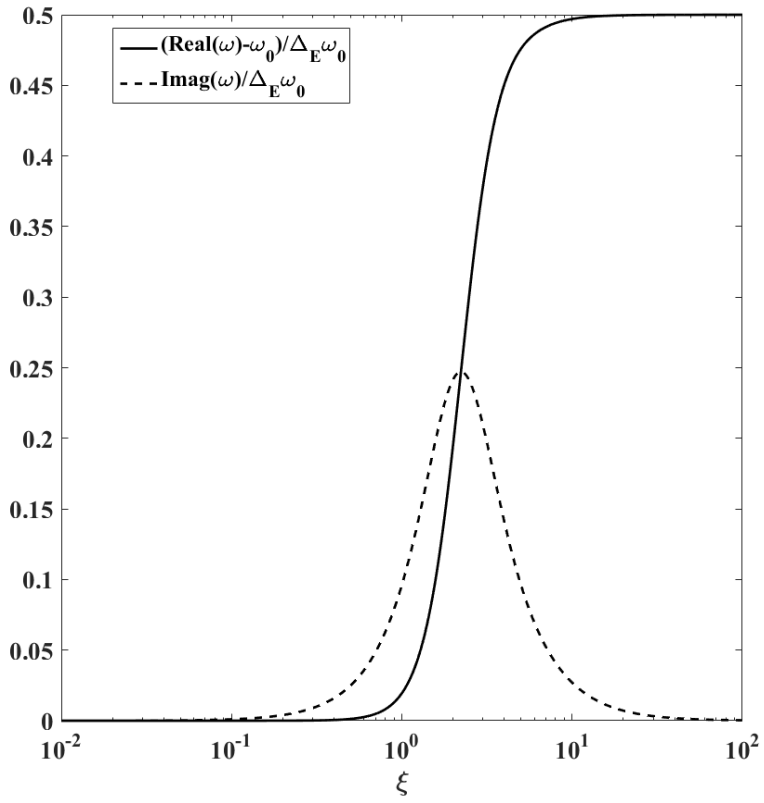
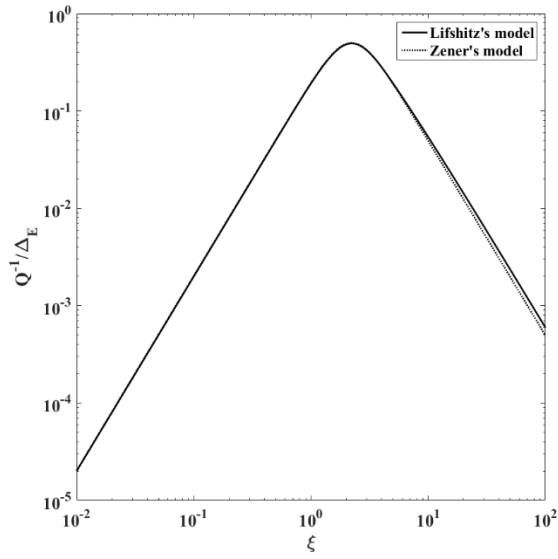
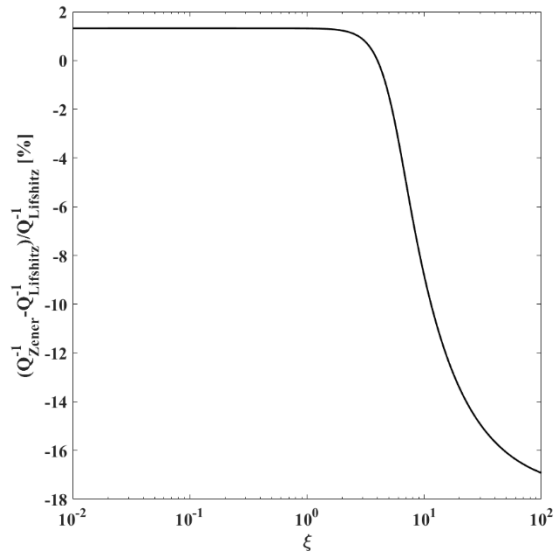


Fig. 5.1 optimization concept of the rectangular cross-sectional ring: ξ to the complex numbers



(a)



(b)

Fig. 5.2 (a) Comparison of Q^{-1} between Zener's and Lifshitz's models,
 (b) % difference between both models

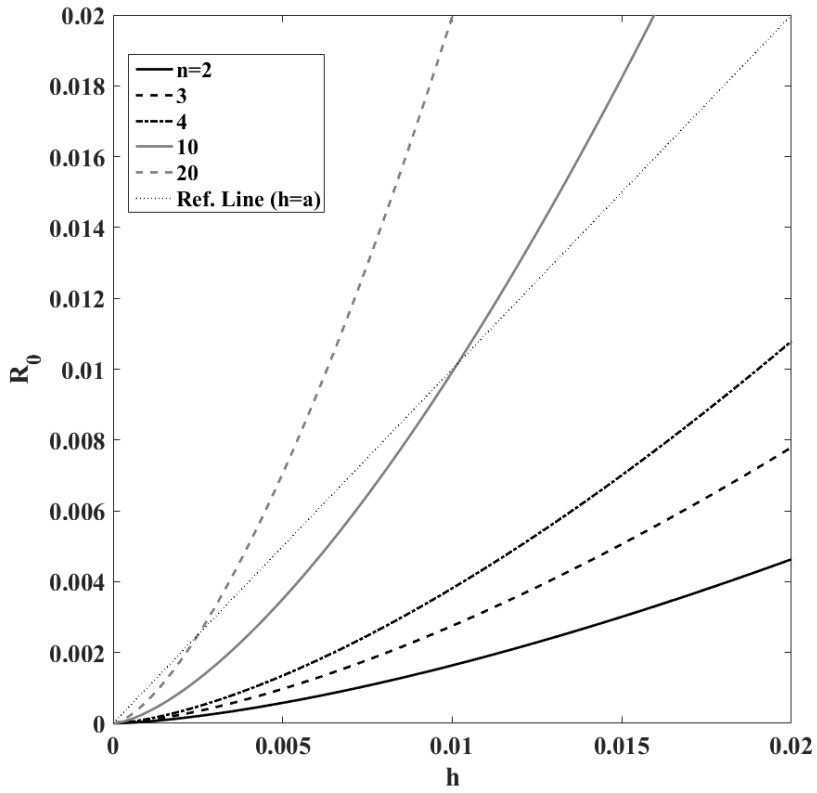


Fig. 5.3 Optimum radii with respect to the radial thickness

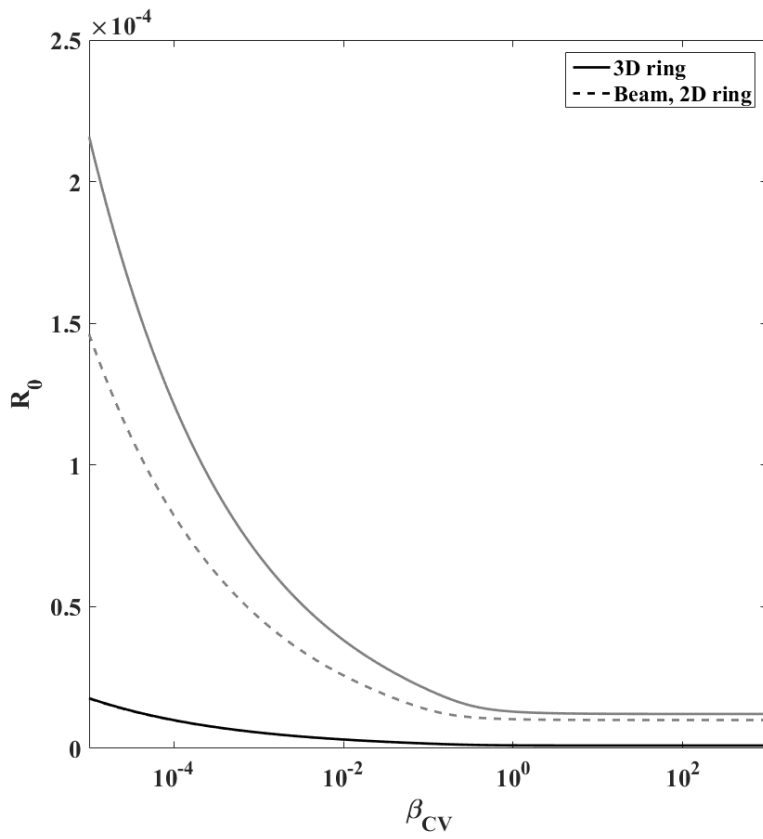


Fig. 5.4 Optimum radii with respect to β_{CV}

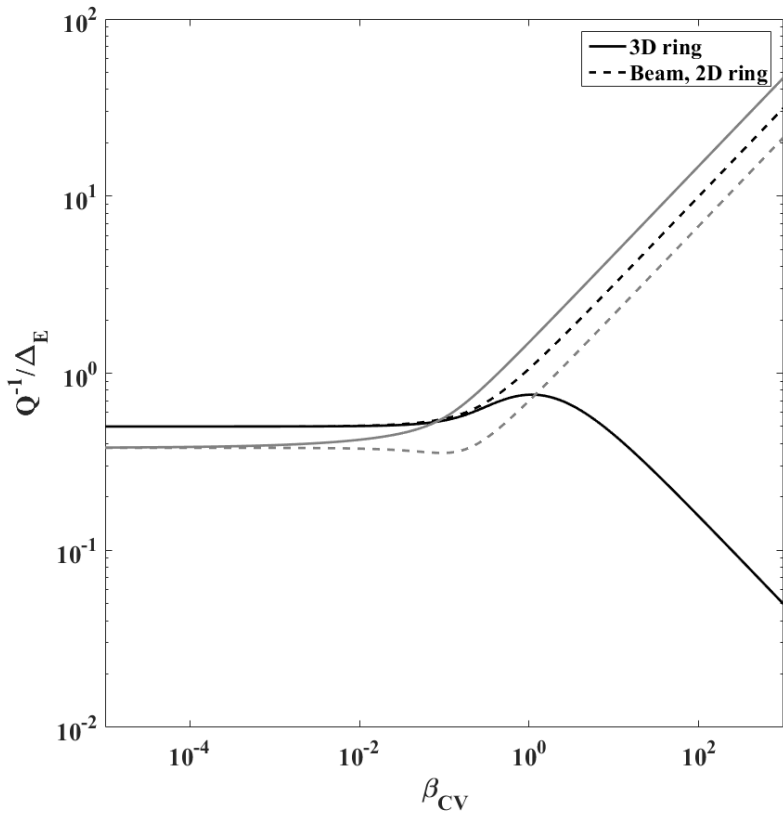


Fig. 5.5 Q^{-1} with respect to β_{CV} on optimum points

Chapter 6 Conclusions

The micro- or nano-ring structure is one of a useful model for gyroscope, sensor, or actuator, *etc.* Firstly, the internal friction effect during the motion should be considered for the micro- or nano-scaled model, *e.g.* thermoelastic dissipation. Additionally, the time delay of heat flux is mainly analyzed to compensate the limitation of the assumption of the infinity velocity of the flux for the ultrahigh frequency or extremely low temperature. To describe the temperature profile, the Bessel function of 1st kind is used with adiabatic boundary condition. And the inverse value of quality factor is defined to evaluate the energy loss to the total energy of single cycle. Moreover, the peak point of the Q is investigated with respect to the lagging time or frequency. And the equivalent damping coefficient of the cycle is represented to describe the linear dissipation model.

Furthermore, the expressions of the eigenfrequency of the ring with point masses are investigated by Rayleigh-Ritz method. In here, the inextensional assumption is applied as the constant centerline of the ring. And then, the spectral density of the structure is represented based on the forced vibration model. Furthermore, the characteristics of the random vibration is investigated by maximum deflection, velocity, and acceleration of deflection.

For the optimization concept, the maximum value of Q^{-1} (i.e. minimum value of Q) can be obtained by the characteristics of the TED. In the rectangular-cross-sectional model, the explicit function of Real and

Imaginary parts are obtained by solving the differential equation. On the contrary, the clear form of the TED for the circular-cross-sectional model cannot be defined because the temperature profile is not linear during the motion. Thus, the optimization of the structure should be stated by the Zener's model based on the relaxation time. Both models are compared and the concept is represented with respect to the geometrical properties. Generally, the point indicates minimum Q , but the deviations due to the external causes are smallest in this situation. Thus the point is important to design the actual ring resonator by the conservative point of the view.

The summarizations of the present works are given as follows:

6.1 Summary

1. Thermoelastic dissipation (TED) is one of the internal friction due to the motion on the molecular scale. And the heat flux is finite velocity, but the classical researches have been investigated as ideal flux with infinite velocity. Thus, Cattaneo and Vernotte's non-Fourier heat conduction is mainly discussed with respect to the gradient of the temperature profile. The advanced model of the conduction is available at ultralow temperature or high-frequency resonators, *e.g.* superconductor. For the circular cross-section, the Laplacian is given as cylindrical coordinate. And the geometrical and thermal strains are defined by using inextensional assumption and thermal expansion coefficient. Then the heat conduction equation is established according to the local coordinate, and the solutions of the profile is obtained by Bessel's function of 1st kind with the adiabatic boundary condition on the surface of the model. Thus, the temperature profiles are clearly obtained as 3-dimensional expression. The important characteristic of the result is the thickness effect of the toroidal ring.

The TED can be described by the ratio of loss energy to the total energy per cycle, thus the quality factor (Q-factor, Q) is introduced as inverse value. By performing the integral through the cycle using the strain and temperature profiles, the summation of Q is obtained with respect to the Bessel function. Moreover, the peak of Q^{-1} is suggested according to the frequency and lagging time in order to analysis the characteristic of the structure in terms of the optimal design. Furthermore, the equivalent linear

damping coefficient is obtained by the definition of the equation of motion. The result can be applied into the analysis of the random vibration, *etc.*

2. Rayleigh-Ritz method is consisted with kinetic and strain energies. And the rotating effect is included in the kinetic energy, then the variations can be applied into the both energies. Then an assumption as inextensional condition is considered to simplify the motion as constant centerline. The general mode shape as the homogeneous solution is introduced, and the eigenfrequency with rotating is obtained as backward and forward trips of wave motions. Furthermore, the imperfection is modeled as a virtual density and distorted angle with respect to the function of the angular position and mode number.

Moreover, the external input and linear damping forces per length are introduced as the component of the equations of motion. Solving the forced vibration, the summation of the mode shapes is obtained with respect to the mode numbers. Thus, the form of the transfer function is obtained in order to describe the response of the irregular motion. Then, the spectral density (SD) of the structure is presented as the response function. To simplify the analysis, the approximation of the SD can be used by eliminating the off-diagonal terms in the SD. But the antiresonances disappear because of the truncation error. Furthermore, the average deflections are obtained on the specific band of the output frequencies. And the Crest factor (or peak factor) is applied to estimate the maximum deflections during the motion based on the standard deviation (StDev). Finally, the Vanmarcke's bandwidth

parameter and spectral moments are introduced to obtain the StDev.

The frequency trimming is a method of the compensating the split of the eigenfrequencies due to the imperfection, based on Rayleigh-Ritz method. Eliminate the eigenfrequency of the uniform structure, then the actual frequencies can be set the same value. Thus, the angular position and the amount of point masses can be obtained as the correction factors.

3. The optimization concept of the ring considering the TED is represented in the last paragraph. For the rectangular-cross-sectional ring, the simplified forms of the Q^{-1} with Real and Imaginary parts are used with respect to the eigenfrequency and thickness. The result is the function of the thickness, thus the TED can be described as the modified Young's modulus. As the result, the relationship of the radius and thickness is clearly obtained as the peak points.

On the other hand, the result cannot be applied into circular-cross-sectional ring due to the bending shape on the cross-section, thus the first relaxation time is more suitable in the analysis, rather than the modified Young's modulus. Solving the same way based on the relaxation time with the rectangular-cross-sectional ring, the relationship is established similar to the previous case. Finally, the Debye peak is a physically important point for an optimization approach for the characteristics of the TED with time delay.

6.2 Future works

Although this thesis suggests that the characteristics of micro- or nano-ring model and optimization based on the thermoelastic dissipation, there are more challenging further works as follows:

1. The random vibration of the ring considering the thermoelastic characteristics can be investigated as the estimation of the fatigue life. The temperature properties are much important in the MEMS, thus the topic will be suitable to research in the near future. And this subject is one of the connection to the actual structure, thus the work will be interesting.

2. The time-domain analysis is more advanced topic in the part of the investigation. The method can supplement actual motion in frequency-domain analysis, and visually describe the dissipation and stability more clearly.

3. The effects caused by the imperfect mass and stiffness can be studied for the ultralow temperature. The effects due to the elements show difference results with respect to the various environments.

4. Non-Fourier heat conduction can be extended to the cylindrical shell model. The estimation of the result for a cylindrical shell can be good investigation to maintain continuity of the whole works.

5. The dual-phase-lagging effect is one of an interesting topic for the TED. The main difference from present work is that the time-lagging exists in not only heat-flux but also the thermal gradient.

6. Finally, the overlapped multiple effects of the former physical

characteristics can be suggested as the future studies.

References

- [1] Williams, H. E. (1973). On the equations of motion of thin rings. *Journal of Sound Vibration*, 26, 465-488.
- [2] Lin, S. M. (2014). Analytical solutions for thermoelastic vibrations of beam resonators with viscous damping in non-Fourier model. *International Journal of Mechanical Sciences*, 87, 26-35.
- [3] Mohanty, P., Harrington, D. A., Ekinici, K. L., Yang, Y. T., Murphy, M. J., & Roukes, M. L. (2002). Intrinsic dissipation in high-frequency micromechanical resonators. *Physical Review B*, 66(8), 085416.
- [4] Kim, S. B., & Kim, J. H. (2011). Quality factors for the nanomechanical tubes with thermoelastic damping and initial stress. *Journal of Sound and Vibration*, 330(7), 1393-1402.
- [5] Belardinelli, P., Brocchini, M., Demeio, L., & Lenci, S. (2013). Dynamical characteristics of an electrically actuated microbeam under the effects of squeeze-film and thermoelastic damping. *International Journal of Engineering Science*, 69, 16-32.
- [6] Kim, B., Hopcroft, M. A., Candler, R. N., Jha, C. M., Agarwal, M., Melamud, R., Chandorkar, S.A. , Yama, G., & Kenny, T. W. (2008). Temperature dependence of quality factor in MEMS resonators. *Journal of Microelectromechanical systems*, 17(3), 755-766.
- [7] Lei, Y., Adhikari, S., & Friswell, M. I. (2013). Vibration of nonlocal Kelvin–Voigt viscoelastic damped Timoshenko beams. *International Journal of Engineering Science*, 66, 1-13.

- [8] Zener, C. (1937). Internal friction in solids. I. Theory of internal friction in reeds. *Physical review*, 52(3), 230.
- [9] Lifshitz, R., & Roukes, M. L. (2000). Thermoelastic damping in micro-and nanomechanical systems. *Physical review B*, 61(8), 5600.
- [10] Kunal, K., & Aluru, N. R. (2011). Akhiezer damping in nanostructures. *Physical Review B*, 84(24), 245450.
- [11] Tserkovnyak, Y., Brataas, A., & Bauer, G. E. (2002). Enhanced Gilbert damping in thin ferromagnetic films. *Physical review letters*, 88(11), 117601.
- [12] Khisaeva, Z. F., & Ostoja-Starzewski, M. (2006). Thermoelastic damping in nanomechanical resonators with finite wave speeds. *Journal of Thermal stresses*, 29(3), 201-216.
- [13] Cattaneo, C. (1958). Sur une forme d'équation de la chaleur éliminant le paradoxe d'une propagation instantanée. *Comptes Rendus de l'Académie des Sciences*, 247 , 431–433 .
- [14] Vernotte, P. (1958). Les paradoxes de la théorie continue de l'équation de la chaleur. *Comptes Rendus de l'Académie des Sciences*, 246 , 3154–3155 .
- [15] Kim, B., Hopcroft, M. A., Candler, R. N., Jha, C. M., Agarwal, M., Melamud, R., Chandorkar, S. A., Yama G. & Kenny, T. W. (2008). Temperature dependence of quality factor in MEMS resonators. *Journal of Microelectromechanical systems*, 17(3), 755-766.
- [16] Houston, B. H., Photiadis, D. M., Marcus, M. H., Bucaro, J. A.,

- Liu, X., & Vignola, J. F. (2002). Thermoelastic loss in microscale oscillators. *Applied Physics Letters*, 80(7), 1300-1302.
- [17] Zhong, Z. Y., Zhang, W. M., Meng, G., & Wang, M. Y. (2015). Thermoelastic damping in the size-dependent microplate resonators based on modified couple stress theory. *Journal of Microelectromechanical Systems*, 24(2), 431-445.
- [18] A., Kumar, S., & Moallemi, M. K. (1991). Significance on non-Fourier heat waves in microscale conduction. In *Winter Annual Meeting of the American Society of Mechanical Engineers*. Publ by ASME.
- [19] Lewandowska, M., & Malinowski, L. (2001). Analytical method for determining critical energies of uncooled superconductors based on the hyperbolic model of heat conduction. *Cryogenics*, 41(4), 267-273.
- [20] Lindström, T., Healey, J. E., Colclough, M. S., Muirhead, C. M., & Tzalenchuk, A. Y. (2009). Properties of superconducting planar resonators at millikelvin temperatures. *Physical Review B*, 80(13), 132501.
- [21] Kim, J. H., & Kim, J. H. (2018). Mass imperfections in a toroidal micro-ring model with thermoelastic damping. *Applied Mathematical Modelling*, 63, 405-414.
- [22] Duwel, A., Gorman, J., Weinstein, M., Borenstein, J., & Ward, P. (2003). Experimental study of thermoelastic damping in MEMS gyros. *Sensors and Actuators A: Physical*, 103(1-2), 70-75.
- [23] Wong, S. J., Fox, C. H. J., McWilliam, S., Fell, C. P., & Eley, R. (2004). A preliminary investigation of thermo-elastic damping in silicon

- rings. *Journal of micromechanics and microengineering*, 14(9), S108.
- [24] Nayfeh, A. H., & Younis, M. I. (2004). Modeling and simulations of thermoelastic damping in microplates. *Journal of Micromechanics and Microengineering*, 14(12), 1711.
- [25] Sun, Y., Fang, D., & Soh, A. K. (2006). Thermoelastic damping in micro-beam resonators. *International Journal of Solids and Structures*, 43(10), 3213-3229.
- [26] Lu, P., Lee, H. P., Lu, C., & Chen, H. B. (2008). Thermoelastic damping in cylindrical shells with application to tubular oscillator structures. *International Journal of Mechanical Sciences*, 50(3), 501-512.
- [27] Kim, S. B., Na, Y. H., & Kim, J. H. (2010). Thermoelastic damping effect on in-extensional vibration of rotating thin ring. *Journal of Sound and vibration*, 329(9), 1227-1234.
- [28] Choi, J., Cho, M., & Rhim, J. (2010). Efficient prediction of the quality factors of micromechanical resonators. *Journal of Sound and Vibration*, 329(1), 84-95.
- [29] Sharma, J. N. (2011). Thermoelastic damping and frequency shift in micro/nanoscale anisotropic beams. *Journal of Thermal Stresses*, 34(7), 650-666.
- [30] Guo, F. L., Wang, G. Q., & Rogerson, G. A. (2012). Analysis of thermoelastic damping in micro-and nanomechanical resonators based on dual-phase-lagging generalized thermoelasticity theory. *International Journal of Engineering Science*, 60, 59-65.

- [31] Guo, F. L., Song, J., Wang, G. Q., & Zhou, Y. F. (2014). Analysis of thermoelastic dissipation in circular micro-plate resonators using the generalized thermoelasticity theory of dual-phase-lagging model. *Journal of Sound and Vibration*, 333(11), 2465-2474.
- [32] Senkal, D., Ng, E. J., Hong, V., Yang, Y., Ahn, C. H., Kenny, T. W., & Shkel, A. M. (2015, January). Parametric drive of a toroidal MEMS rate integrating gyroscope demonstrating < 20 PPM scale factor stability. In 2015 28th IEEE International Conference on Micro Electro Mechanical Systems (MEMS) (pp. 29-32). IEEE.
- [33] Kim, J. H., & Kim, J. H. (2016). Thermoelastic damping effect of the micro-ring resonator with irregular mass and stiffness. *Journal of Sound and Vibration*, 369, 168-177.
- [34] Hong, J. S., & Lee, J. M. (1994). Vibration of circular rings with local deviation. *Journal of applied mechanics*, 61(2), 317-322.
- [35] Park, H. G., Lee, J. M., Kang, Y. J., & Kim, S. H. (2008). A study on the mode pair of a slightly asymmetric circular ring with multiple deviations. *Journal of Sound and Vibration*, 310(1-2), 366-380.
- [36] Kim, J. H., & Kim, J. H. (2016). Thermoelastic dissipation of rotating imperfect micro-ring model. *International Journal of Mechanical Sciences*, 119, 303-309.
- [37] Li, P., Fang, Y., & Zhang, J. (2016). Thermoelastic damping in microrings with circular cross-section. *Journal of Sound and Vibration*, 361, 341-354.

- [38] Alghamdi, N. A., & Youssef, H. M. (2017). Dual-phase-lagging thermoelastic damping in-extensional vibration of rotating nano-ring. *Microsystem Technologies*, 23(10), 4333-4343.
- [39] Fang, Y., & Li, P. (2015). Thermoelastic damping in thin microrings with two-dimensional heat conduction. *Physica E: Low-dimensional Systems and Nanostructures*, 69, 198-206.
- [40] Kim, J. H., Kang, S. J., & Kim, J. H. (2017). Splitting of quality factors for micro-ring with arbitrary point masses. *Journal of Sound and Vibration*, 395, 317-327.
- [41] Kim, J. H., & Kim, J. H. (2018). Separation of Q-factors for tubular microstructure with point imperfections. *Applied Mathematical Modelling*, 64, 572-583.
- [42] Zhou, H., & Li, P. (2017). Thermoelastic damping in micro-and nanobeam resonators with non-Fourier heat conduction. *IEEE Sensors Journal*, 17(21), 6966-6977.
- [43] Zhou, H., Li, P., & Fang, Y. (2018). Thermoelastic damping in circular cross-section micro/nanobeam resonators with single-phase-lag time. *International Journal of Mechanical Sciences*, 142, 583-594.
- [44] Wong, S. J., Fox, C. H. J., & McWilliam, S. (2006). Thermoelastic damping of the in-plane vibration of thin silicon rings. *Journal of sound and vibration*, 293(1-2), 266-285.
- [45] Fox, C. H. J. (1990). A simple theory for the analysis and correction of frequency splitting in slightly imperfect rings. *Journal of*

Sound and Vibration, 142(2), 227-243.

[46] Eley, R., Fox, C. H. J., & McWilliam, S. (2000). Coriolis coupling effects on the vibration of rotating rings. *Journal of sound and vibration*, 238(3), 459-480.

[47] Kirkhope, J. (1977). In-plane vibration of a thick circular ring. *Journal of Sound and Vibration*, 50(2), 219-227.

[48] Endo, M., Hatamura, K., Sakata, M., & Taniguchi, O. (1984). Flexural vibration of a thin rotating ring. *Journal of Sound and Vibration*, 92(2), 261-272.

[49] Suzuki, S. I. (1984). In-plane vibrations of circular rings. *Journal of Sound and Vibration*, 97(1), 101-105.

[50] Bickford, W. B., & Reddy, E. S. (1985). On the in-plane vibrations of rotating rings. *Journal of Sound and Vibration*, 101(1), 13-22.

[51] Huang, S. C., & Soedel, W. (1987). Effects of coriolis acceleration on the free and forced in-plane vibrations of rotating rings on elastic foundation. *Journal of sound and vibration*, 115(2), 253-274.

[52] Charnley, T., Perrin, R., Mohanan, V., & Banu, H. (1989). Vibrations of thin rings of rectangular cross-section. *Journal of sound and vibration*, 134(3), 455-488.

[53] Ellison, J., Ahmadi, G., & Kehoe, M. (2001). Passive vibration control of airborne equipment using a circular steel ring. *Journal of sound and vibration*, 246(1), 1-28.

[54] Yoon, Y. J., Lee, J. M., Yoo, S. W., & Choi, H. G. (2002). A new

method for in-plane vibration analysis of circular rings with widely distributed deviation. *Journal of sound and vibration*, 254(4), 787-800.

[55] Bisegna, P., & Caruso, G. (2007). Frequency split and vibration localization in imperfect rings. *Journal of Sound and Vibration*, 306(3-5), 691-711.

[56] Hu, J., Bando, Y., Liu, Z., Sekiguchi, T., Golberg, D., & Zhan, J. (2003). Epitaxial Heterostructures: Side-to-Side Si–ZnS, Si–ZnSe Biaxial Nanowires, and Sandwichlike ZnS–Si–ZnS Triaxial Nanowires. *Journal of the American Chemical Society*, 125(37), 11306-11313.

[57] Bartolomé, J., Cremades, A., & Piqueras, J. (2013). Thermal growth, luminescence and whispering gallery resonance modes of indium oxide microrods and microcrystals. *Journal of Materials Chemistry C*, 1(41), 6790-6799.

[58] Anguiano, S., Bruchhausen, A. E., Jusserand, B., Favero, I., Lamberti, F. R., Lanco, L., ... & Fainstein, A. (2017). Micropillar resonators for optomechanics in the extremely high 19–95-GHz frequency range. *Physical review letters*, 118(26), 263901.

[59] Pauzaskie, P. J., Sirbuly, D. J., & Yang, P. (2006). Semiconductor nanowire ring resonator laser. *Physical review letters*, 96(14), 143903.

[60] Gu, Z., Liu, S., Sun, S., Wang, K., Lyu, Q., Xiao, S., & Song, Q. (2015). Photon hopping and nanowire based hybrid plasmonic waveguide and ring-resonator. *Scientific reports*, 5, 9171.

[61] Ricciardi, G. (1994). Random vibration of beam under moving

loads. *Journal of Engineering Mechanics*, 120(11), 2361-2380.

[62] Crandall, S. H., & Yildiz, A. (1962). Random vibration of beams. *Journal of Applied Mechanics*, 29(2), 267-275.

[63] Jacquot, R. G. (2000). Random vibration of damped modified beam systems. *Journal of sound and vibration*, 234(3), 441-454.

[64] Jiao, G., & Moan, T. Probabilistic analysis of fatigue due to Gaussian load processes. *Probabilistic Engineering Mechanics*, 5(2) (1990) 76-83.

[65] Zhao, W., & Baker, M. J. On the probability density function of rainflow stress range for stationary Gaussian processes. *International Journal of Fatigue*, 14(2) (1992) 121-135.

[66] Elishakoff, I., & Livshits, D. (1984). Some closed-form solutions in random vibration of Bernoulli-Euler beams. *International journal of engineering science*, 22(11-12), 1291-1301.

[67] Elishakoff, I., & Livshits, D. (1989). Some closed-form solutions in random vibration of Bresse-Timoshenko beams. *Probabilistic Engineering Mechanics*, 4(1), 49-54.

[68] Gopalakrishnan, S., Martin, M., & Doyle, J. F. (1992). A matrix methodology for spectral analysis of wave propagation in multiple connected Timoshenko beams. *Journal of Sound and Vibration*, 158(1), 11-24.

[69] Chang, T. P. (1994). Deterministic and random vibration of an axially loaded Timoshenko beam resting on an elastic foundation. *Journal*

of sound and vibration, 178(1), 55-66.

[70] Birgersson, F., Ferguson, N. S., & Finnveden, S. (2003). Application of the spectral finite element method to turbulent boundary layer induced vibration of plates. *Journal of Sound and Vibration*, 259(4), 873-891.

[71] Barbato, M., & Conte, J. P. (2008). Spectral characteristics of non-stationary random processes: Theory and applications to linear structural models. *Probabilistic Engineering Mechanics*, 23(4), 416-426.

[72] Wang, B. T. (2009). Vibration analysis of a continuous system subject to generic forms of actuation forces and sensing devices. *Journal of Sound and Vibration*, 319(3-5), 1222-1251.

[73] Zhang, Y. H., Li, Q. S., Lin, J. H., & Williams, F. W. (2009). Random vibration analysis of long-span structures subjected to spatially varying ground motions. *Soil Dynamics and Earthquake Engineering*, 29(4), 620-629.

[74] Araújo, I. G., & Laier, J. E. (2014). Operational modal analysis using SVD of power spectral density transmissibility matrices. *Mechanical Systems and Signal Processing*, 46(1), 129-145.

[75] Heredia-Zavoni, E., Santa-Cruz, S., & Silva-González, F. L. (2015). Modal response analysis of multi-support structures using a random vibration approach. *Earthquake Engineering & Structural Dynamics*, 44(13), 2241-2260.

[76] Braccesi, C., Cianetti, F., & Tomassini, L. (2015). Random fatigue.

A new frequency domain criterion for the damage evaluation of mechanical components. *International Journal of Fatigue*, 70, 417-427.

[77] Awrejcewicz, J., Krysko, A. V., Papkova, I. V., Zakharov, V. M., Erofeev, N. P., Krylova, E. Y., Mrozowski J. & Krysko, V. A. (2016). Chaotic dynamics of flexible beams driven by external white noise. *Mechanical Systems and Signal Processing*, 79, 225-253.

[78] Li, Y., Zhang, Y., & Kennedy, D. (2017). Random vibration analysis of axially compressed cylindrical shells under turbulent boundary layer in a symplectic system. *Journal of Sound and Vibration*, 406, 161-180.

[79] Dahlberg, T. (1982). Modal cross-spectral terms may be important and an alternative method of analysis be preferable. *Journal of Sound and Vibration*, 84(4), 503-508.

[80] Dahlberg, T. (1999). The effect of modal coupling in random vibration analysis. *Journal of Sound and vibration*, 228(1), 157-176.

[81] Chen, S. Y., Niu, X., & Guo, F. L. (2018). Thermoelastic damping in micromechanical resonators operating as mass sensors. *European Journal of Mechanics-A/Solids*, 71, 165-178.

[82] Rourke, A. K., McWilliam, S., & Fox, C. H. J. (2001). Multi-mode trimming of imperfect rings. *Journal of Sound and Vibration*, 248(4), 695-724.

[83] Rourke, A. K., McWilliam, S., & Fox, C. H. J. (2002). Multi-mode trimming of imperfect thin rings using masses at pre-selected locations. *Journal of sound and vibration*, 256(2), 319-345.

- [84] Wang, K., Wong, A. C., Hsu, W. T., & Nguyen, C. C. (1997, June). Frequency trimming and Q-factor enhancement of micromechanical resonators via localized filament annealing. In Proceedings of International Solid State Sensors and Actuators Conference (Transducers' 97) (Vol. 1, pp. 109-112). IEEE.
- [85] Rourke, A. K., McWilliam, S., & Fox, C. H. J. (2005). Frequency trimming of a vibrating ring-based multi-axis rate sensor. *Journal of sound and vibration*, 280(3-5), 495-530.
- [86] Kim, J. H., & Kim, J. H. (2017). Trimming of imperfect hemispherical shell including point mass distributions. *International Journal of Mechanical Sciences*, 131, 847-852.
- [87] Behbahani, A. H., & M'Closkey, R. T. (2017). Frequency analysis of a uniform ring perturbed by point masses and springs. *Journal of Sound and Vibration*, 397, 204-221.
- [88] Llobet, J., Gerbolés, M., Sansa, M., Bausells, J., Borrísé, X., & Perez-Murano, F. (2015). Fabrication of functional electromechanical nanowire resonators by focused ion beam implantation. *Journal of Micro/Nanolithography, MEMS, and MOEMS*, 14(3), 031207.
- [89] Guo, X., Yi, Y. B., & Pourkamali, S. (2013). A finite element analysis of thermoelastic damping in vented MEMS beam resonators. *International Journal of Mechanical Sciences*, 74, 73-82.
- [90] Soedel, W. (2004). *Vibrations of shells and plates*. CRC Press.
- [91] Inman, D. J. (2007) *Engineering vibration*. Englewood Cliffs, NJ:

Prentice Hall.

국문초록

시간지연 열-탄성 감쇠를 고려한 자이로 구조물의 최적화 설계에 대한 연구

김정환

서울대학교 대학원

기계항공공학부

본 학위논문에서는 비(非) 푸리에 열전도를 고려한 열-탄성 감쇠 자이로 구조물의 진동 특성을 주로 연구하였다. 먼저, 유한 열유속 속도로 인한 시간지연 현상이 포함된 열-탄성 감쇠를 보여주었다. 그 해로써 1종 베셀함수에 의한 3차원 열전도 방정식을 풀어서 온도 형상을 구하였다. 그리하여 열-탄성 감쇠는 복소수로 구성된 양질계수로 정의될 수 있음을 확인하였다. 또한 진동수의 함수로서 양질계수의 역수를 구하였고, 진동수, 시간지연, 기하학적 형상에 의해 정해지는 간략화된 결과식 역시 도출하였다. 여기서 시간지연은 2차음속으로 정의될 수 있다. 또한 열-탄성 감쇠는 1회 진동에서 선형 감쇠계수로 근사화될 수 있음을 확인하였다. 온도 형상은 열 유속의 시간지연을 기하학적으로 묘사하였다.

다음으로, 불균일 질량과 회전 효과를 고려한 진동의 지배방정식을 도출하기 위해 해밀톤 원리에 의한 레일라이-리츠

방법을 적용하였다. 그 다음 늘어나지 않는 고리의 고유진동수를 불균일 질량에 대한 가상밀도로 구하였다. 또한 불규칙 진동 현상을 묘사하기 위하여 라플라스 변환에 의한 전달함수를 유도하였다. 전달함수에 대한 스펙트럼밀도를 구하였고 표준편차를 사용한 불규칙 진동의 응용을 제안하였다. 그리고 최대변위를 예측하여 피로예측 인자 등에 사용 가능한 파괴율을 소개하였다. 그리고 부착질량으로 인한 진동수 갈라짐을 보정하는 진동수 트리밍 방법을 연구하였다.

본 논문에서는 양질계수의 역수를 해석하는 최적화 방법을 제안함으로써 수치적 데이터를 보여주고 있다. 극점을 찾기 위해 진동수와 단면 두께에 연관된 인자를 사용하였다. 그리고 반지름과 기타 물성치를 두께의 함수로 표현하였다. 극점에서는 감쇠가 최대이지만 불균일 질량에 의한 변화는 가장 작다. 또한 이러한 시점에서, 극점은 보수적 설계에 적합할 수 있음을 확인하였다.

주요어: 자이로 구조물; 열-탄성 감쇠, 비(非) 푸리에 열전도;

평면 진동; 양질 계수; 스펙트럼 밀도; 주파수 트리밍

학번: 2014-31044